Power Extraction from an Oscillating Water Column along a coast

by

Hervé Martins-rivas

Submitted to the Department of Aeronautics and Astronautics
in partial fulfillment of the requirements for the degree of

Master of Science in Aeronautics and Astronautics

at the

MASSACHUSETTS INSTITUTE OF TECHNOLOGY

June 2008

Author .....
Department of Aeronautics and Astronautics
May 23, 2008

Certified by .....
Prof. Chiang C. Mei
Ford Professor of Engineering,
Department of Civil and Environmental Engineering
Thesis Supervisor

Accepted by .....
Prof. David L. Darmofal
Associate Department Head Chair, Committee on Graduate Students

Power Extraction from an Oscillating Water Column along a coast

by

Hervé Martins-rivas

Submitted to the Department of Aeronautics and Astronautics
on May 23, 2008, in partial fulfillment of the
requirements for the degree of
Master of Science in Aeronautics and Astronautics

Abstract

For reasons of wave climate, geography, construction, maintenance, energy storage and transmission, some devices for extracting energy from sea waves will likely be installed on the coast. We study here the specific case where an Oscillating Water Column (OWC) is attached to the tip of a long breakwater.
A three-dimensional numerical model of a skeletal geometry of the the Foz do Douro breakwater is developed in order to determine the response inside the OWC pneumatic chamber to incident waves and assess the possible effects of the breakwater geometry. The model uses the hybrid element method and linear water wave theory.
Then, a more analytical approach for a simplified geometry is presented. Making use of an exact solution for the scattering by a solid cylinder connected to a wedge, we solve for the linearized problems of radiation and scattering for a hollow cylinder with an open bottom. Power-takeoff by Wells turbines above an air chamber is modeled by including the compressibility of air. It is shown for the case of a circular OWC attached to a thin breakwater, that the incidence angle affects only the waves in and outside the column but not the power extraction which depends only on the averaged water-surface displacement inside. Optimization by controlling the turbine characteristics is examined for a wide range of wavelengths.
Finally, the same approach is used to solve the case of an OWC positioned along a straight coast line. It is found that in this configuration, the extracted power does depend on the incidence angle. It is also shown that the average efficiency is doubled compared to the thin breakwater geometry.

Thesis Supervisor: Prof. Chiang C. Mei
Title: Ford Professor of Engineering,
Department of Civil and Environmental Engineering

Acknowledgments

This work is sponsored by the MIT-Portugal Alliance Grant as a part of the Sustainable Energy Systems group.

The research effort leading to this report has been carried out under the supervision of Prof. Chiang C. Mei. I would like to take this opportunity to thank Prof. Mei for his guidance and extraordinary availability.

I am also grateful to Prof. A. Sarmento and Prof. A. Falcão from Instituto Superior Técnico, Lisbon, Portugal, for their extremely valuable inputs and comments given at the occasion of several discussions during their visits at MIT.

Contents

List of Figures

List of Tables

Chapter 1

Introduction

The science and technology of power extraction from sea waves have been steadily advancing since the 1970's. Reviews of the earlier devices can be found in McCormick [1], Evans [2] and Mei [3]. More recent surveys have been given by Falcão [4] and Falnes [5]. While many design concepts now exist at diverse stages of development, the most widely studied ones approximately fall in two major categories. For one type, energy is collected from the oscillations of floating bodies such as buoys, cams or floats. In the other the oscillating water surface inside a stationary column open at the bottom pushes the dry air above through turbines.

The first studies were mostly focused on rigid-body oscillating systems like the famous Salter 'duck'. Notably, Evans [6], Mei [7] and Budal and Falnes [8] provided extremely valuable contributions in modeling this problem. The rigid-body theory has then been adapted to model simple oscillating water columns (OWC) by Evans [9]. Falcão and Sarmento considered the increased pressure on a non-plane free surface [10]. Finally, Evans provided a general theory for any number of fixed OWC [11] including a parallel with the rigid-body motion where the hydrodynamics characteristics of a system are described in terms of its added mass and radiation damping rate matrices. In the case of an OWC, the volume flux across the considered free surface replaces the concept of exciting forces exerted on a floating body. In both theories, optimum power absorption is based on the matching of impedances, i.e., the system must resonate at the design frequency and the energy absorption rate must match

the rate of radiation damping.

Both the resonance frequency and the radiation damping rate depend on the geometry of the device. Because sea waves are random and broad-banded, a design challenge is to improve the system performance so that high efficiency is achieved over a wide range of frequencies around the spectral peak of the incident sea. To achieve this goal, it is necessary in the design phase to model the power extracting device and predict its hydrodynamics characteristics. It must also be noted that it is possible to manipulate the absorber in real time by phase control (Budal and Falnes [8]) to increase the efficiency. Other ideas include the coupling of two or more mechanisms in one unit so that multiple resonant peaks can be attained.

Detailed studies of specific OWC geometries have been conducted. Theories for simple two-dimensional geometries have been derived by Smith [12] and later Evans and Porter [13]. Sarmento and Falcão presented a full model including turbin power take-off [14]. Three-dimensional axi-symmetric floating OWC geometries have been considered by Fernandes [15]. An efficient calculation method using a Galerkin formulation has been designed by Evans and Porter [16] in the case of a circular cylinder with thin walls, following the work of Garrett on bottomless harbours scattering [17]. When considering a specific system, the geometry, local bathymetry, coastline boundary and other construction details must be examined. It is now possible to use a wide variety of numerical tools such as finite element. However, it is also useful for physical insight to study idealized systems using analytical means. The understanding gained from such a study is thought to be potentially valuable to guide design efforts in their early phase.

In general the choice of sites depends not only on wave climate but also on the accessibility, construction and maintenance costs, storage, transmission, grid connection ... etc. For some projects it may be more preferable to install the entire system on the coast rather than offshore. Since 1990 the experimental OWC pilot plant on the coast of Pico, Island of Azores, Portugal, has been in operation [18]. Moreover, plans has been reported for another full size OWC station at the head of a breakwater

at the mouth of Foz do Douro River, Portugal [19]. More theoretical studies have also been conducted such as McIver and Evans approximate theory for OWC's situated in harbours along a reflecting wall [20].

This thesis presents different approaches for modelling the hydrodynamics of an OWC installed on a coast line. The first part is an hybrid element numerical model of a geometry close to an early design of the actual Foz do Douro OWC plant. The aim is to solve the scattering problem and assess the effect of the breakwater on the wave pattern, mainly the free surface inside the OWC. We consider next a simplified OWC geometry consisting of a hollow circular cylinder connected to a thin breakwater. The cylinder is open to the sea at the bottom and rises to a certain height above the mean sea level. The power-take-off system such as Wells turbines is installed on top of the cylinder. A linearized theory is developed to predict the effects of the breakwater on waves in and outside the column ; and also on power absorption. The same approach can be applied to any wedge-like coast line. As another example, we treat the case of an OWC positioned along a straight coast line. In all cases, the sea depth is assumed to be constant and the walls of the coast and structure are vertical. Monochromatic plane waves of very small slope arrive from a prescribed direction.

Chapter 2

Hybrid Model of Ceodouro Breakwater OWC

Plans have been made to install the Ceodouro power plant at the head of a long breakwater at the mouth of Foz do Douro estuary [19]. The site was chosen based on the perceived advantage of low construction cost in comparison to offshore locations. The breakwater is inclined with its head pointing in the South-West direction while the predominant waves arrive from the North-West. From wave records in the vicinity the dominant wave period is around 10 seconds and the average significant wave height 1.6 m. While issues of power takeoff and OWC performance have been analyzed in detail before [21, 22], diffraction patterns due to the long breakwater and their possible effects on the performance of an OWC unit have not been seen in open literature. We are therefore constructing a numerical model with the view to analyzing the effects of diffraction on the water level inside the chamber.

For a different project of the Azores Pilot Plant on the Island of Pico, numerical modelling of the complex geometry for an OWC plant including part of the coastline and local bathymetry has been reported by Brito-Melo et al [23]. The numerical method of boundary elements based on Green's function in a sea of constant depth was employed. The sea depth in the immediate neighborhood and in the far field were treated as being constant, so that discrete elements were only used over the vertical

walls of the cassons and the power plant and over the uneven bottom nearby.

We report here a computation of linear diffraction by the breakwater with a partially open chamber at its head. The hybrid element method developed for isolated scatterers [24, 25] is modified to account for the long breakwater. Since the incident wave comes from one side of the breakwater, we ignore for convenience the small thickness of most of the breakwater on the shadow side away from the OWC unit and the breakwater head. For confirmation of the numerical scheme several simple geometries with well-known analytical solutions are used, including a vertical circular cylinder and a semi-infinite breakwater of zero thickness. The complex geometry to be modelled is based on an early design of the Ceodouro power plant [19, 21, 22].

2.1 The Hybrid Element Method

We shall consider monochromatic waves only; the result gives the frequency response which can be used for spectral analysis of random waves. We also assume that away from the head of the breakwater, the sea depth is constant and all walls are vertical. The model is based on the linearized potential theory of an inviscid and incompressible fluid and for wave amplitude small relative to the typical water depth and structural dimensions ($a_0/a \ll 1$ and $ka = O(1)$) [3].

In the hybrid element method, the fluid domain is divided into two regions: the near field where the geometry, including the sea bottom, can be complex, and the far field where the geometry is simple and the sea depth h is constant. The two fields are separated by an imaginary circular cylinder S as shown in Figure 2-1. In the near field V, the spatial factor of the velocity potential ϕ is approximated by finite elements with unknown nodal coefficients. In the far field V' outside S, the potential ϕ' is represented by eigenfunction expansions.

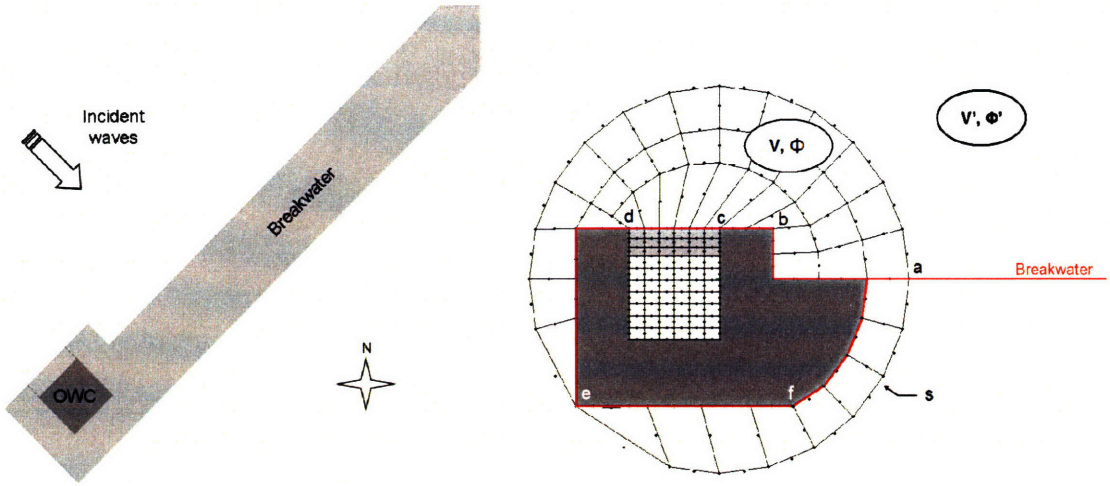

Figure 2-1: Model of Foz do Douro breakwater for the hybrid-element scheme. Left: sketch of the global configuration. Right: OWC model - marked stations (a to f) along the wall will be used for displaying local surface responses.

2.1.1 Three-dimensional Analysis

Omitting the time factor $e^{-i\omega t}$, the potential must satisfy the field equation

$$\nabla^2\phi = \left(\frac{\partial^2}{\partial x^2} + \frac{\partial^2}{\partial y^2} + \frac{\partial^2}{\partial z^2}\right)\phi = 0 \tag{2.1.1}$$

everywhere in the fluid. It is also subjected to the boundary condition

$$\frac{\partial\phi}{\partial z} - \frac{\omega^2}{g}\phi = 0 \tag{2.1.2}$$

on the free surface ($z = 0$), and the no-flux condition

$$\frac{\partial\phi}{\partial n} = 0 \tag{2.1.3}$$

on all solid walls including the sea bed at $z = -h(x, y)$.

Consider first the far field V'. Because the breakwater thickness is taken to be zero far from the OWC, advantage can be taken of the exact Sommerfeld solution ϕ_I for the diffraction by a thin semi-infinite breakwater [26]. Specifically, let the

incoming wave have the amplitude a_0, frequency ω and be inclined at an angle α with the breakwater. If the positive x axis is superimposed with the breakwater (with the origin at the tip):

$$\phi_I = -i\frac{ga_o}{\omega}\frac{\cosh k_0(z+h)}{\cosh k_0 h}\left\{J_0(k_0 r) + 2\sum_{n=1}^{\infty} e^{-in\pi/4} J_{\frac{n}{2}}(k_0 r)\cos\frac{n\theta}{2}\cos\frac{n\alpha}{2}\right\} \tag{2.1.4}$$

where k_0 is the positive real root of the dispersion relation:

$$\omega^2 = gk_0 \tanh k_0 h \tag{2.1.5}$$

Due to the presence of the complex installations at the head, additional scattering and radiation produce a correction potential which can be represented in V' by series of eigenfunctions satisfying (2.1.1):

$$\phi' - \phi_I = -i\frac{ga_o}{\omega}\sum_n\sum_m \alpha_{mn} H_{\frac{n}{2}}(k_m r) \cdot \cos\frac{n\theta}{2}\frac{\cosh k_m(z+h)}{\cosh k_m h} \tag{2.1.6}$$

where k_m, $m = 1, 2, 3, \ldots$ are the positive imaginary roots of the dispersion relation. Corresponding to each nonzero m, the eigenfunction represents an evanescent mode that does not radiate energy to infinity.

Through the propagating mode corresponding to k_0, the scattered wave satisfies the radiation condition at infinity,

$$\lim_{k_0 r\to\infty} \sqrt{r}\left(\frac{\partial}{\partial r} - \imath k_0\right)(\phi' - \phi_I) = 0 \tag{2.1.7}$$

Note also that the no flux boundary condition is satisfied on both sides of the breakwater along the x axis,

$$\frac{\partial}{\partial\theta}(\phi' - \phi_I) = 0, \quad \theta = 0, 2\pi. \tag{2.1.8}$$

Thus by construction, ϕ' satisfies (2.1.1) to (2.1.3) in the domain V' and is of course discontinuous on opposite sides of the breakwater ($\theta = 0, 2\pi$).

Along the cylindrical surface S, the two potentials (ϕ' in V' and ϕ in V) and their normal derivatives must be continuous, i.e.,

$$\phi = \phi' \quad \text{and} \quad \frac{\partial \phi}{\partial n} = \frac{\partial \phi'}{\partial n} \tag{2.1.9}$$

It can be shown (appendix A) that this boundary value problem is equivalent to the stationarity of the following functional [24, 25],

$$\begin{aligned} J(\phi, \phi') = & \iiint_V \frac{1}{2} (\nabla \phi)^2 \, dV - \iint_F \frac{\omega^2}{2g} \phi^2 dF \\ & + \iint_S \left[\left(\frac{\phi' - \phi_I}{2} - (\phi - \phi_I) \right) \frac{\partial \phi'}{\partial n} - \frac{\phi' - \phi_I}{2} \frac{\partial \phi_I}{\partial n} \right] dS \end{aligned} \tag{2.1.10}$$

where F is the free surface of V ($z = 0$).

By extremizing the functional ($\delta J(\phi, \phi') = 0$), a matrix equation for the nodal coefficients in ϕ and the expansion coefficients $\{\alpha_{mn}\}$ in ϕ' is obtained and is solved numerically.

2.1.2 Two-dimensional Analysis

It is well known that if the sea depth is constant everywhere and all walls are vertical the mathematical problem becomes two-dimensional after factoring out the vertical dependence $\cosh k(z + h)$,

$$\begin{Bmatrix} \phi(x, y, z) \\ \phi'(x, y, z) \end{Bmatrix} = \begin{Bmatrix} \psi(x, y) \\ \psi'(x, y) \end{Bmatrix} \frac{\cosh k(z + h)}{\cosh kh} \tag{2.1.11}$$

For testing the algorithm, we have developed first a two-dimensional version of the hybrid-element routine, which can be checked by comparison with known analytical solutions. This simplified version is then used for validating the full three-dimensional routine for more complex two-dimensional geometries which can be solved by both routines.

We shall consider first the simple problem of a vertical cylinder in the open sea of constant depth, triangular finite elements are used to approximate ψ in a ring V between the rigid cylinder and the surface S. The scattered wave potential in the far field V' is written as

$$\psi' - \psi_I = -\frac{iga_0}{\omega} \sum_{n=0} H_n(k_0 r) \left[\alpha_n \cos n\theta + \beta_n \sin n\theta\right] \tag{2.1.12}$$

The potential of ψ_I in the far field is simply the incident wave with inclination α and amplitude a_0

$$\psi_I = -\frac{iga_0}{\omega} e^{ik_0 r \cos(\theta - \alpha)}$$

For the long breakwater we take for the far field the Sommerfeld solution as ψ_I and the scattered wave to be

$$\psi' - \psi_I = -\frac{iga_0}{\omega} \sum_{n=0} \alpha_n H_{\frac{n}{2}}(k_0 r) \cos\frac{n\theta}{2} \tag{2.1.13}$$

2.2 Validations of the Numerical Model

To ensure correctness and accuracy we use two well-known exact solutions as benchmarks: (i) a semi-infinite breakwater of zero thickness and (ii) a vertical circular cylinder in an open sea.

2.2.1 Two-dimensional Model

Computed results from the two-dimensional numerical model is compared with Sommerfeld's exact solution for the thin breakwater in figure 2-3. A grid of 400 nodal points with 594 triangular elements distributed between two circles ($k_0 r = 1$ and $k_0 r = 1.3$) is used as shown in figure (2-2). We used 15 coefficients in the far field eigenfunction expansion.

As expected, the numerical values of the coefficients α_n are all nearly zero. The edge of a thin breakwater is a point of singularity near which discrete approximation is locally ineffective. The potential in a small neighbourhood of the sharp tip can be better represented analytically by another eigenfunction expansion as described in [24]. Details of this implementation are not detailed here.

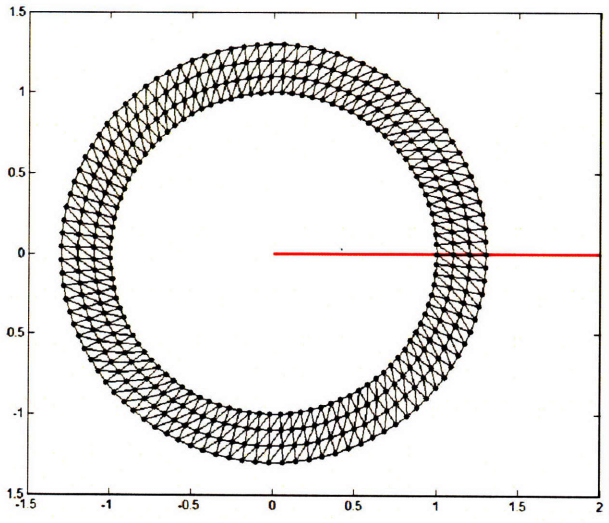

Figure 2-2: 2D Mesh for a thin breakwater. Center and outside areas are described by analytical series, the middle annulus is described with finite elements.

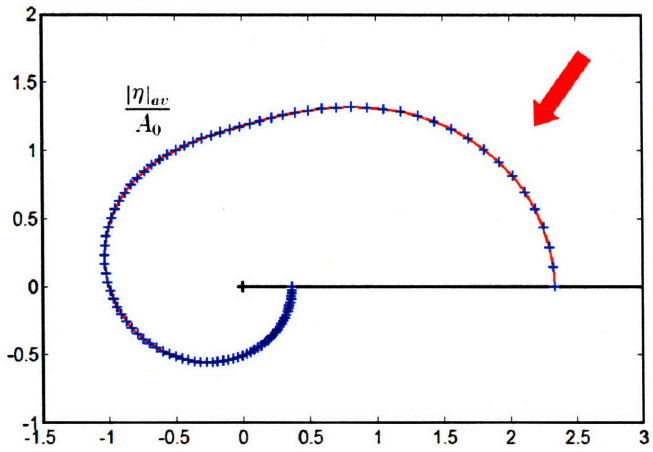

Figure 2-3: Polar plot of the maximum free-surface displacement along a circle or radius $k_0 r = 1.3$ around the head of a thin breakwater. Incidence angle with respect to the breakwater is $\alpha = 0, 3\pi$. Solid curve: 2D exact theory by Sommerfeld. Crosses: 2D numerical model.

2.2.2 Three-dimensional Model

The scattered waves must now consist of both propagating and evanescent modes. For an isolated scatterer in the open sea the outer region potential has to be

$$\begin{aligned} \phi' - \phi_I &= -\frac{iga_0}{\omega} \sum_{m=0} \sum_{n=0} H_n(k_m r)[\alpha_{m,n} \cos n\theta \\ &+ \beta_{m,n} \sin n\theta] \frac{\cosh k_m(z+h)}{\cosh k_m h} \end{aligned} \tag{2.2.14}$$

The number of expansion coefficients in the far-field potential is much greater than for the 2-D case. In the near field V, cubic elements with twenty nodal points in each element are used instead of triangles - figure (2-4) - resulting in a significant increase in the number of nodal unknowns. Hence the size of the matrices in the computation is now much greater. In addition, the integration routines which involve interpolation functions and quadrature become much more complex. However, despite the added complexity, the model is implemented on a PC. The three-dimensional model is compared to the two-dimensional analytical solution of a vertical circular cylinder as shown in figure 2-5. In particular the expansion coefficients for the sine terms in (2.2.14) which are theoretically equal to zero are of the order of 10^{-11} and the first evanescent mode coefficients are less than 10^{-2}.

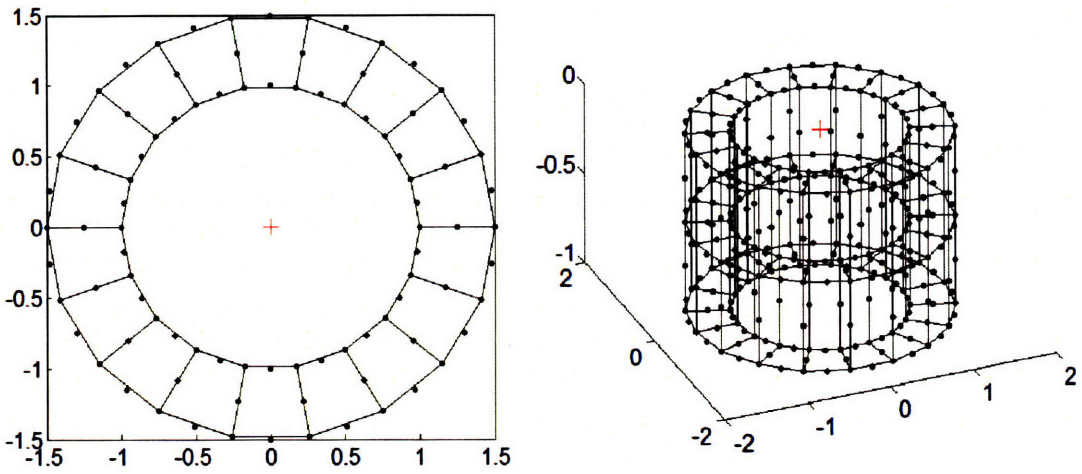

Figure 2-4: 3D mesh for a cylinder in open sea. Left: top view. Right: side view.

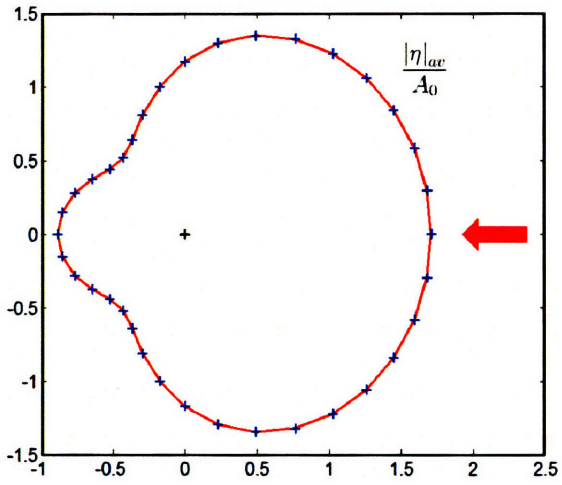

Figure 2-5: Polar plot of the maximum free-surface displacement along the wall of a vertical circular cylinder in an open sea. Incidence angle is $\alpha = 0$. Solid curve: Exact theory. Crosses: 3D numerical model.

With a breakwater, we checked our three-dimensional model (2.1.4, 2.1.6) in two different ways. First, comparison is made with the theoretical solution for a vertical circular at the head of a thin breakwater, when the incoming wave is inclined at the angle of 180°, i.e., along the breakwater. In this configuration, the semi-infinite wall is effectively absent by symmetry. A grid of 342 nodal points and 36 cubic elements is used between $k_0 r = 1$ and $k_0 r = 1.5$ and 45 expansions coefficients are used in the

	$\lvert\alpha_{00}\rvert$	$\lvert\alpha_{01}^{break}\rvert or \lvert\beta_{01}^{open}\rvert$	$\lvert\alpha_{02}^{break}\rvert or \lvert\alpha_{01}^{open}\rvert$	$\lvert\alpha_{03}^{break}\rvert or \lvert\beta_{02}^{open}\rvert$
3D open sea	0.49081	0	0.70045	0
3D breakwater	0.49084	0	0.70040	0
theory	0.49080	0	0.70054	0

Table 2.1: Coefficients of the series expansion for a 3D model of a cylinder in open sea ($ka = 1$). Comparison between a model without breakwater, a model with a thin breakwater and $\alpha = \pi$ and theory.

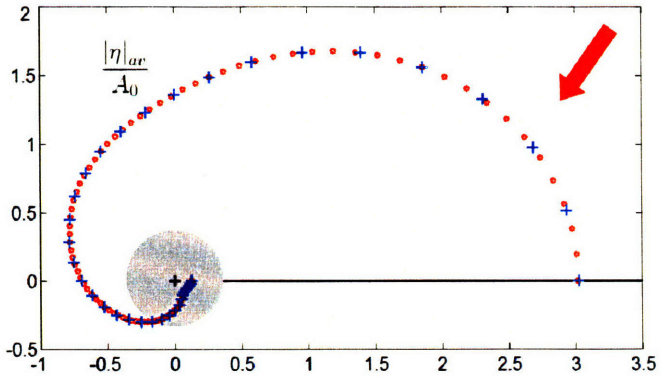

Figure 2-6: Polar plot of the maximum free-surface displacement along the wall of a vertical circular cylinder at the head of a thin breakwater. Incidence angle is $\alpha = 0.3\pi$. Circles: 2D numerical model. Crosses: 3D numerical model.

far field. The computed coefficients of all the Hankel functions of non-integer order in (2.1.6) are vanishingly small (less than 10^{-9}). The agreement with the analytical theory is again excellent - see figure (2.1).

In the second test, we used a circular cylinder at the head of a thin breakwater but for an obliquely incident wave. Numerical results from both the two and three dimensional models are compared in figure (2-6) and table (2.2). The agreement is good. The expansion coefficients of the propagating mode are matched with an accuracy of 10^{-3} and the coefficients of the first evanescent mode in the 3D model are less than 10^{-2}.

After being checked in multiple ways, this hybrid element model can now be used with confidence on the more complex geometry of the power extraction system.

	$\|\alpha_{00}\|$	$\|\alpha_{01}\|$	$\|\alpha_{02}\|$	$\|\alpha_{03}\|$	$\|\alpha_{10}\|$	$\|\alpha_{11}\|$	$\|\alpha_{12}\|$
2D model	0.4911	0.1896	0.4109	0.07688	-	-	-
3D model	0.4908	0.1904	0.4116	0.07706	0.0090	0.0159	0.0092

Table 2.2: Coefficients of the series expansion for the 2D and 3D model for a cylinder positioned at the tip of a thin breakwater. $ka = 1$; $\alpha = 0.3\pi$.

2.3 Computed Results for Foz do Douro Breakwater

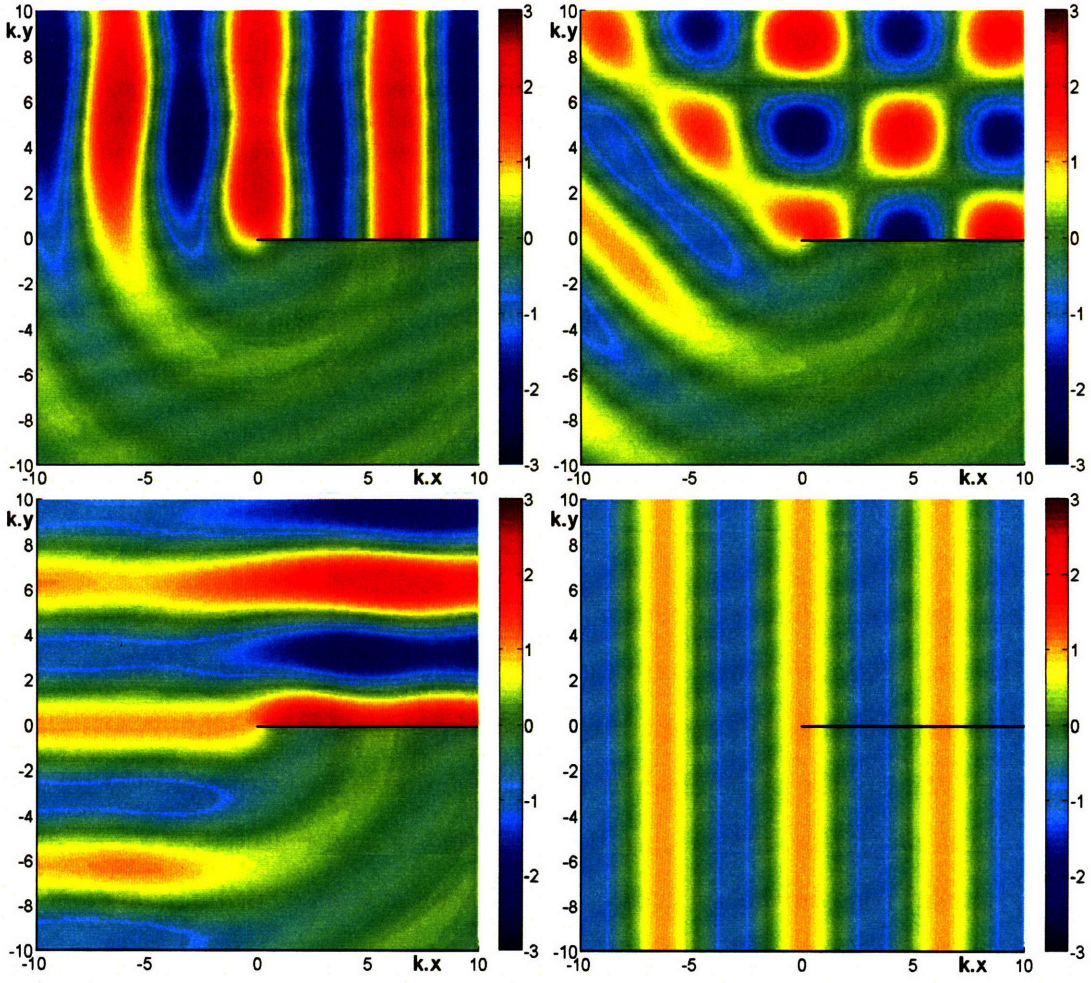

Figure 2-7: Instantaneous free-surface displacement near an infinitely thin breakwater. α is the incidence angle with respect to the breakwater. (i) $\alpha = 0$; (ii) $\alpha = \pi/4$; (iii) $\alpha = \pi/2$; $\alpha = \pi$.

In this section, the geometry of the three dimensional model is based on an early

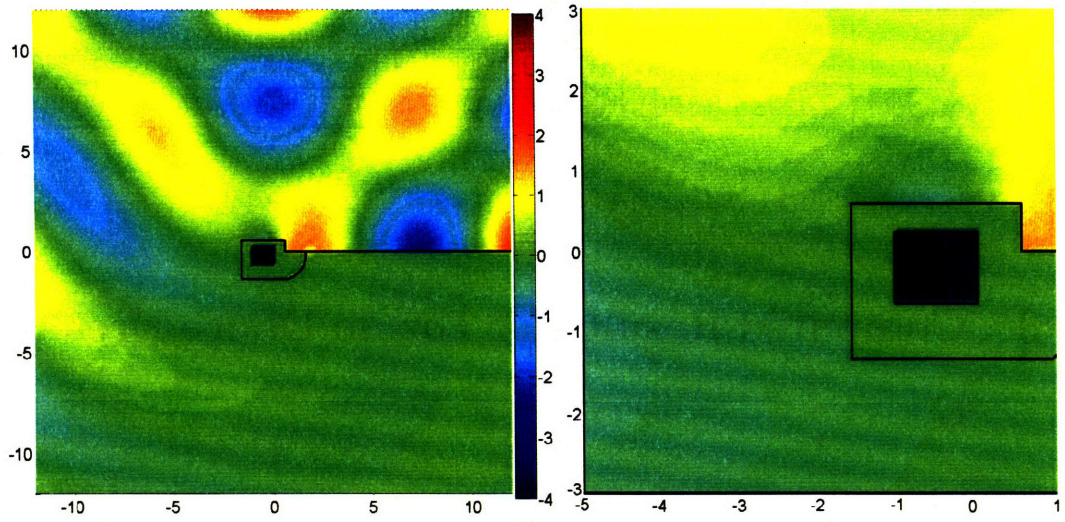

Figure 2-8: Normalized instantaneous free-surface displacement near Foz do Douro breakwater with the chamber open. Oblique incidence with $\alpha = \pi/4$ radians with respect to the breakwater. $T = 10$. Upper panel: overall view. Lower panel: Enlarged view of the breakwater head.

design described in [19, 21, 22]. The average depth outside the breakwater is 10m, the head of the breakwater has a width of 19.35m. The pneumatic chamber has the horizontal dimensions of 10x9.1m and an inside depth of 6m (see figure 2-1). The chamber opens to the sea through a wall of 3m thickness. The opening is of the same width as the breakwater head (10m) and a height of 2.66m above the inside bottom.

As a reference for later comparison, we display in figure 2-7, the diffraction pattern by a thin semi-infinite breakwater due to obliquely incident waves. There are clearly three distinct zones, roughly separated by straight rays. In the illuminated zone to the left of the tip, the plane incident wave is the dominant feature. In the reflection zone on the north side, interference between incident and reflected waves is evident. In the shadow zone on the south side, wave motion is weak. The boundaries of these zones change with the angle of incidence.

For modelling the Foz do Douro breakwater, the grid is made up of 419 cubic elements and 2583 nodal points, as seen from above in figure 2-1. Ten layers of grids are used in the vertical direction. Additional grids are implemented in the opening.

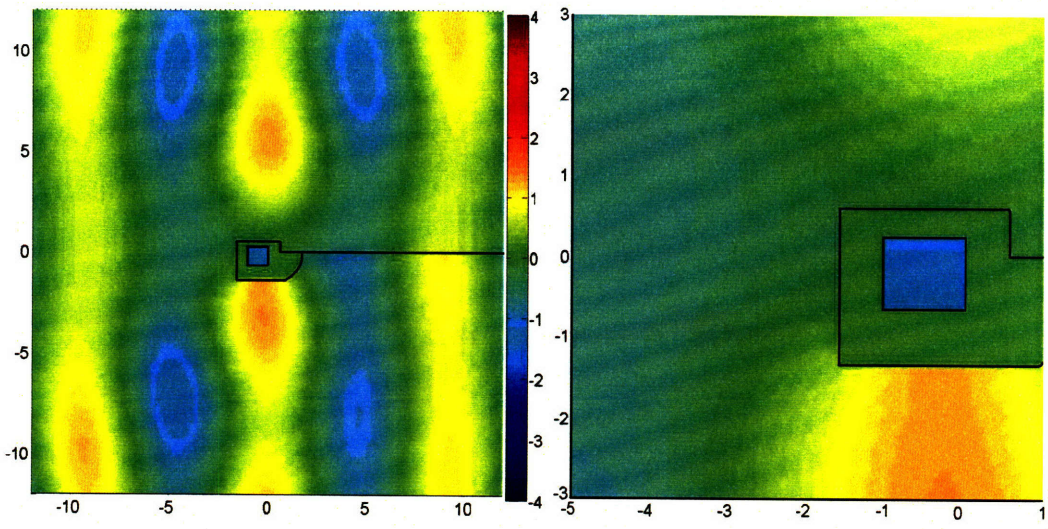

Figure 2-9: Instantaneous free-surface displacement near Foz do Douro breakwater with the chamber open. Head-sea incidence with $\alpha = \pi$ radians with respect to the breakwater. $T = 10$. Upper panel: overall view. Lower panel: Enlarged view of the breakwater head.

Almost half of the nodal points are deployed in the pneumatic chamber and the tunnel in order to assure accurate results in this most important region. In the figures to be shown, all horizontal distances are normalized by $a = 10$ m and the incident wave amplitude is taken to be $a_0 = 1$ m. We have chosen the period of 10.2 sec so that the non- dimensional period is

$$T = \frac{2\pi\sqrt{g}}{\omega\sqrt{a}} = 10. \tag{2.3.15}$$

The computed results show that far from the breakwater head, the scattering pattern is qualitatively similar to that around an infinitely thin breakwater. However, severe local effects take place in the neighbourhood of the pneumatic chamber (see figure 2-8 for oblique incidence, figure 2-9 for head-sea incidence, figure 2-10 for normal incidence and figure 2-11 for tail-sea incidence). First, for the chosen frequency, there is a strong resonance of the oscillations inside the chamber where the amplitude can reach several times the value outside. Second, the free surface displacement in the chamber is essentially uniform, implying that the resonance is of Helmholtz type, which is optimal for OWC operations. Thus the chamber dimensions are very well chosen for the design wave.

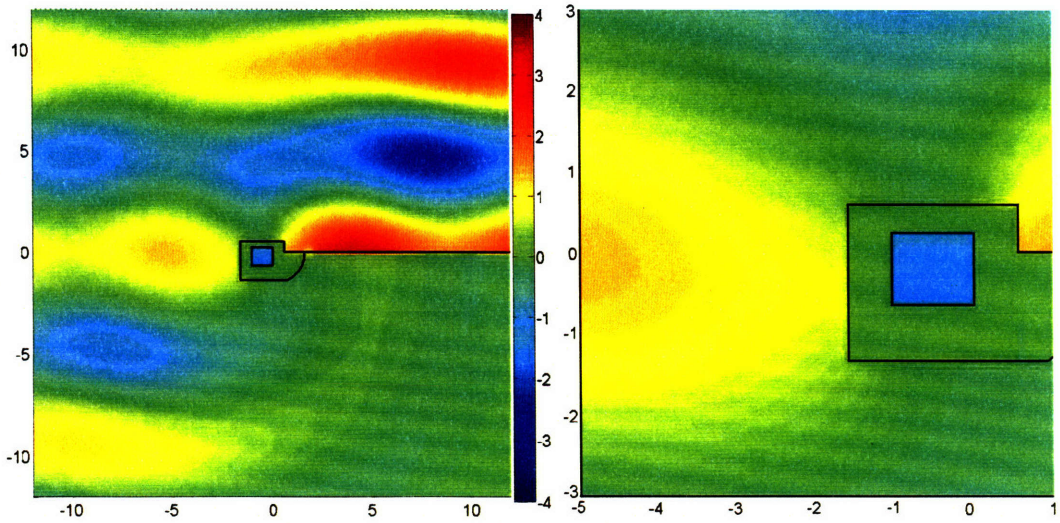

Figure 2-10: Instantaneous free-surface displacement near Foz do Douro breakwater with the chamber open. Normal incidence with $\alpha = \pi/2$ radians with respect to the breakwater. $T = 10$. Upper panel: overall view. Lower panel: Enlarged view of the breakwater head.

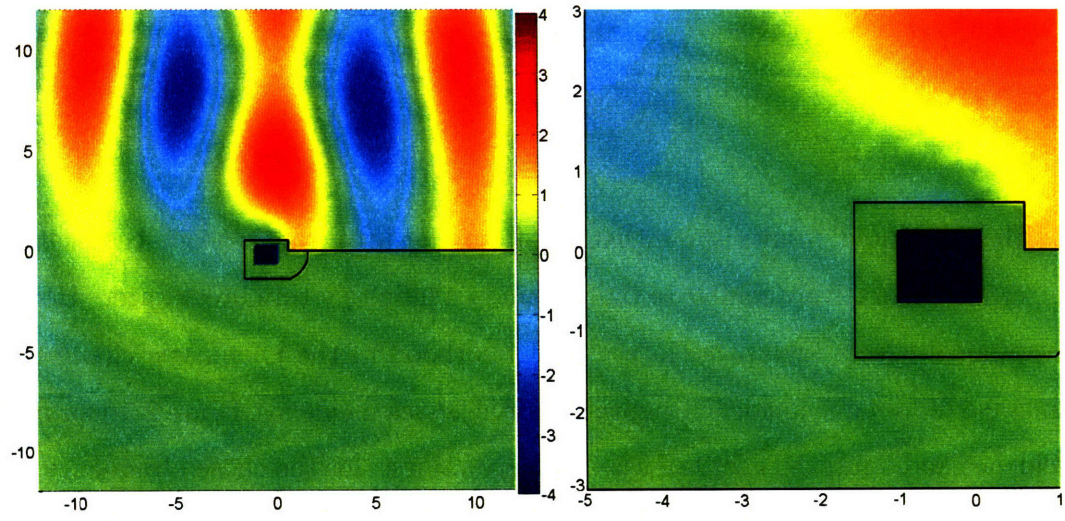

Figure 2-11: Instantaneous free-surface displacement near Foz do Douro breakwater with the chamber open. Head-sea incidence with $\alpha = 0$ radians with respect to the breakwater. $T = 10$. Upper panel: overall view. Lower panel: Enlarged view of the breakwater head.

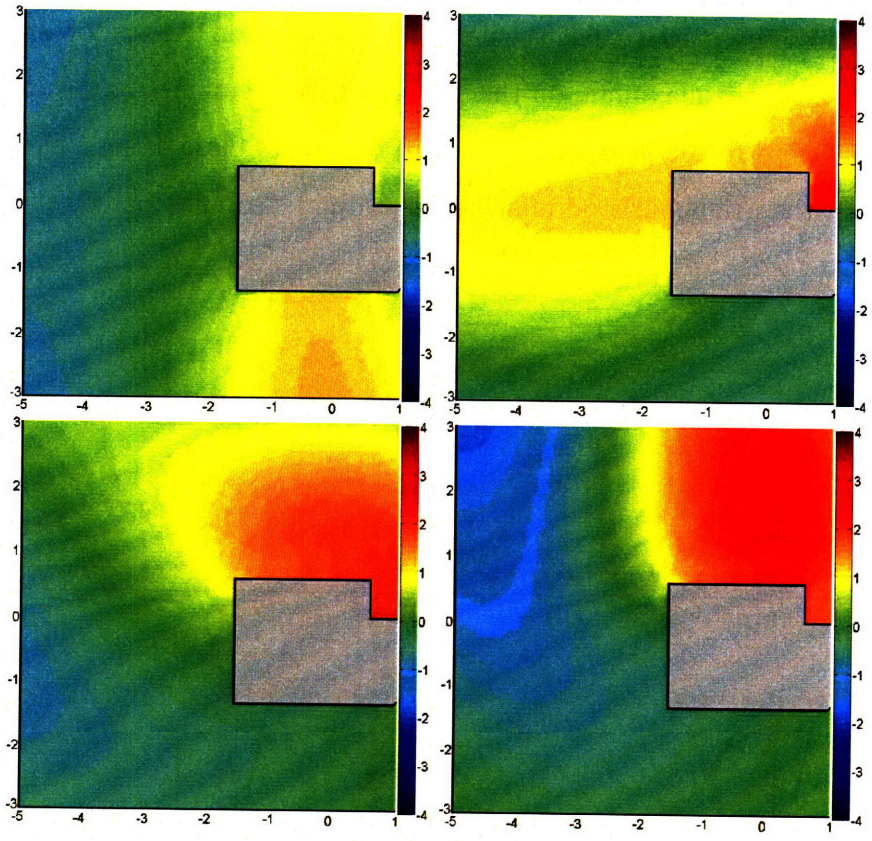

Figure 2-12: Instantaneous free-surface displacement near Foz do Douro breakwater with the chamber closed. From top down: (i). Head-sea incidence with $\alpha = \pi$ radians. (ii). Normal incidence with $\alpha = \pi/2$ radians. (iii). Oblique incidence with $\alpha = \pi/4$ radians. (iv). Tail-sea incidence with $\alpha = 0$ radians.

Note that at the entrance where there must be strong flow, the free-surface amplitude is relatively small. This is consistent with the well-known phenomenon in harbour dynamics that a node must be near the mouth of a resonating harbour. For comparison we present in figure 2-12 the diffraction pattern of the same breakwater with the chamber completely closed. The wave amplitude near the area of the closed chamber is much higher.

More detailed comparisons are shown for various angles of incidence in figure 2-13 for the water elevation along the outside wall at the stations $a - f$ as marked in figure 2-1. The influence of chamber opening on the local elevation is significant. In particular the elevation reduction by the opening is large for all angles of incidence (see stations c, d).

As expected, the free surface displacements at station e-f on the shadow side are small and the amplitude is maximum on the side the wave is coming from (between a and b for angles close to 0 and between d and e for angles close to π). The very rapid variations in the neighbourhood of sharp edges were also anticipated.

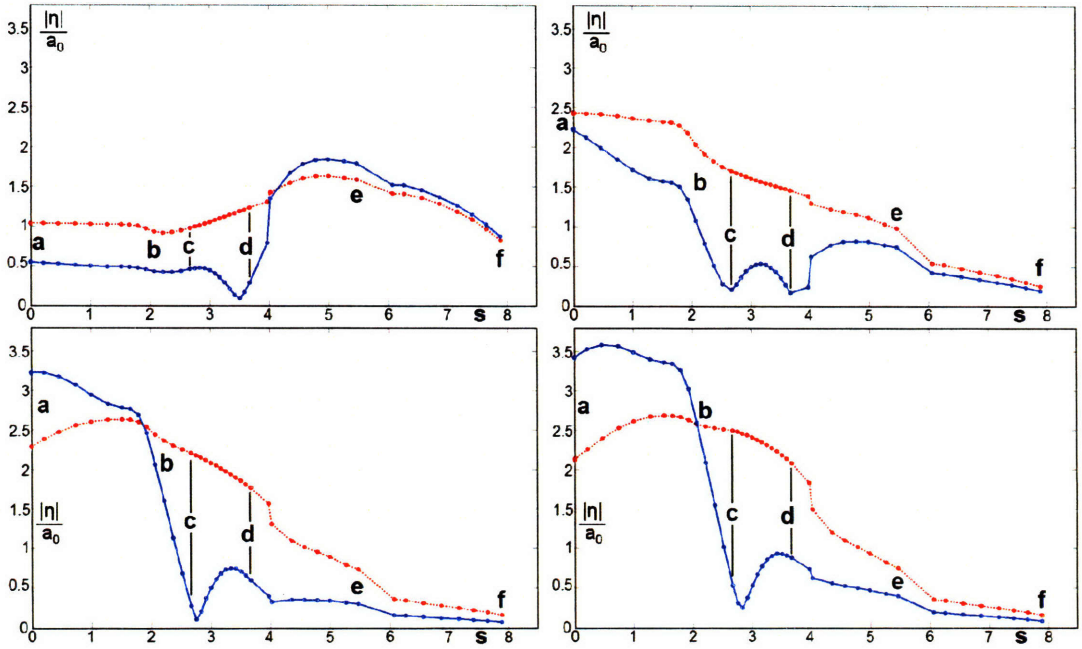

Figure 2-13: Maximum free-surface displacement along the wall of Foz do Douro breakwater's head with (solid) and without opening (dotted). The reference points (a-f) can be situated using figure 2-1. From top down: (i). Head-sea incidence with $\alpha = \pi$ radians. (ii). Normal incidence with $\alpha = \pi/2$ radians. (iii). Oblique incidence with $\alpha = \pi/4$ radians. (iv). Tail-sea incidence with $\alpha = 0$ radians.

Finally we examine the free surface elevation inside the chamber as a function of the angle of incidence. Both the horizontal average $|\eta|_{av}$ and the standard deviation from the mean σ are displayed in Figure 2-14.

$$\sigma = \frac{1}{S} \iint_S ||\eta| - |\eta|_{av}| \, dS \tag{2.3.16}$$

The average response in the chamber is monotonous - larger for small angles of incidence with respect to the breakwater and smaller for angles close to π. The deviation from the mean is always small. This is a surprising result since an optimum for a normal incidence could have been expected. Here, the amplitude is twice as

large for a tail-sea incidence ($\alpha = 0$) than for a head-sea incidence ($\alpha = \pi$). This can actually be also clearly seen from the wave pattern for both angles - figures (2-11) and (2-9). According to local wind-wave records the predominant incoming wave has the

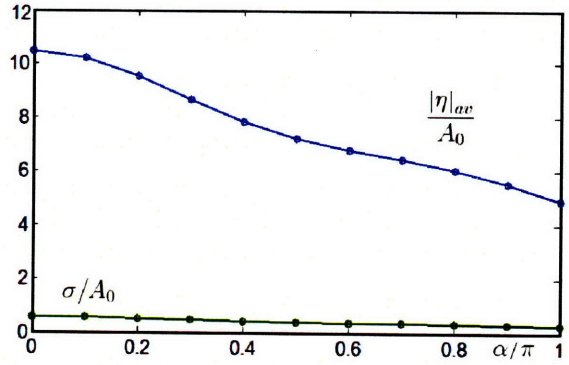

Figure 2-14: Dependence of the free surface displacement inside the chamber on the angle of incidence. Average and standard deviation for $T = 10$.

period of 10s and the direction of 125° with respect to the breakwater. Figure 2-15 shows the dependence of chamber response to incident waves of different periods, all for the same angle of incidence. Resonance occurs here at $T \cong 10.75$, showing that the chamber dimensions are near optimum.

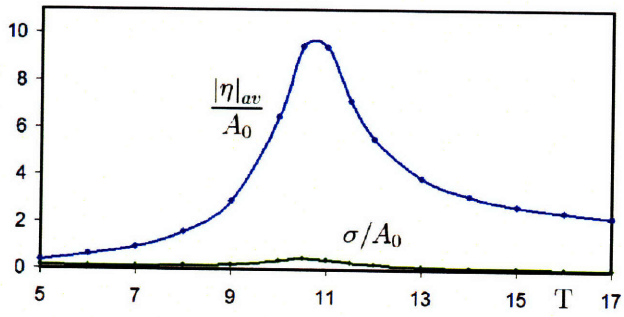

Figure 2-15: Dependence of the free surface displacement inside the chamber on the period of incoming sea. Average and standard deviation for $\alpha = 125°$.

These results also indicate that the free surface elevation amplitude inside the chamber can potentially be one order of magnitude larger than the incident wave. This might be a limitation to the use of this linear theory. Thus, it may be necessary to account for nonlinearities in the future. Our ideas for modelling separation loss are sketched below.

2.4 Modeling of Separation Loss

Given the geometry of the problem which includes sharp angles and ducts, it seems necessary to account for separation loss. This section aims at outlining a possible approach to the problem.

Deliberate use of flow separation is the basis for designing perforated wall panels for sound absorption, perforated or slotted breakwaters for wave attenuation [27] and thin breakwaters at the mouth of an estuary for tsunami dissipation [28]. Theoretical modelling of this effect can be found in [29] and [3]. The essential idea is to represent the energy loss by the pressure drop across the opening. In terms of the flow velocity u through the opening, the pressure difference across the mouth is,

$$g(\zeta_- - \zeta_+) = \frac{f}{2}u|u| + L\frac{\partial u}{\partial t} \tag{2.4.17}$$

where ζ_- and ζ_+ are the wave heights inside and outside the chamber, respectively, f is the friction coefficient and L the total effective thickness of the walls (including the apparent thickness due to hydrodynamics). In principle this is a nonlinear relation even for infinitesimal waves. The method of equivalent linearization can be used to make the mathematics linear and to preserve the quadratic dependence on the velocity amplitude. This is achieved by rewriting (2.4.17) in linear form:

$$g(\zeta_- - \zeta_+) = C_e u + L\frac{\partial u}{\partial t} \tag{2.4.18}$$

The coefficient C_e is chosen so that the period-averaged energy dissipation rate is the same by using either (2.4.17) or (2.4.18). This gives:

$$C_e = \frac{f}{2}\frac{\overline{u^2|u|}}{\overline{u^2}} \tag{2.4.19}$$

which depends on the amplitude of u, hence preserves some features of nonlinearity.

The friction coefficient depends on the local geometry of the opening (roundedness

of corners etc.) and must be found by experiment. The effective length L depends on fluid motion and is a part of the theory. A crude estimate can be given as follows. In the proposed design the chamber and the opening are very small compared to a wavelength, hence the resonance is of Helmholtz type and the water level inside the chamber is essentially uniform as confirmed by the numerical model. Let S_C denote the horizontal area of the chamber and S_o the area of the opening. It follows by mass conservation that

$$S\frac{\partial \zeta_-}{\partial t} = -uS_o \tag{2.4.20}$$

In (2.4.18) the effective hydrodynamic length L can be found approximately from the resonant period or frequency by first ignoring the effect of friction loss and assuming that a node exists outside the opening when resonance occurs, i.e. $\zeta_- \gg \zeta_+$. The momentum equation gives

$$g\zeta_- = L\frac{\partial u}{\partial t} \tag{2.4.21}$$

It follows that

$$\frac{\partial^2 \zeta_-}{\partial t^2} + \frac{S_o}{S_C} gL\zeta = 0 \tag{2.4.22}$$

so that the resonance frequency is

$$\omega_H = \sqrt{\frac{gS_o}{LS}} \quad \text{implying} \quad L = \frac{gS_o}{\omega_H^2 S_C}. \tag{2.4.23}$$

In a numerical model, the resonance frequency is a result of the diffraction theory. The above formula gives the value of L as the first approximation, valid near resonance. Clearly L depends on frequency.

2.5 Conclusion

The present numerical scheme based on linearized theory gives quantitative information about the effects of diffraction on the response inside the OWC chamber. Our results provide evidence that the dimensions of the chamber are well chosen for the predominant wave period and direction. However, the predicted amplitude of

water-level inside the chamber is very large at resonance, suggesting the need for considering additional factors. For example, separation losses and broad frequency band may contribute to the reduction of the resonant amplification.

The results also show that the breakwater affects the wave pattern locally depending on the angle of incidence. In the following chapters we examine idealized geometries which allow for analytical modeling with view to better physical understanding.

Chapter 3

Circular OWC at the Tip of a Thin Breakwater

This chapter aims at providing a complete model for an OWC system whose geometry is an idealized version of the Ceodouro project. A simple circular geometry allows analytical models for both the radiation and scattering problems by using eigenfunctions and integral equations. The hydrodynamics can then be coupled with a model of the power take-off system to predict the extracted power and efficiency.

We shall consider here an OWC system consisting of a hollow circular cylinder of radius a connected to a breakwater. The cylinder is open to the sea at the bottom and rises to certain height above the mean sea level. A system of Wells turbines is installed on top of the cylinder. Energy is converted by the turbine which rotates in only one direction under the oscillating air pressure. This is sketched in Figure 3-1. We assume the sea depth h to be constant, and the walls of the coast and structure are vertical. Waves coming with the angle of incidence α are monochromatic and of small amplitude so that the linearized theory applies.

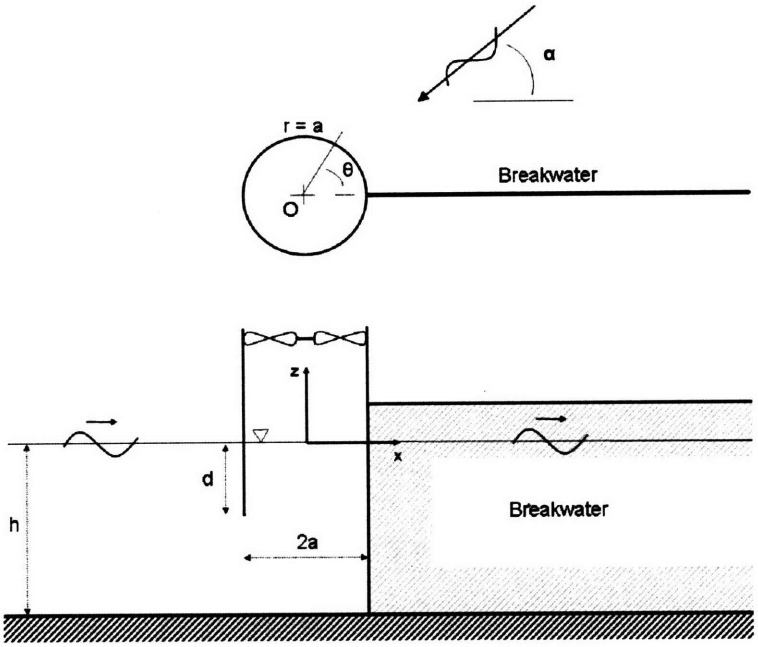

Figure 3-1: OWC at the head of a breakwater.

3.1 Model of Power Take-off

Let us assume that one or more Wells turbines are installed at the top of the cylinder. Due to the high sound speed in air and the low frequency of sea waves, we assume that the air pressure p_a is approximately uniform throughout the chamber. We also approximate that the mass flux through the Wells turbines is proportional to the chamber air pressure. Following Sarmento & Falcao [14] we relate the mass flux of air to the turbine characteristic by:

$$\frac{d(\rho_a V)}{dt} = \frac{KD}{N} p_a \tag{3.1.1}$$

where ρ_a is the air density, V the volume, N the rotational speed of turbine blades and D the turbine rotor outer diameter. The empirical factor K depends on the design, numbers and setup of turbines. For a single turbine the usual range of the proportionality constant K is 0.4–0.6. Accounting for air compressibility, the rate of

mass change in the chamber is,

$$\frac{d(\rho_a V)}{dt} = \rho_a \frac{dV}{dt} + V \frac{d\rho_a}{dt} \tag{3.1.2}$$

dV/dt is the rate of total upward displacement of the water surface

$$\frac{dV}{dt} = Q = \int_0^a \int_0^{2\pi} w(r, \theta, z = 0, t) r dr\, d\theta \equiv \iint_{S_c} w\, dS \tag{3.1.3}$$

where S_c denotes the water surface in the chamber. Assuming isentropy so that $c_a^2(d\rho_a/dt) = dp_a/dt$ where c_a is the sound velocity in air, this gives,

$$\frac{dM}{dt} = \rho_a^0 Q - \frac{V_o}{c_a^2} \frac{dp_a}{dt} \tag{3.1.4}$$

Then, for simple harmonic motion with $Q = \Re(\widehat{Q} e^{-i\omega t}), p_a = \Re(\widehat{p}_a e^{-i\omega t})$:

$$\widehat{Q} = \left(\frac{KD}{N\rho_a^0} - \frac{i\omega V_o}{c_a^2 \rho_a^0} \right) \widehat{p}_a \tag{3.1.5}$$

as in Sarmento & Falcao [14].

For small waves the linearized velocity potential in water can be treated as the sum of radiation and diffraction problems. The upward flux at the water surface is made up of two parts

$$\widehat{Q} = \widehat{Q}^R + \widehat{Q}^D \tag{3.1.6}$$

where $\widehat{Q}^R$ and $\widehat{Q}^D$ are respectively contributions from the radiation and diffraction potentials, both of which will be analyzed in detail in subsequent sections. We express these two contributions as

$$\widehat{Q}^R \equiv -(\mathcal{B} - i\mathcal{C})\, \widehat{p}_a, \quad \text{with } \mathcal{B} \text{ and } \mathcal{C} \text{ real} \quad ; \quad \widehat{Q}^D \equiv \Gamma A_0 \tag{3.1.7}$$

where A_o is the incident wave amplitude. Physically $\mathcal{C}$ is in phase with the flux acceleration and amounts to the added hydrodynamic inertia (i.e., the radiation susceptance). On the other hand, $\mathcal{B}$ is in phase with the flux velocity amounting to

radiation damping (i.e., radiation conductance). The quantities $\mathcal{B}, \mathcal{C}$ and Γ will be computed in later sections.

Combining (3.1.5) and (3.1.7), we obtain

$$\frac{\widehat{p}_a}{A_0} = \frac{\Gamma}{\left[\left(\frac{KD}{N\rho_a^0} + \mathcal{B}\right) - i\left(\mathcal{C} + \frac{\omega V_o}{c_a^2 \rho_a^0}\right)\right]} \tag{3.1.8}$$

The time-averaged power output to the turbine is:

$$P_{out} = \overline{\frac{d(\rho_a V)}{dt}\frac{p_a}{\rho_a}} = \frac{KD}{N\rho_a^0}\overline{p_a^2} = \frac{KD}{2N\rho_a^0}\left|\widehat{p}_a\right|^2 \tag{3.1.9}$$

Thus:

$$P_{out} = \frac{KD}{2N\rho_a^0}\frac{|\Gamma|^2 A_o^2}{\left(\frac{KD}{N\rho_a^0} + \mathcal{B}\right)^2 + \left(\mathcal{C} + \frac{\omega V_o}{c_a^2\rho_a^0}\right)^2} \tag{3.1.10}$$

We shall use the normalized capture length as the measure of extraction efficiency:

$$\begin{aligned} kL &= \frac{2kP_{out}}{\rho g A_0^2 C_g} = \frac{KD}{N\rho_a}\frac{|\Gamma|^2}{\left(\frac{KD}{N\rho_a} + \mathcal{B}\right)^2 + \left(\mathcal{C} + \frac{\omega V_o}{c_a^2\rho_a^0}\right)^2}\frac{k}{\rho g C_g} \\ &= \frac{gka}{\omega C_g}\frac{\chi|\widetilde{\Gamma}|^2}{\left(\chi + \widetilde{\mathcal{B}}\right)^2 + \left(\widetilde{\mathcal{C}} - \beta\right)^2} \end{aligned} \tag{3.1.11}$$

$\widetilde{\Gamma}, \widetilde{\mathcal{B}}$ and $\widetilde{\mathcal{C}}$ are the dimensionless counterparts of $\Gamma, \mathcal{B}, \mathcal{C}$

$$\Gamma = \widetilde{\Gamma}\left(\frac{ag}{\omega}\right), \quad (\mathcal{B}, \mathcal{C}) = (\widetilde{\mathcal{B}}, \widetilde{\mathcal{C}})\left(\frac{a}{\omega\rho_w}\right) \tag{3.1.12}$$

and

$$\chi = \frac{\rho_w KD\omega}{\rho_a N a}, \quad \beta = -\frac{\omega^2 V_o \rho_w}{c_a^2 a \rho_a} \tag{3.1.13}$$

The parameter χ characterizes the turbines while β represents the effects of compressibility and chamber volume and is analogous to a spring of negative elasticity which varies with ω^2. As noted by Sarmento & Falcao in [14], this springlike effect of compressibility is equivalent to adding an imaginary term to the turbine proportionality constant K, thus introducing a non-zero phase difference between the mass flow rate and the pressure.
As an estimate we take $\omega = 0.5$ rad/s, a=10 m, $V_o = 10^3$ m^3, and $\rho_w/\rho_a = 10^3$, then $\beta = 0.43$ which shows the importance of air compressibility. We shall assume that he magnitude of χ can be controlled by proper design.

We now solve the radiation and diffraction problems. For easy distinction we shall denote the radiation potential by ϕ and the diffraction potential by φ.

3.2 Radiation Problem

3.2.1 Analysis

The velocity potentials both inside (ϕ_C) and outside (ϕ_O) the cylindrical column are axially symmetric and governed by the three-dimensional Laplace equation. As in earlier theories, we approximate the unknown air pressure in the chamber to be uniform in space but sinusoidal in time. Outside the cylinder, the air is calm. The linearized boundary condition on the water surface is

$$\left(\frac{\partial}{\partial z} - \frac{\omega^2}{g}\right) \left\{ \begin{array}{c} \phi_C \\ \phi_O \end{array} \right\} = \left\{ \begin{array}{ll} \frac{i\omega}{\rho g}\widehat{p}_a, & z = 0, \quad r < a; \\ 0, & z = 0, \quad r > a. \end{array} \right. \tag{3.2.1}$$

In addition to the no flux condition on all solid boundaries, ϕ_O must behave as outgoing waves in the far field. Together with the Laplace equation, these conditions constitute the radiation problem, which was first solved by Evans and Porter [16].

Let k be the the positive real root, and κ_ℓ, $\ell = 1, 2, 3, ...$ the positive imaginary

roots of the dispersion relation, i.e.,

$$\omega^2 = gk\tanh kh. \quad -\omega^2 = g\kappa_\ell \tan \kappa_\ell h, \quad \ell = 1,2,3,... \tag{3.2.2}$$

and let $Z_0(z)$ and $Z_\ell(z)$ be the corresponding eigen-functions

$$Z_0(z) = \frac{\cosh k(z+h)}{N_0^{1/2}}, \quad N_0 = \frac{1}{2}\left[1 + \frac{\sinh 2kh}{2kh}\right] \tag{3.2.3}$$

and

$$Z_\ell(z) = \frac{\cos \kappa_\ell(z+h)}{N_\ell^{1/2}}, \quad N_\ell = \frac{1}{2}\left[1 + \frac{\sin 2\kappa_\ell h}{2\kappa_\ell h}\right], \quad \ell = 1,2,3,... \tag{3.2.4}$$

which are orthogonal in $-h < z < 0$

$$\int_{-h}^{0} Z_\ell(z) Z_m(z)\, dz = h\delta_{\ell m}, \quad \ell, m = 0,1,2,3,\cdots \tag{3.2.5}$$

All $Z_\ell(z)$ satisfy the homogeneous version of relation (3.2.1) as well as the no flux boundary condition at the bottom. For brevity we shall define $k = i\kappa_0$ and include $Z_0(z)$ as a member of the set of (3.2.4) with $\ell = 0$.

The potential inside the cylinder can then be expressed as an infinite series of modified Bessel functions, solution of the Laplace equation and non-singular at the origin:

$$\phi_C = \frac{-i\widehat{p}_a}{\rho\omega} \sum_{\ell=0}^{\infty} D_\ell \frac{I_0(\kappa_\ell r)}{\kappa_\ell a\ I_0'(\kappa_\ell a)} Z_\ell(z) - \frac{i\widehat{p}_a}{\rho\omega} \tag{3.2.6}$$

The outside potential can be expressed as another infinite series of modified Bessel functions, again the solution of the Laplace equation but outgoing at infinity:

$$\phi_O = \frac{-i\widehat{p}_a}{\rho\omega} \sum_{\ell=0}^{\infty} E_\ell \frac{K_0(\kappa_\ell r)}{\kappa_\ell a\ K_0'(\kappa_\ell a)} Z_\ell(z) \tag{3.2.7}$$

Note that terms associated with $\ell = 0$ are wave-like

$$I_0(\kappa_0 r) = J_0(kr), \quad K_0(\kappa_0 r) = \frac{\pi}{2} i H_0^{(1)}(kr) \tag{3.2.8}$$

while terms with $\ell = 1, 2, 3, ...$ are evanescent modes.

The unknown coefficients D_ℓ and E_ℓ must be chosen to ensure the continuity of radial flux and potential on the open part of the column surface,

$$\frac{\partial \phi_O}{\partial r} = \frac{\partial \phi_C}{\partial r} \equiv U(z), \quad \text{and} \quad \phi_O = \phi_C; \quad r = a, \quad -h < z < -d. \tag{3.2.9}$$

The first matching condition (3.2.9) requires that

$$E_\ell = D_\ell = \frac{ia\rho\omega}{\widehat{p}_a h} \int_{-h}^{-d} U(z) Z_\ell(z) dz \qquad \ell = 1, 2, 3, ... \tag{3.2.10}$$

while the second leads to an integral equation for $U(z)$ for $-h < z < -d$:

$$\int_{-h}^{-d} U(z') \mathcal{K}(z, z') dz' = -\frac{i\widehat{p}_a}{a\rho\omega} \tag{3.2.11}$$

with the kernel

$$\mathcal{K}(z, z') = \frac{1}{h} Z_\ell(z') \left(\frac{K_0(\kappa_\ell a)}{\kappa_\ell a \; K_0'(\kappa_\ell a)} - \frac{I_0(\kappa_\ell a)}{\kappa_\ell a \; I_0'(\kappa_\ell a)} \right) Z_\ell(z) \tag{3.2.12}$$

To solve for $U(z)$ which is expected to be singular at $z = -d$, we follow Porter & Evans [30] by taking

$$U(z) = \frac{-i\widehat{p}_a}{\rho\omega} \sum_{n=0}^{\infty} \alpha_n u_n(z) \qquad \text{with} \qquad u_n(z) = \frac{2(-1)^n}{\pi \sqrt{(h-d)^2 - (z+h)^2}} T_{2n}\left(\frac{z+h}{h-d} \right) \tag{3.2.13}$$

where T_n is the Chebychev polynomials of order n. Only even polynomials are used in order to ensure that there is no vertical flux at the sea bottom.

With the help of the following identity [31]:

$$\int_{-h}^{-d} u_n(z)Z_\ell(z)dz = N_\ell^{-1/2} J_{2n}\{\kappa_\ell(h-d)\} \equiv F_{n\ell} \tag{3.2.14}$$

(3.2.11) is reduced to a matrix equation for the expansion coefficients α_n,

$$\sum_{n=0}^{\infty} \mathcal{A}_{pn}\alpha_n \equiv \sum_{n=0}^{\infty}\left[\sum_{\ell=0}^{\infty} F_{n\ell}\left(\frac{K_0(\kappa_\ell a)}{\kappa_\ell a\, K_0'(\kappa_\ell a)} - \frac{I_0(\kappa_\ell a)}{\kappa_\ell a\, I_0'(\kappa_\ell a)}\right)F_{p\ell}\right]\alpha_n = \frac{h}{a}\delta_{p0} \tag{3.2.15}$$

From here all series are summed over all integers from 0. Once α_n's are calculated numerically, $U(z)$ is calculated from (3.2.13), and the coefficients $E_n = D_n$ from (3.2.10).

3.2.2 Energy Conservation

Numerical solutions of the algebraic system have been validated by checking the identity of energy conservation that the power input by the chamber air must equal the power outflux across a vertical cylindrical surface around the column:

$$\overline{P\iint_{S_c} -\frac{\partial\Phi}{\partial z}\bigg|_{z=0} dS} = \overline{\iint_{S_R} -\rho\frac{\partial\Phi}{\partial t}\frac{\partial\Phi}{\partial r}dS} \tag{3.2.16}$$

Invoking the eigenfunction expansions, the left-hand side equals

$$\Re\left\{\frac{i\pi\left|\widehat{p}_a\right|^2}{\rho\omega}\int_0^a \sum_\ell D_\ell \frac{I_0(\kappa_\ell r)}{\kappa_\ell a\, I_0'(\kappa_\ell a)} Z_\ell'(0) r dr\right\} \tag{3.2.17}$$

Taking the radius of S_R to be very large, the right-hand side involves only the propagating modes and becomes

$$\begin{aligned}\frac{1}{2}\Re\left\{\iint_{S_\infty} \rho i\omega\phi_O\frac{\partial\phi_O^*}{\partial r}dS\right\} &= \lim_{r\to\infty}\Re\left\{\int_{-h}^{0}\frac{i\pi^3 h\left|\widehat{p}_a\right|^2\left|E_0\right|^2}{4ka^2\rho\omega\left|K_0'(\kappa_0 a)\right|^2}H_0(kr)H_0'^*(kr)rdz\right\}\\ &= \frac{\left|\widehat{p}_a\right|^2 h}{\rho\omega}\frac{2\left|E_0\right|^2}{(ka)^2\left|H_0'(ka)\right|^2}\end{aligned} \tag{3.2.18}$$

This equality of (3.2.17) and (3.2.18) has been checked using the numerically computed coefficients D_ℓ and E_0 as shown in table (3.1).

ka	0.089	0.276	0.359	0.387	0.397	0.403
W(3.2.18)	0.000399	0.062167	0.868372	7.141401	10.64467	7.666883
W(3.2.17)	0.000399	0.062168	0.868373	7.141416	10.64469	7.666898

Table 3.1: Radiated power W (Eq. 3.2.24) obtained by computation using equation (3.2.17) and equation (3.2.18) for different values of ka. $a/h = 0.1$; $d/h = 0.2$.

Let us note that relation (3.2.16) can be derived mathematically. By Green's formula:

$$\iiint_V \left[\phi \nabla^2 \phi^* - \phi^* \nabla^2 \phi\right] dV = \iint_S \left[\phi \frac{\partial \phi^*}{\partial n} - \phi^* \frac{\partial \phi}{\partial n}\right] dS \tag{3.2.19}$$

where V is the fluid volume inside the cylindrical surface S_∞, and $S = S_\infty \cup S_F \cup S_C \cup S_B$, is the bounding surface of V. The volume integral on the left vanishes by virtue of the Laplace equation. On the right-hand side, the surface integrals over solid boundaries $S_C \cup S_B$ are zero due to the no-flux condition. On the free surface inside the column, the surface integral is non-zero, hence :

$$\Im\left\{2\pi \int_{r<a,z=0} \phi \frac{\partial \phi^*}{\partial z} r dr\right\} = -\Im\left\{\iint_{S_\infty} \phi \frac{\partial \phi^*}{\partial r} dS\right\} \tag{3.2.20}$$

Using (3.2.1), the left side can be rewritten as:

$$\Im\left\{2\pi \int_{r<a,z=0} \frac{iP}{\rho\omega} \frac{\partial \phi^*}{\partial z} r dr + 2\pi \int_{r<a,z=0} \frac{-g}{\omega^2} \frac{\partial \phi}{\partial z} \frac{\partial \phi^*}{\partial z} r dr\right\} = -\Im\left\{\iint_{S_\infty} \phi \frac{\partial \phi^*}{\partial r} dS\right\} \tag{3.2.21}$$

Since $\frac{\partial \phi}{\partial z}\frac{\partial \phi^*}{\partial z} = \left|\frac{\partial \phi}{\partial z}\right|^2$ is real and P is constant, this yields:

$$\Re\left\{-2\pi P \int_{r<a,z=0} \frac{\partial \phi}{\partial z} r dr\right\} = \Re\left\{\iint_{S_\infty} \rho i\omega \phi \frac{\partial \phi^*}{\partial r} dS\right\} \tag{3.2.22}$$

which is the same statement of energy balance derived from physical arguments (3.2.16).

3.2.3 Numerical Results

All convergence aspects of the numerical implementation will be addressed in section (3.3.3). We will focus here on the physical discussion of the results.

For the radiation problem we shall present results for the normalized free surface displacement in and near the oscillating water column,

$$\begin{aligned} \frac{\eta_C}{P/\rho g} &= \frac{i\omega\rho\,\phi_C|_{z=0}}{P} - 1 \qquad , \quad 0 < r < a \\ \frac{\eta_O}{P/\rho g} &= \frac{i\omega\rho\,\phi_O|_{z=0}}{P} \qquad , \quad r > a \end{aligned} \tag{3.2.23}$$

for a given surface pressure P. The non dimensional radiated power at infinity can be defined to be :

$$W = \frac{\rho\omega}{2aP^2}\overline{\iint_{S_\infty} p\frac{\partial\phi}{\partial r}dS} \tag{3.2.24}$$

In order to evaluate later the energy extracted by the turbine, it is necessary to obtain the coefficients $\widetilde{\mathcal{B}}$ and $\widetilde{\mathcal{C}}$. Let's recall from (3.1.7):

$$Q^R = -(\mathcal{B} - i\mathcal{C})p_a = \iint_{S_c} \left.\frac{\partial\phi_C}{\partial z}\right|_{z=0} dS \tag{3.2.25}$$

so that

$$\widetilde{\mathcal{B}} = \Re\left\{\iint_{S_c}\sum_\ell \frac{iD_\ell}{a}\frac{I_0(\kappa_\ell r)}{\kappa_\ell a\, I_0'(\kappa_\ell a)}Z_\ell'(0)dS\right\} \tag{3.2.26}$$

$$\widetilde{\mathcal{C}} = -\Im\left\{\iint_{S_c}\sum_\ell \frac{iD_\ell}{a}\frac{I_0(\kappa_\ell r)}{\kappa_\ell a\, I_0'(\kappa_\ell a)}Z_\ell'(0)dS\right\} \tag{3.2.27}$$

For a fixed depth h but several OWC sizes a/h, the numerical values of these coefficients are plotted in Figure 3-2. Note that, contrary to the case of a rigid floating

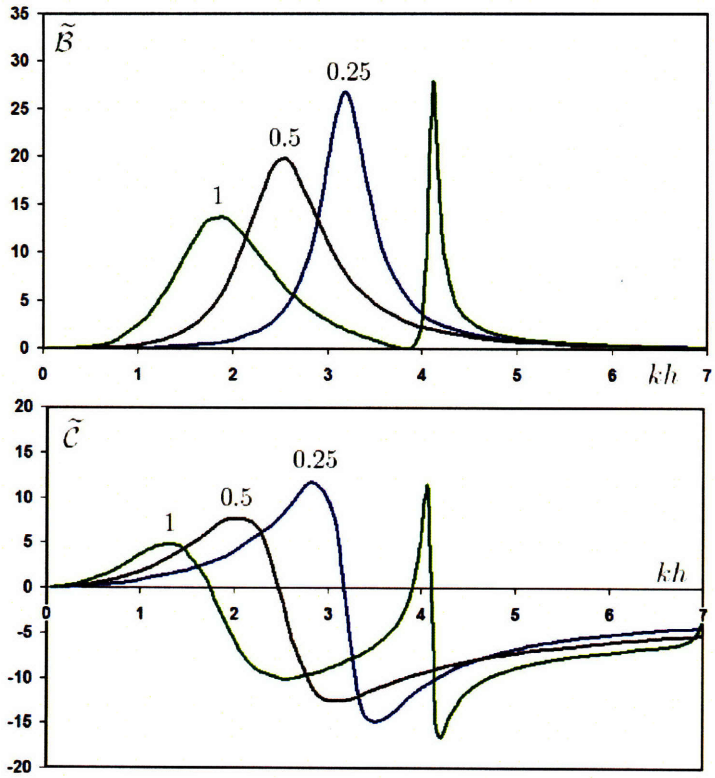

Figure 3-2: (i) Radiation damping and (ii) added mass against the normalized frequency kh for $a/h =$ 0.25 , 0.5 , 1. In all cases $d/h = 0.2$.

body, the added mass $\widetilde{\mathcal{C}}$ changes sign here. This is an important characteristic feature of OWC systems already acknowledged [12, 13, 14]. The radiation damping coefficient reaches a maximum at a resonance frequency. Both the frequency and the amplitude of the resonance peak decrease with increasing a/h. On the other hand, larger radii lead to larger peak width. Physically, as a/h becomes smaller, the fluid inside the OWC tends to follow a solid body motion and behaves like a piston. In this limiting case an hydrostatic approximation predicts resonance at $kd\tanh(kh) = 1$ (which corresponds to $kh \approx 5$). This trend is indeed confirmed by the computed results as the radius of the OWC gets smaller.

If a/h is sufficiently large there can be more peaks separated by zeros[1] of $J_0'(ka)$ where there is no radiation, i.e. $\widetilde{\mathcal{B}} = 0$ due to destructive interference. Similarly to the two dimensional theory of Stoker [26], these zeroes can be confirmed by solving

[1]The first three zero of $J_0'(ka)$ are at $ka = 3.83, 7.02, 10.17$.

analytically the simpler problem of forced radiation by an oscillating pressure over a circular area of the free surface (see also Appendix C).

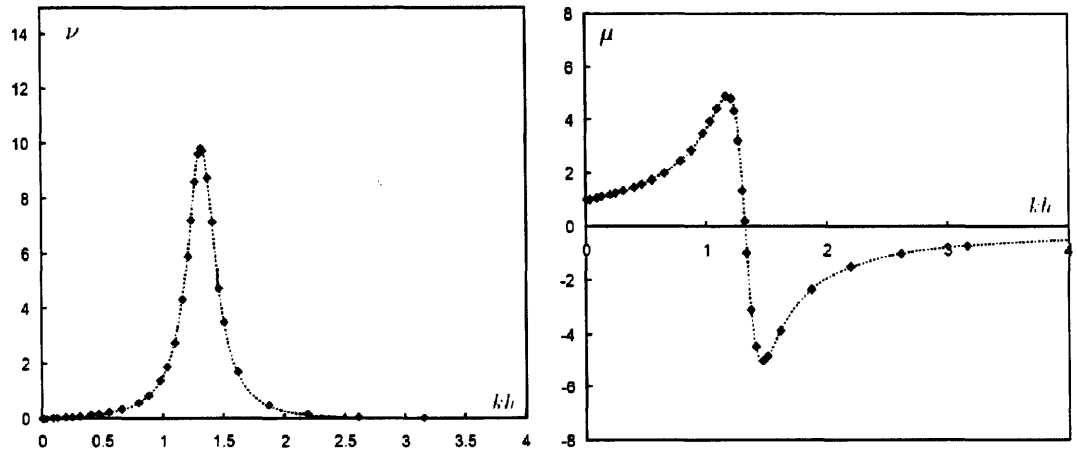

Figure 3-3: Nondimensional (i) radiation damping and (ii) added mass as defined by Evans and Porter against the normalized frequency kh for $d/h = 0.5$ and $a/h = 0.5$. Dotted line: Results of Evans & Porter. Diamonds: present computation.

Our computations have been compared with earlier results of Evans and Porter [16]. The agreement is excellent, as seen in Figure 3-3 where μ and ν are defined as:

$$(\nu;\mu) = \frac{g}{\pi a\omega^2}\left(\widetilde{\mathcal{B}};\widetilde{\mathcal{C}}\right) \tag{3.2.28}$$

Figure 3-4 shows the effects of draft d/h for a fixed radius $a/h = 0.5$. Clearly smaller d/h (i.e. larger opening) leads to lower and flatter curves of $\widetilde{\mathcal{B}}$ and $\widetilde{\mathcal{C}}$. It is interesting that a larger opening gives a larger frequency bandwidth.

Another important aspect of the problem is the free surface elevation, especially inside the cylinder. It can be observed in figure (3-5) that the behaviour of the elevation amplitude average is qualitatively similar to that of the radiation damping. For long periods, the limit is $\left|\frac{\eta_{av}}{P/\rho g}\right| = 1$ which corresponds to the hydrostatic equilibrium. As kh increases, the elevation goes through a maximum and then decreases slowly

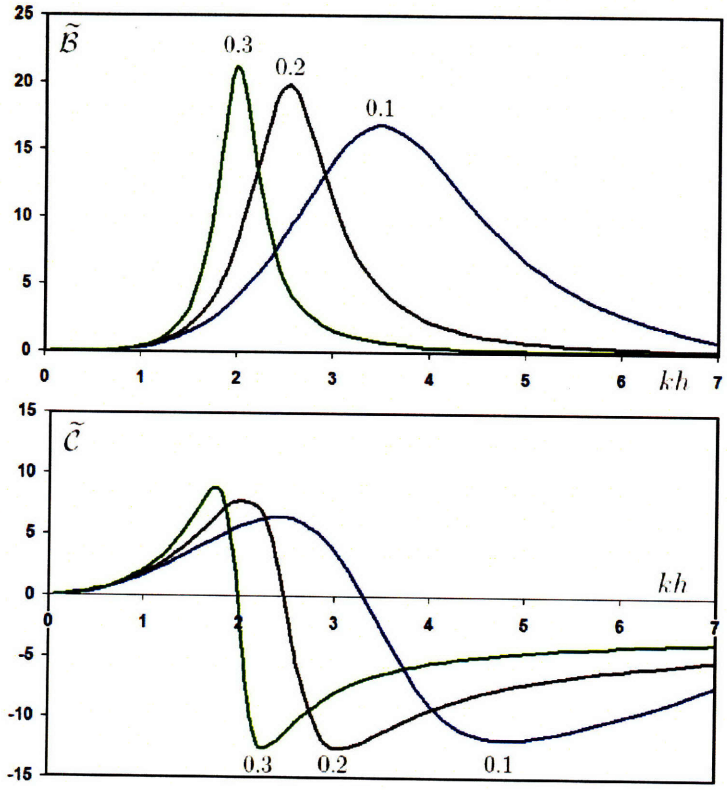

Figure 3-4: (i) Radiation damping and (ii) added mass against the normalized frequency kh for $d/h =$ 0.1 , 0.2 , 0.3. In all cases $a/h = 0.5$.

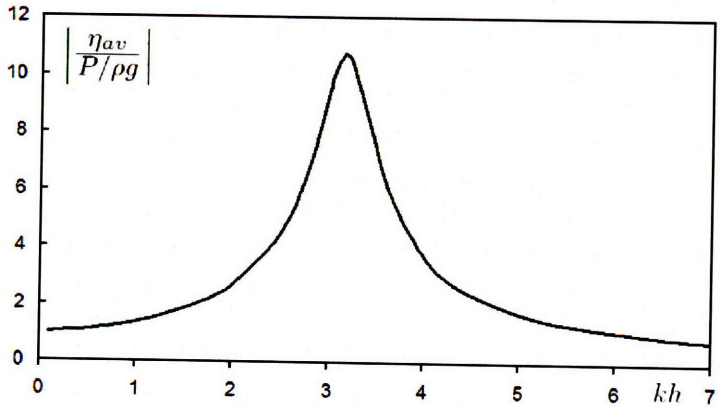

Figure 3-5: Amplitude of the free surface elevation average inside the cylinder against kh ; $a/h =$ 0.25 ; $d/h = 0.2$

towards 0. The peak corresponds to a piston like motion (or Helmholtz mode) as shown on the top of figure (3-6) by a 3D representation of the free surface elevation for a frequency slightly above resonance. Note in figure (3-5) that the small amplitude

assumption is violated if the forcing pressure is not small. This will be examined later when the OWC power output is computed.

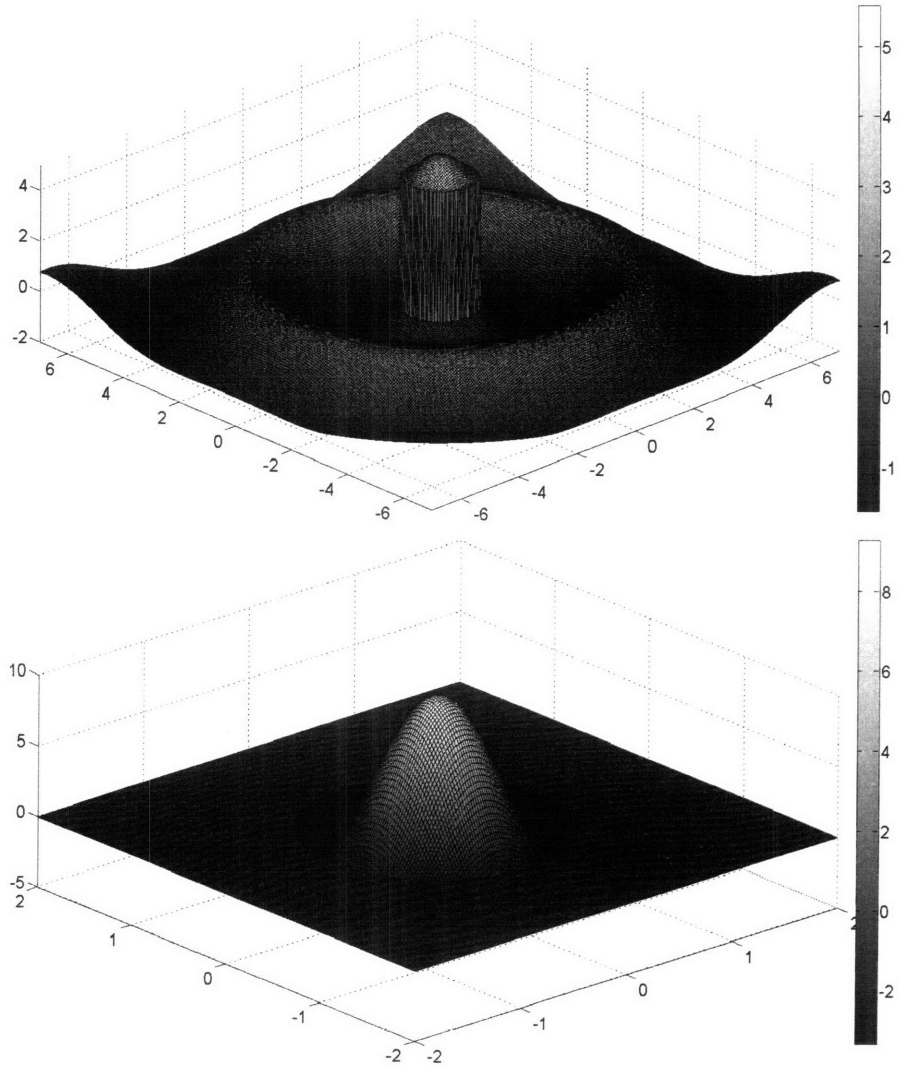

Figure 3-6: Free surface elevation inside and around the cylinder (i) close to the resonance frequency ; $kh = 2.55$; $t = \frac{3\pi}{2\omega}$ and (ii) close to the first axisymmetric natural mode ; $kh = 7.6388$; $t = 0$. In both cases: $a/h = 0.5$; $d/h = 0.2$.

It is also interesting to take a closer look at what happens near zeros of $J_0'(ka)$. It has been pointed out that at this frequency, a natural mode of oscillation develops inside the cylinder with no flux at $r = a$ from the propagating mode hence no dissipated power. As shown on the bottom of figure (3-6) for a frequency close to the first zero of $J_0'(ka)$, the local elevation amplitude at $r = 0$ increases drastically whereas

the outside of the cylinder is calm. The free surface inside the cylinder is dominated by $J_0(kr)$.

3.3 Diffraction Problem

3.3.1 Analysis

Let the incident wave arrive from the direction $\theta = \alpha$ with respect the breakwater (the x axis, see Figure 3-1). In the special case of head-sea incidence ($\alpha = \pi$), the breakwater has no effect. The diffraction problem is identical to that of a bottomless harbour treated by Garrett [17].

We first represent the total potential outside the cylinder as the sum of two parts:

$$\varphi_O(r,\theta,z) \;=\; \varphi_1 + \varphi_2 \tag{3.3.1}$$

Part φ_1 is due to scattering by a solid cylinder extending the entire sea depth and connected to the breakwater, and Part φ_2 is the correction for the opening. The first part is solved exactly in Appendix B by extending Stoker's treatment of a thin breakwater (the Sommerfeld problem [26]), with the following result :

$$\varphi_1 = \frac{-igA_o}{\omega}\sum_{n=0}^{\infty}\epsilon_n \frac{\cos\frac{n\alpha}{2}e^{-\frac{in\pi}{4}}iY'_{n/2}(ka)}{H'_{n/2}(ka)}\left(J_{n/2}(kr) - \frac{J'_{n/2}(ka)}{Y'_{n/2}(ka)}Y_{n/2}(kr)\right) \cdot \cos\left(\frac{n\theta}{2}\right)\frac{Z_0(z)}{Z_0(0)} \tag{3.3.2}$$

The second part φ_2 is due to the fluid pulsation at the opening $r = a$, $0 < \theta < 2\pi$, $-h < z < -d$ and is formally expressed as

$$\varphi_2 = \frac{-igA_o}{\omega}\sum_{\ell=0}^{\infty} Z_\ell(z)\sum_{n=0}^{\infty} A_{n\ell}\frac{K_{\frac{n}{2}}(\kappa_\ell r)}{\kappa_\ell a\; K'_{\frac{n}{2}}(\kappa_\ell a)}\cos\frac{n\theta}{2} \tag{3.3.3}$$

which satisfies the no-flux condition on both sides the breakwater ($\theta = 0,\ 2\pi$). Note that the terms with $\ell = 0$ corresponds to an outgoing wave

$$K_{\frac{n}{2}}(-ikr) = \frac{\pi}{2} i^{\frac{n}{2}+1} H^{(1)}_{\frac{n}{2}}(kr) \tag{3.3.4}$$

The coefficients $A_{n\ell}$ are yet unknown.

The potential inside the cylinder $r < a, 0 < \theta < 2\pi$ is due entirely to the opening,

$$\varphi_C = \frac{-igA_o}{\omega} \sum_{n=0}^{\infty} \sum_{\ell=0}^{\infty} \left(B_{n\ell} \cos n\theta + C_{n\ell} \sin n\theta\right) \frac{I_n(\kappa_\ell r)}{\kappa_\ell a\ I'_n(\kappa_\ell a)} Z_\ell(z) \tag{3.3.5}$$

where $B_{n\ell}$ and $C_{n\ell}$ are also unknown. Again for $\ell = 0$, $\kappa_0 = -ik$ and

$$I_{\frac{n}{2}}(-ikr) = (-i)^{\frac{n}{2}} J_{\frac{n}{2}}(kr) \tag{3.3.6}$$

Since φ_1 already satisfies the no flux condition on the cylindrical surface $r = a$ for the entire water depth, φ_2 must satisfy:

$$\frac{\partial \varphi_2}{\partial r} = \frac{\partial \varphi_C}{\partial r} = \begin{cases} 0 & -d < z < 0, \\ U(z,\theta) & -h < z < -d \end{cases} \tag{3.3.7}$$

which implies :

$$\begin{aligned} \sum_{n=0}^{\infty} \sum_{\ell=0}^{\infty} A_{n\ell} \cos\frac{n\theta}{2} Z_\ell(z) &= \sum_{n=0}^{\infty} \sum_{\ell=0}^{\infty} \left(B_{n\ell} \cos n\theta + C_{n\ell} \sin n\theta\right) Z_\ell(z) \\ &= \begin{cases} 0 & -d < z < 0, \\ \frac{ia\omega}{gA_o} U(z,\theta) & -h < z < -d \end{cases} \end{aligned} \tag{3.3.8}$$

Using orthogonality, we get for any integer ℓ and n:

$$\frac{2\pi}{\epsilon_n} A_{n,\ell} = \frac{ia\omega}{ghA_o} \int_0^{2\pi} \int_{-h}^{-d} U(\theta,z) Z_\ell(z) \cos\frac{n\theta}{2} d\theta dz \tag{3.3.9}$$

$$\frac{2\pi}{\epsilon_n} \{B_{n,\ell}\ ;\ C_{n,\ell}\} = \frac{ia\omega}{ghA_o} \int_0^{2\pi} \int_{-h}^{-d} U(\theta,z) Z_\ell(z) \{\cos(n\theta)\ ;\ \sin(n\theta)\} d\theta dz \tag{3.3.10}$$

Since the pressure must also be continuous at the opening, we require

$$\varphi_1 + \varphi_2 = \varphi_C, \qquad r = a, -h < z < -d \tag{3.3.11}$$

which implies in turn:

$$\begin{aligned}
&\textstyle\sum_{n=0}^{\infty} \epsilon_n \frac{\cos\frac{n\alpha}{2} e^{-\frac{in\pi}{4}} iY'_{n/2}(ka)}{H'_{n/2}(ka)} \left(J_{n/2}(ka) - \frac{J'_{n/2}(ka)}{Y'_{n/2}(ka)} Y_{n/2}(ka) \right) \cos\frac{n\theta}{2} \frac{Z_0(z)}{Z_0(0)} \\
&\qquad + \textstyle\sum_{n=0}^{\infty} \sum_{\ell=0}^{\infty} A_{n\ell} \frac{K_{\frac{n}{2}}(\kappa_\ell a)}{\kappa_\ell a \; K'_{\frac{n}{2}}(\kappa_\ell a)} \cos\frac{n\theta}{2} Z_\ell(z) \\
&\quad = \textstyle\sum_{n=0}^{\infty} \sum_{\ell=0}^{\infty} \left(B_{n\ell} \cos n\theta + C_{n\ell} \sin n\theta \right) \frac{I_n(\kappa_\ell a)}{\kappa_\ell a \; I'_n(\kappa_\ell a)} Z_\ell(z)
\end{aligned} \tag{3.3.12}$$

Let us denote for brevity:

$$\mathcal{E}_n = \epsilon_n \frac{\cos\frac{n\alpha}{2} e^{-\frac{in\pi}{4}} iY'_{n/2}(ka)}{Z_0(0) H'_{n/2}(ka)} \left(J_{n/2}(ka) - \frac{J'_{n/2}(ka)}{Y'_{n/2}(ka)} Y_{n/2}(ka) \right) \tag{3.3.13}$$

hence

$$\begin{aligned}
&\sum_{n=0}^{\infty} \left[\mathcal{E}_n \cos\frac{n\theta}{2} Z_0(z) + \sum_{\ell=0}^{\infty} A_{n\ell} \frac{K_{\frac{n}{2}}(\kappa_\ell a)}{\kappa_\ell a \; K'_{\frac{n}{2}}(\kappa_\ell a)} \cos\frac{n\theta}{2} Z_\ell(z) \right] \\
&\qquad = \sum_{n=0}^{\infty} \sum_{\ell=0}^{\infty} \left(B_{n\ell} \cos n\theta + C_{n\ell} \sin n\theta \right) \frac{I_n(\kappa_\ell a)}{\kappa_\ell a \; I'_n(\kappa_\ell a)} Z_\ell(z)
\end{aligned} \tag{3.3.14}$$

After using (3.3.9, 3.3.10), we get

$$\begin{aligned}
&\tfrac{-2\pi i g A_o}{a\omega} \textstyle\sum_{n=0}^{\infty} \mathcal{E}_n \cos\frac{n\theta}{2} Z_0(z) + \\
&\textstyle\sum_n \sum_{\ell=0}^{\infty} \frac{\epsilon_n}{h} \int_0^{2\pi} \int_{-h}^{-d} U(\theta', z') Z_\ell(z') \cos(\frac{n\theta'}{2}) d\theta' dz' \frac{K_{\frac{n}{2}}(\kappa_\ell a)}{\kappa_\ell a \; K'_{\frac{n}{2}}(\kappa_\ell a)} \cos(\frac{n\theta}{2}) Z_\ell(z) \\
&= \textstyle\sum_{n=0}^{\infty} \sum_{\ell=0}^{\infty} \frac{\epsilon_n}{h} \int_0^{2\pi} \int_{-h}^{-d} U(\theta', z') Z_\ell(z') \cos(n\theta') d\theta' dz' \cos(n\theta) \frac{I_n(\kappa_\ell a)}{\kappa_\ell a \; I'_n(\kappa_\ell a)} Z_\ell(z) \\
&+ \textstyle\sum_{n=0}^{\infty} \sum_{\ell=0}^{\infty} \frac{\epsilon_n}{h} \int_{-h}^{-d} U(\theta', z') Z_\ell(z') \sin(n\theta') d\theta' dz' \sin(n\theta) \frac{I_n(\kappa_\ell a)}{\kappa_\ell a \; I'_n(\kappa_\ell a)} Z_\ell(z)
\end{aligned} \tag{3.3.15}$$

which is an integral equation for $U(\theta, z)$

$$\iint d\theta' dz' U(z', \theta') \mathcal{K}(z, \theta; z', z', \theta') = \frac{-2\pi i g A_o}{a\omega} \sum_{n=0}^{\infty} \mathcal{E}_n \cos\frac{n\theta}{2} Z_0(z),$$
$$0 < \theta < 2\pi, , \quad -h < z < -d \tag{3.3.16}$$

with the kernel:

$$\begin{aligned}
&\mathcal{K}(z, \theta; z', \theta') \equiv \\
&\quad \sum_{n=0}^{\infty}\sum_{\ell=0}^{\infty} \frac{\epsilon_n}{h} \frac{I_n(\kappa_\ell a)}{\kappa_\ell a \; I_n'(\kappa_\ell a)} Z_\ell(z) Z_\ell(z') \left[\sin(n\theta)\sin(n\theta') + \cos(n\theta)\cos(n\theta')\right] \\
&- \sum_{n=0}^{\infty}\sum_{\ell=0}^{\infty} \frac{\epsilon_n}{h} \frac{K_{\frac{n}{2}}(\kappa_\ell a)}{\kappa_\ell a \; K_{\frac{n}{2}}'(\kappa_\ell a)} Z_\ell(z) Z_\ell(z') \cos(\frac{n\theta}{2}) \cos(\frac{n\theta'}{2})
\end{aligned} \tag{3.3.17}$$

Again we let $U(\theta, z)$ be expanded as a series of orthogonal functions,

$$U(\theta, z) = \frac{-igA_o}{\omega} \sum_{m=0}^{\infty}\sum_{p=0}^{\infty} \left(\alpha_{mp} \cos m\theta + \beta_{mp} \sin m\theta\right) u_p(z) \tag{3.3.18}$$

We first rewrite the integral equation (3.3.15) as:

$$\begin{aligned}
&\sum_{n=0}^{\infty} 2\pi \frac{h}{a} \mathcal{E}_n \cos\frac{n\theta}{2} Z_0(z) = \\
&\quad - \sum_{n=0}^{\infty}\sum_{\ell=0}^{\infty}\sum_{m=0}^{\infty}\sum_{p=0}^{\infty} \epsilon_n \beta_{mp} F_{p\ell} \frac{4m(1-(-1)^n)}{4m^2 - n^2} \frac{K_{\frac{n}{2}}(\kappa_\ell a)}{\kappa_\ell a \; K_{\frac{n}{2}}'(\kappa_\ell a)} \cos\frac{n\theta}{2} Z_\ell(z) \\
&\quad - \sum_{n=0}^{\infty}\sum_{\ell=0}^{\infty}\sum_{m=0}^{\infty}\sum_{p=0}^{\infty} 2\pi \alpha_{mp} F_{p\ell} \delta_{\frac{n}{2}m} \frac{K_{\frac{n}{2}}(\kappa_\ell a)}{\kappa_\ell a \; K_{\frac{n}{2}}'(\kappa_\ell a)} \cos\frac{n\theta}{2} Z_\ell(z) \\
&\quad + \sum_{n=0}^{\infty}\sum_{\ell=0}^{\infty}\sum_{m=0}^{\infty}\sum_{p=0}^{\infty} 2\pi \beta_{mp} F_{p\ell} \delta_{nm} \left(1 - \delta_{n0}\right) \frac{I_n(\kappa_\ell a)}{\kappa_\ell a \; I_n'(\kappa_\ell a)} \sin n\theta Z_\ell(z) \\
&\quad + \sum_{n=0}^{\infty}\sum_{\ell=0}^{\infty}\sum_{m=0}^{\infty}\sum_{p=0}^{\infty} 2\pi \alpha_{mp} F_{p\ell} \delta_{nm} \frac{I_n(\kappa_\ell a)}{\kappa_\ell a \; I_n'(\kappa_\ell a)} \cos n\theta Z_\ell(z)
\end{aligned} \tag{3.3.19}$$

After using (3.2.14), multiplying (3.3.16) by $u_P(z)\cos M\theta$ and $u_P(z)\sin M\theta$ in turn, and integrating over the range $0<\theta<2\pi, -h<z-d$, we get for any P and M:

$$\mathcal{E}_{2M}F_{P0}\frac{h}{a}=\sum_{\ell=0}^{\infty}\sum_{p=0}^{\infty}\alpha_{Mp}\left[\frac{I_M(\kappa_\ell a)}{\kappa_\ell a\ I'_M(\kappa_\ell a)}-\frac{K_M(\kappa_\ell a)}{\kappa_\ell a\ K'_M(\kappa_\ell a)}\right]F_{p\ell}F_{P\ell} \tag{3.3.20}$$

and

$$\begin{aligned}\sum_{n=0}^{\infty}2\pi\frac{h}{a}\mathcal{E}_nF_{P0}\frac{4M(1-(-1)^n)}{4M^2-n^2}&=\sum_{\ell=0}^{\infty}\sum_{p=0}^{\infty}2\pi^2\beta_{Mp}\frac{I_M(\kappa_\ell a)}{\kappa_\ell a\ I'_M(\kappa_\ell a)}F_{p\ell}F_{P\ell}\\ -\sum_{n=0}^{\infty}\sum_{\ell=0}^{\infty}\sum_{m=0}^{\infty}\sum_{p=0}^{\infty}\epsilon_n\beta_{mp}&\frac{K_{\frac{n}{2}}(\kappa_\ell a)}{\kappa_\ell a\ K'_{\frac{n}{2}}(\kappa_\ell a)}F_{p\ell}F_{P\ell}\frac{16mM(1-(-1)^n)^2}{(4m^2-n^2)(4M^2-n^2)}\end{aligned} \tag{3.3.21}$$

Thus α_{mp} and β_{mp} are governed by separate algebraic equations. After solving them numerically, all the coefficients $A_{n\ell}$, $B_{n\ell}$ and $C_{n\ell}$ can be related to the flux and computed using (3.3.9, 3.3.10). Then the diffraction potential in the entire fluid is found.

3.3.2 Independence of Γ in Incidence Angle

For computing the power output we need the complex amplitude of the total vertical flux across the chamber surface S_c:

$$\begin{aligned}\Gamma &= \frac{1}{A_o}\iint_{S_c}\frac{\partial\varphi_C}{\partial z}dS\\ &= \frac{-ig}{\omega}\iint_{S_c}\sum_{n=0}^{\infty}\sum_{\ell=0}^{\infty}(B_{n\ell}\cos n\theta+C_{n\ell}\sin n\theta)\frac{I_n(\kappa_\ell r)}{\kappa_\ell a\ I'_n(\kappa_\ell a)}Z'_\ell(0)rd\theta dr\\ &= \frac{-2\pi ig}{\omega}\int_0^a\sum_{\ell=0}^{\infty}B_{0\ell}\frac{I_n(\kappa_\ell r)}{\kappa_\ell a\ I'_n(\kappa_\ell a)}Z'_\ell(0)rdr\end{aligned} \tag{3.3.22}$$

which only depends on the coefficients $B_{0\ell}$. From (3.3.10), and the decomposition of $U(\theta, z)$ by (3.3.18), we get

$$\begin{aligned} B_{0,\ell} &= \frac{ia\omega}{2\pi g h A_o} \int_0^{2\pi} \int_{-h}^{-d} U(\theta, z) Z_\ell(z) d\theta dz \\ &= \frac{a}{2\pi h} \int_0^{2\pi} \int_{-h}^{-d} Z_\ell(z) \sum_{m=0}^{\infty} \sum_{p=0}^{\infty} \left(\alpha_{mp} \cos m\theta + \beta_{mp} \sin m\theta\right) u_p(z) d\theta dz \\ &= \frac{a}{h} \int_{-h}^{-d} Z_\ell(z) \sum_{p=0}^{\infty} \alpha_{0p} u_p(z) dz \end{aligned} \tag{3.3.23}$$

Recall from (3.3.20) that α_{0p}, $p = 0, 1, 2, ...$, are governed by the algebraic system

$$\frac{h}{a} \mathcal{E}_0 J_{2P}(\kappa_0(h-d)) N_0^{-1/2} = \sum_{\ell=0}^{\infty} \sum_{p=0}^{\infty} \alpha_{0p} \left[\frac{I_0(\kappa_\ell a)}{\kappa_\ell a \; I_0'(\kappa_\ell a)} - \frac{K_0(\kappa_\ell a)}{\kappa_\ell a \; K_0'(\kappa_\ell a)} \right] F_{p\ell} F_{P\ell} \tag{3.3.24}$$

Since by definition

$$\mathcal{E}_0 = \frac{i Y_0'(ka)}{Z_0(0) H_0'(ka)} \left(J_0(ka) - \frac{J_0'(ka)}{Y_0'(ka)} Y_0(ka) \right)$$

this algebraic linear system (3.3.24) is independent of the incidence angle α. Thus, all α_{0p} coefficients and consequently Γ are also independent of α. Since the radiation problem is axially symmetric, coefficients $\mathcal{B}$ and $\mathcal{C}$ are independent of α. It follows that the power output is the same as if the breakwater is absent and the OWC unit is in the open sea. The existence of the breakwater affects only the waves pattern, the local free surface elevation, the wave forces, etc ; but not the averaged quantities inside the OWC.

This remarkable result must be the combined consequence of the idealized geometry of circular column, thin breakwater and a 360° as well as the approximation of uniform air pressure inside the column.

3.3.3 Computational Aspects

In numerical computations all series are truncated after a large but finite number of terms. For example (3.3.18) is approximated by

$$U(\theta, z) = \sum_{n=0}^{N_t} \sum_{p=0}^{N_c} (\alpha_{np} \cos n\theta + \beta_{np} \sin n\theta)\, u_p(z)$$

Table (3.2) shows how some of the computed parameters evolve in a random case as the number of terms N_c in the series of Chebychev polynomials increases. It can be observed that the convergence is very fast and it is important to note that a very good level of accuracy can be obtained with very few terms (for the following calculation, we use $N_c = 5$ which a good compromise between accuracy and computing load).

N_c	η_{av}	$\lvert B_{00}\rvert$	$\lvert B_{01}\rvert$	$\lvert B_{10}\rvert$	$\lvert B_{20}\rvert$	$\lvert C_{10}\rvert$	$\lvert C_{11}\rvert$
1	0.3330	0.0039792	0.0049128	0	0.0063948	0.0342504	0.0422866
2	3.1689	0.0680241	0.0035775	0	0.0067494	0.0407022	0.0201958
3	4.6283	0.1042643	0.0055707	0	0.0069427	0.0407318	0.0198914
4	4.7553	0.1074447	0.0056937	0	0.0069744	0.0407479	0.0198955
5	4.7598	0.1075570	0.0056982	0	0.0069758	0.0407475	0.0198959
6	4.7599	0.1075580	0.0056982	0	0.0069758	0.0407478	0.0198958
7	4.7599	0.1075581	0.0056982	0	0.0069758	0.0407479	0.0198958

Table 3.2: Convergence of different coefficients as N_c increases. Case $\alpha = \pi/2$, $a/h = 0.1$, $d/h = 0.2$, $ka = 0.42$, $N_t = 5$ and $N_\ell = 2000$.

Table (3.3) shows how the slow convergence with the number of terms N_t in the angular cosine/sine expansion. Note that each increase of N_t causes a very significant increase in computation time. However, it must be also be noted that this affects only the C_{nm} coefficients and not the B_{nm} or any average quantity like the inside free surface elevation.

It is also necessary to examine how the convergence depends on the number of

N_t	η_{av}	$\lvert B_{00}\rvert$	$\lvert C_{10}\rvert$	$\lvert C_{20}\rvert$	$\lvert C_{21}\rvert$	$\lvert C_{31}\rvert$
16	4.7553	0.107445	0.039527	0.023211	0.012338	0.009766
22	4.7553	0.107445	0.039379	0.022882	0.012097	0.009450
30	4.7553	0.107445	0.039273	0.022646	0.011926	0.009226
38	4.7553	0.107445	0.039211	0.022509	0.011827	0.009096
40	4.7553	0.107445	0.039200	0.022483	0.011809	0.009071
42	4.7553	0.107445	0.039189	0.022460	0.011792	0.009049
44	4.7553	0.107445	0.039179	0.022438	0.011777	0.009029
46	4.7553	0.107445	0.039171	0.022419	0.011763	0.009010
48	4.7553	0.107445	0.039162	0.022401	0.011750	0.008994
49	4.7553	0.107445	0.039159	0.022392	0.011744	0.008986
50	4.7553	0.107445	0.039155	0.022384	0.011738	0.008978

Table 3.3: Convergence of different coefficients as N_t increases. Case $\alpha = \pi/2$, $a/h = 0.1$, $d/h = 0.2$, $ka = 0.42$, $N_\ell = 2000$ and $N_c = 4$.

vertical modes $Z_\ell(z)$. Let us recall (3.3.5),

$$\varphi_C = \frac{-igA_o}{\omega} \sum_{n=0}^{N_t} \sum_{\ell=0}^{N_\ell} (B_{n\ell} \cos n\theta + C_{n\ell} \sin n\theta) \frac{I_n(\kappa_\ell r)}{\kappa_\ell a \; I'_n(\kappa_\ell a)} Z_\ell(z)$$

Table (3.4) shows that an extremely large number of terms is needed to get to a good level of accuracy. This is explained by the fact that the $Z_\ell(z)$ functions are continuous whereas the potential is singular at the edge of the cylinder. However, the computation time increases slowly with N_ℓ. Thus, it is not a problem to use several thousand terms in the series and get a very good convergence. For the presented results, we use $N_\ell = 2000$.

N_ℓ	η_{av}	$\lvert B_{00}\rvert$	$\lvert B_{01}\rvert$	$\lvert B_{10}\rvert$	$\lvert B_{20}\rvert$	$\lvert C_{10}\rvert$	$\lvert C_{11}\rvert$
1000	4.7695	0.1077759	0.0057072	0	0.0069775	0.0407654	0.0198934
1500	4.7600	0.1075549	0.0056982	0	0.0069755	0.0407537	0.0198948
2000	4.7553	0.1074447	0.0056937	0	0.0069744	0.0407479	0.0198955
2010	4.7552	0.1074431	0.0056937	0	0.0069744	0.0407478	0.0198955
2020	4.7552	0.1074415	0.0056936	0	0.0069744	0.0407477	0.0198955

Table 3.4: Convergence of different coefficients as N_ℓ increases. Case $\alpha = \pi/2$, $a/h = 0.1$, $d/h = 0.2$, $ka = 0.42$, $N_t = 5$ and $N_c = 4$.

This overview shows that all truncated series converge and that any desired accuracy can be achieved if the number of terms in the truncated series is increased. This proves that the model is very flexible and allows the user to decide on the trade-off between precision and computation time.

3.3.4 Numerical Results

Validation using reciprocal relation

It has been shown by Evans [11] that for an OWC, the radiation damping coefficient B can be related to the vertical flux in the column due to diffraction by

$$B = \frac{k}{8\pi\rho g a_o^2 C_g} \int_0^{2\pi} |\widehat{Q}^D(\alpha)|^2 d\alpha \tag{3.3.25}$$

which is similar to the Haskind-Hanoka relation for oscillating bodies.
Because $\widehat{Q}^D$ is independent of α, the above identity reduces to (Appendix D),

$$B = \frac{k\left|\widehat{Q}^D\right|^2}{4\rho g a_o^2 C_g} \qquad \text{i.e.} \qquad \widetilde{B} = \frac{kag\left|\widetilde{\Gamma}\right|^2}{4C_g\omega} \tag{3.3.26}$$

This relation has been used to confirm the accuracy of separate computations of radiation and diffraction potentials - table (3.5). Note that a direct consequence is that if only the extracted power is required, there is no need to solve for the scattering problem since $|\Gamma|$ can be deduced directly from the radiation damping $\mathcal{B}$.

ka	0.089	0.276	0.359	0.387	0.420	0.522	0.617
$\widetilde{\mathcal{B}}$	0.0015975	0.24867	3.4735	28.5656	8.2351	0.40801	0.13098
$\frac{kag\left\|\widetilde{\Gamma}\right\|^2}{4C_g\omega}$	0.0015975	0.24867	3.4736	28.5666	8.2348	0.40800	0.13098

Table 3.5: Radiation damping $\widetilde{\mathcal{B}}$ obtained by computation both sides of equation (3.3.26) for different values of ka. $a/h = 0.1$; $d/h = 0.2$.

Validation for limiting cases

For the diffraction problem we shall present results for the normalized free surface displacement in and near the oscillating water column,

$$\frac{\eta}{A_0} = \frac{i\omega\,\varphi|_{z=0}}{gA_0} \tag{3.3.27}$$

where A_0 is the incident wave amplitude. Since the air pressure above the water surface inside the column is assumed to be uniform, the spatial average of the free-surface height inside the column is important; its amplitude is denoted by:

$$\eta_{av} = \left| \iint_S \frac{\eta}{A_0} dS \right| \tag{3.3.28}$$

In some limiting cases, our results can be compared to known solutions. As d/h tends to 1, it is expected that the solution tends to that of an infinite cylinder at the edge of a breakwater. The left side of Figure (3-7) compares the polar representations of the free surface elevation for two values of d/h and the limiting case - analytical expression from theory in Appendix B. Indeed, agreement is clear.
A second possible test is to decrease ka and check that the solution tends towards that of a breakwater with no cylinder which is known exactly as well. Good agreement is shown on the right side of Figure (3-7).

Validation by comparing with the bottomless harbour

We can compare our results with Garrett's study of Bottomless Harbours [17] since a head-sea incidence in our model ($\alpha = \pi$) is equivalent to the case of a isolated truncated cylinder in open sea. In Garrett's notations,

$$\begin{aligned} \frac{\eta}{A_0} = \quad & \sum_n \Bigg[\epsilon_n (A_n^B \cos(n\theta) + A_n^C \sin(n\theta)) J_n(kr) + \\ & \sum_\ell{}' (B_{n\ell} \cos n\theta + C_{n\ell} \sin n\theta) \frac{I_n(\kappa_\ell r)}{\kappa_\ell I_n'(\kappa_\ell a)} Z_\ell(0) \Bigg] \end{aligned} \tag{3.3.29}$$

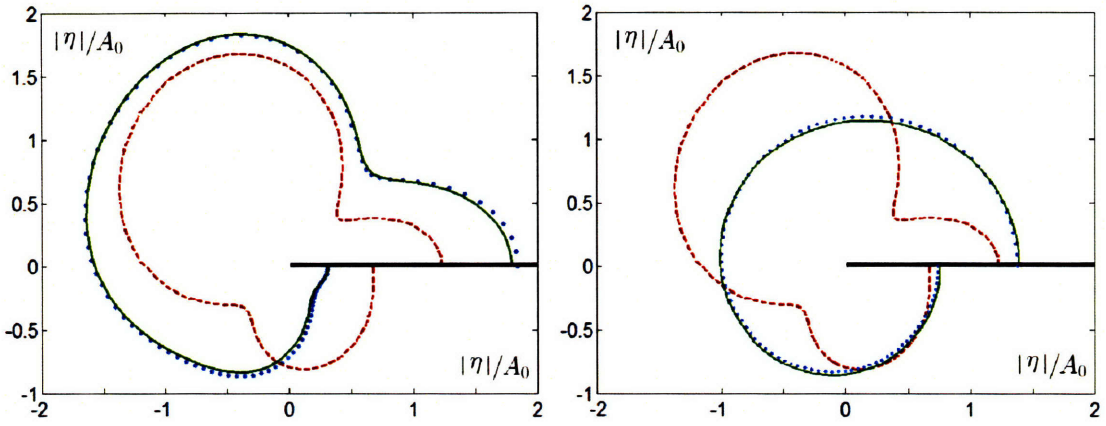

Figure 3-7: Polar plot of the free surface elevation along the wall ($r = a$) outside the chamber. **Left:** Convergence towards the theoretical solution for a cylinder extending to the bottom (dots) as d/h increases ($d/h = 0.5$: dashed ; $d/h = 0.99$: plain). $ka = 1.3$. **Right:** Convergence towards the theoretical solution for a breakwater with no cylinder (dots) as ka decreases ($ka = 1.3$: dashed ; $ka = 0.32$: plain). $d/h = 0.5$. For all cases $a/h = 1$ and $\alpha = 2\pi/3$.

where $\sum'_\ell = \sum_{\ell=1}^{\infty}$. Let us recall that inside the column (3.3.5):

$$\frac{\eta}{A_0} = \sum_n \sum_\ell' \left(B_{n\ell} \cos n\theta + C_{n\ell} \sin n\theta\right) \frac{I_n(\kappa_\ell r)}{\kappa_\ell a \; I'_n(\kappa_\ell a)} Z_\ell(0)$$

This means,

$$A_n^B = \frac{B_{n0}}{\epsilon_n ka \; J'_n(ka) Z_0(0)} \quad ; \quad A_n^C = \frac{C_{n0}}{\epsilon_n ka \; J'_n(ka) Z_0(0)} \tag{3.3.30}$$

The $\left|A_n^{B/C}\right|$'s can be interpreted as the amplitudes of the different modes. Note that for head-sea incidence ($\alpha = \pi$, corresponding to the bottomless harbour), $A_n^C = 0$ for all n by symmetry and A_n^B is the same as A_n in Garrett. Figure (3-8 - left side) is a graph comparing, for a particular case, Garrett's A_1^B coefficient and our computations. The agreement is very good.

Let us now examine the variation of the A_n^B coefficient as the frequency ka varies in order to develop a more physical interpretation of these coefficients. The right side of Figure (3-8) shows the variation of the first three A_n^B coefficients versus the wave

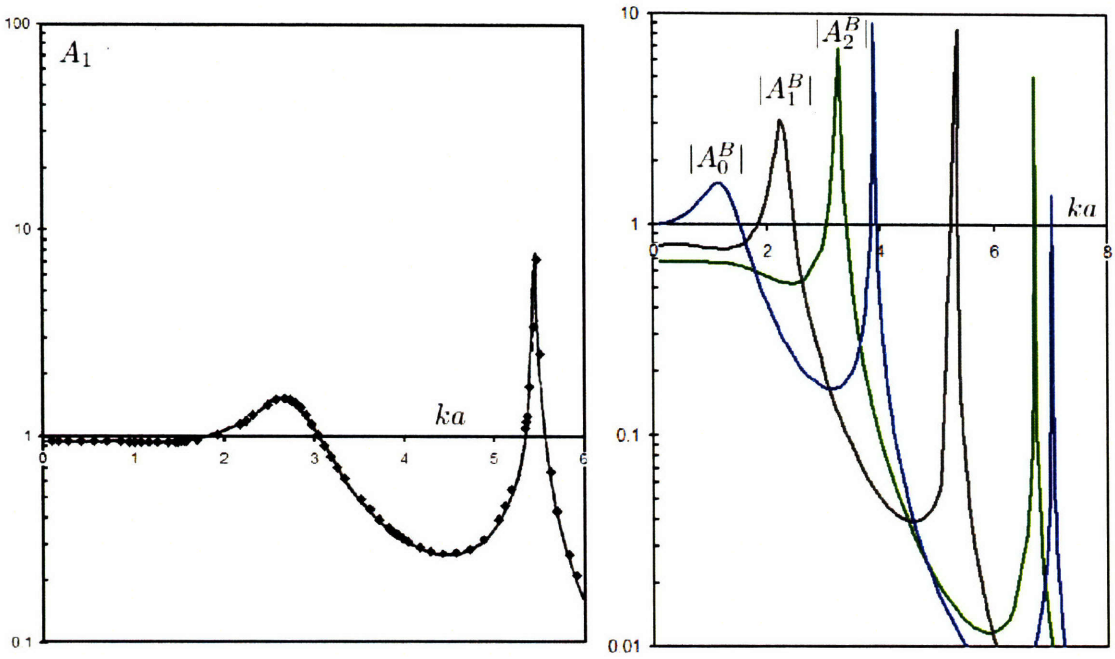

Figure 3-8: (i) A_1 as defined by Garrett against ka for $\alpha = \pi$, $h/a = 0.6$ and $d/a = 0.2$ - Garret's results (solid curve) and numerical computation (diamonds, A_1^B). (ii) $|A_0^B|$, $|A_1^B|$ and $|A_2^B|$ against ka computed for $h/a = 0.6$, $d/a = 0.4$, $\alpha = \pi$.

frequency. These results are again in very good agreement with Garrett's study. We observe the first resonance at the small value of $ka = 1.16$ where A_0^B dominates. The radial dependence is dominated by $J_0(kr)$ which is of one sign for all $0 < r < a$ since the first zero of $J_0(kr)$ is at $kr = 2.4$. This mode can be regarded as the Helmholtz mode.

As ka increases, sharp resonance peaks appear where only one single mode is dominant. These peaks ($ka = 2.24, 3.26, 3.88, 5.35, 6.75, 7.03...$) happen around each zero of J_n' ($J_n'(ka) = 0$; $ka = 1.84, 3.05, 3.83, 5.33, 6.71, 7.02...$)as discussed in [17].

Let us examine the free surface inside and around the cylinder at these resonance points, at $t = 0$ (still for head-sea incidence). Recall that $A_n^{B/C}$'s are the amplitudes of the propagating modes. We shall investigate if they are actually a good representation of the oscillation modes. Figure (3-9.(i)) corresponds to the first resonance where A_0^B dominates and gives an almost uniform surface inside the cylinder (Helmholtz mode). Then, as we go through the resonances of A_1^B and A_2^B, patterns of variation in $\cos(\theta)$

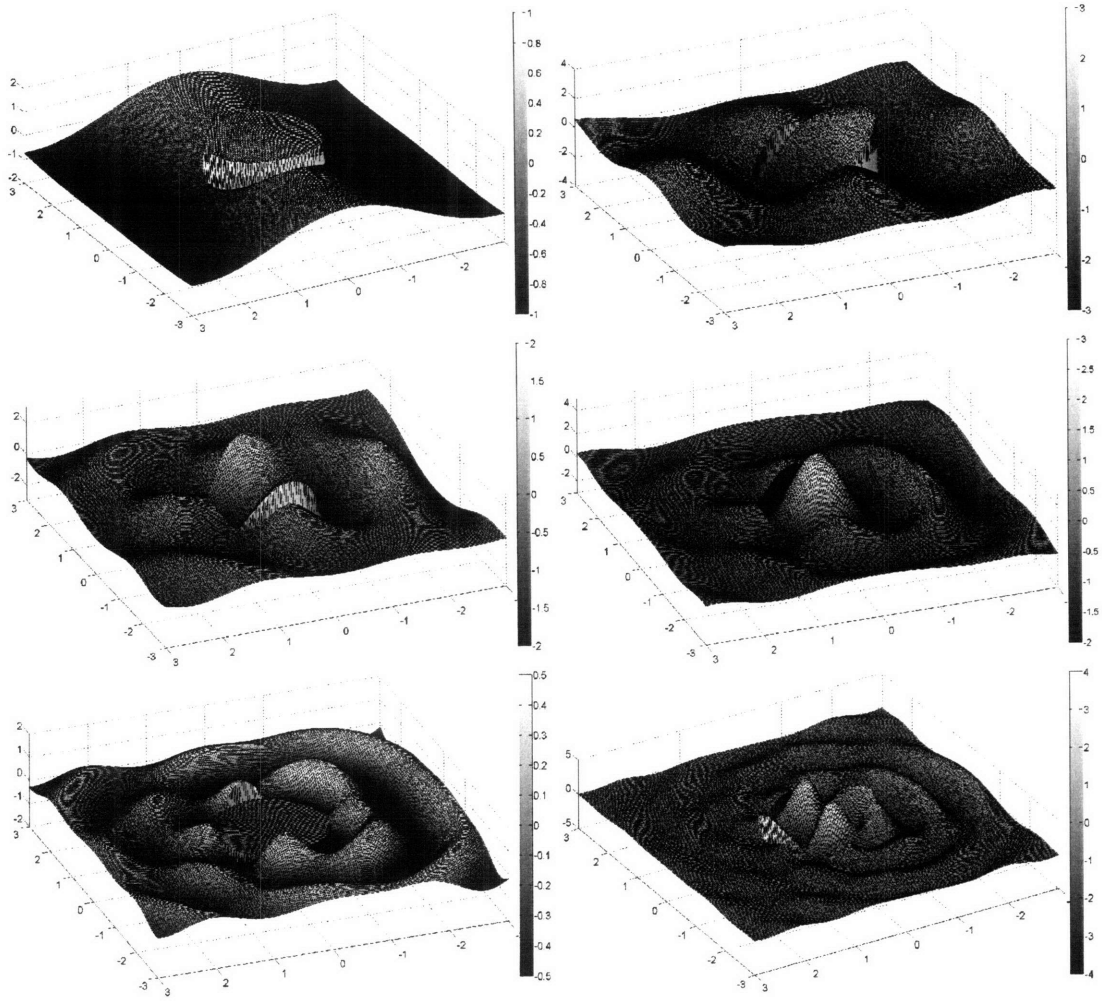

Figure 3-9: Free surface elevation inside and around the cylinder for different resonance modes - isolated cylinder with the incident wave coming from the right of the figures ; $h/a = 0.6$; $d/a = 0.4$; $t = 0$. From top left to bottom , as ka increases: (i) First mode in $\cos(0.\theta)$ ($ka = 1.16$) ; (ii) First mode in $\cos(\theta)$ ($ka = 2.24$) ; (iii) First mode in $\cos(2\theta)$ ($ka = 3.18$) ; (iv) Second mode in $\cos(0\theta)$ ($ka = 3.87$) ; (v) No resonance ($ka = 4.57$) ; (vi) Second mode in $\cos(2\theta)$ ($ka = 6.71$)

(ii) and $\cos(2\theta)$ (iii) can be identified. If ka increases further, we observe a more complex geometry of surface where the angular variation is coupled with the radial variation of Bessel functions. Figure (3-9.(iv)) shows the $J_0(kr)$ variation and (vi) the $J_2(kr)cos(2\theta)$ variation, corresponding respectively to the second peaks of A_0^B and A_2^B. Figure (3-9.(v)) represents the situation where there is no resonance. Thus the maxima of A_n^B's are indicators of resonance of a particular mode of oscillation.

Oblique incidences

Sample numerical results are displayed in Figure 3-10 for the free surface in and outside the cylinder at the first resonance peak. In this figure, the geometry is chosen to be typical for a realistic OWC design with $a/h = 0.5$ and $d/h = 0.2$. Note that the free surface inside is roughly uniform and relatively insensitive to the angle of incidence, only tilting slightly in the direction of the incident wave. On the other hand, the free surface outside varies considerably with α and seems largely dominated by the plain wave. The presence of the breakwater is made obvious by the discontinuity along the axis $x = 0$.

The free surface amplitude along the outside wall of the cylinder is shown in Figure (3-11) for $ka \approx 1$ and in Figure (3-12) for $ka = 3$. This information can be useful for computing wave forces on the structure. Generally, the elevation at the angle $\theta = 0$ along the breakwater is significantly larger than that on an isolated cylinder. On the shadow side the elevation is considerably reduced as expected. For comparison, the plots show both the profiles for an open cylinder and one extending to the bottom. Interestingly, at a lower frequency ($ka \approx 1$), the difference between the two cases is very significant, thus showing an interaction with the inside of the cylinder. On the other hand, at a larger frequency $ka = 3$, both cases are very close. This suggests that higher frequency waves do not penetrate the opening.

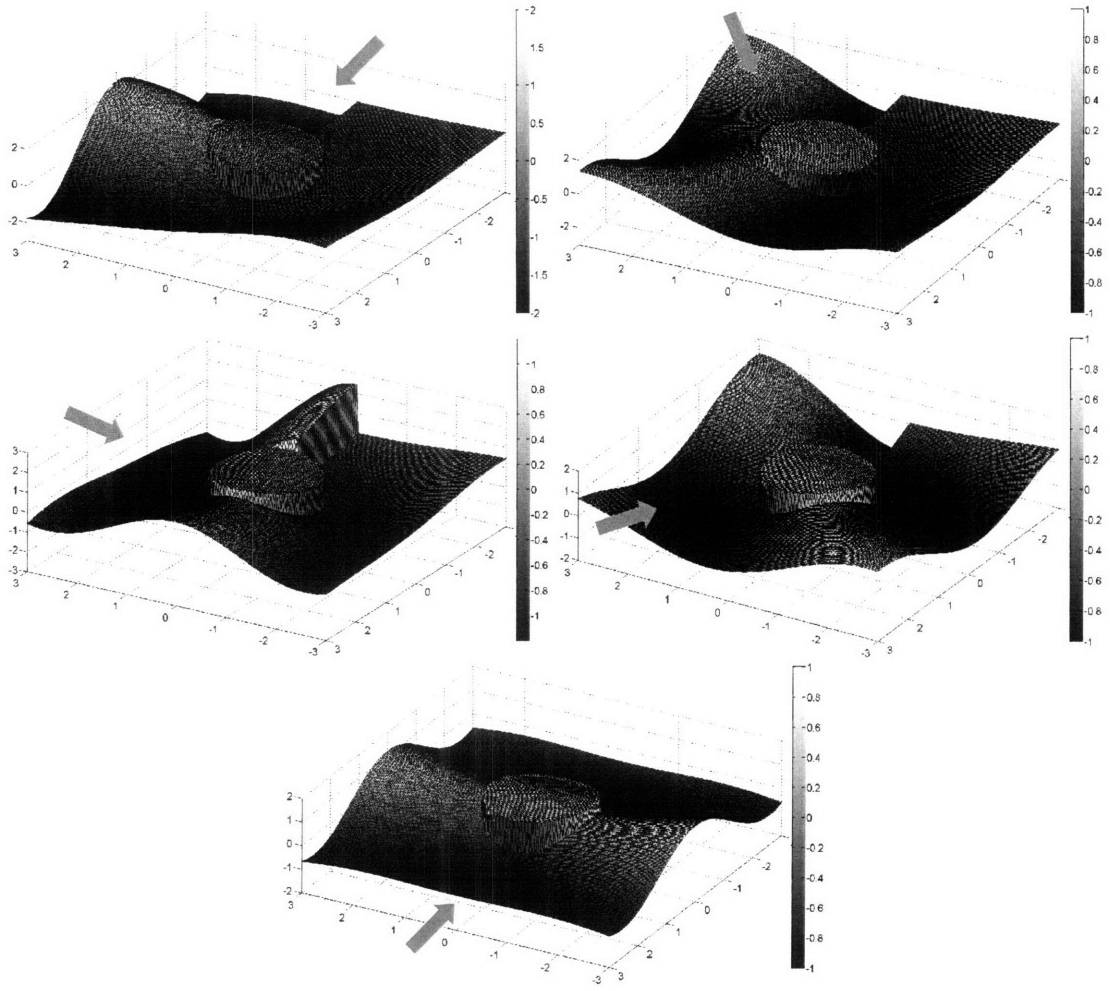

Figure 3-10: Free surface elevation inside and around the cylinder for different incidence angles at resonance of the 0^{th} mode - $a/h = 0.5$; $d/h = 0.2$; $ka = 1.27$; $t = 0$. From top left to bottom , as α increases: (i) Tail-sea incidence $\alpha = 0$; (ii) Oblique incidence $\alpha = \pi/4$; (iii) Normal incidence $\alpha = \pi/2$; (iv) Oblique incidence $\alpha = 3\pi/4$; (v) Head-sea incidence $\alpha = \pi$.

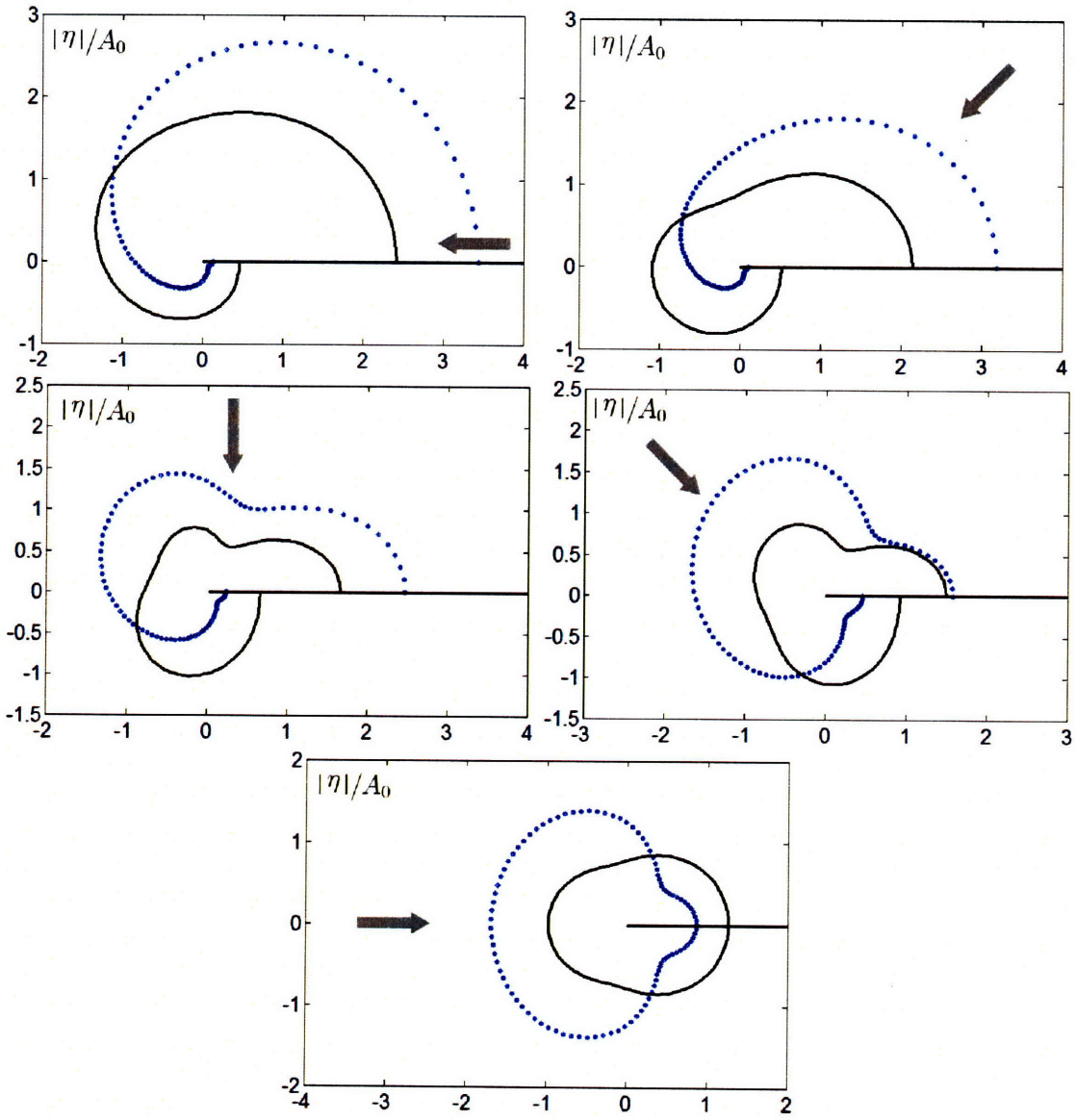

Figure 3-11: Polar plot of the free surface elevation amplitude along the outside wall of the cylinder - $r = a$ - for different incidence angles - $a/h = 0.5$; $ka = 1.12$. Dots: cylinder extending to the bottom ; Solid line: truncated empty cylinder with $d/h = 0.2$. From top left to bottom , as α increases: (i) Tail-sea incidence $\alpha = 0$; (ii) Oblique incidence $\alpha = \pi/4$; (iii) Normal incidence $\alpha = \pi/2$; (iv) Oblique incidence $\alpha = 3\pi/4$; (v) Head-sea incidence $\alpha = \pi$.

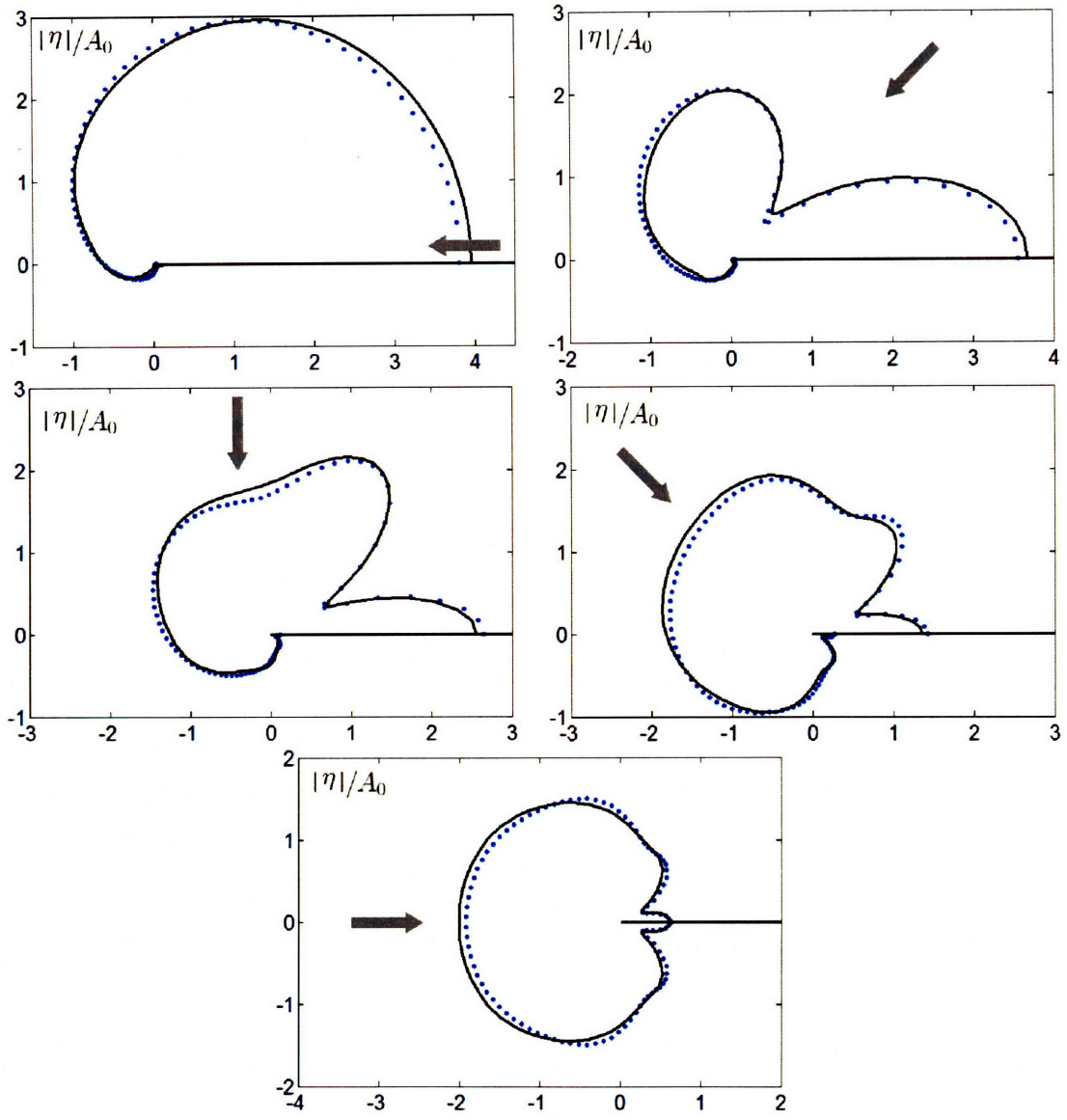

Figure 3-12: Polar plot of the free surface elevation amplitude along the outside wall of the cylinder - $r = a$ - for different incidence angles - $a/h = 0.5$; $ka = 3$. Dots: cylinder extending to the bottom ; Red line: truncated empty cylinder with $d/h = 0.2$. From top left to bottom , as α increases: (i) Tail-sea incidence $\alpha = 0$; (ii) Oblique incidence $\alpha = \pi/4$; (iii) Normal incidence $\alpha = \pi/2$; (iv) Oblique incidence $\alpha = 3\pi/4$; (v) Head-sea incidence $\alpha = \pi$.

In summary, the main result here is that the amplitude of the hydrodynamic coefficient Γ and thus the power output are independent of the incident angle of the incoming wave for this configuration. However, the breakwater affects significantly the wave pattern outside the cylinder.

3.4 Extracted Power

3.4.1 Numerical Results

Different configurations have been investigated in order to evaluate the influence of parameters such as the size, the draft and the wave frequency. As a first exercise, we fix the turbine characteristics and rotational speed and study how the size of the OWC impacts the power extraction.

We present the results for a sample case with numerical values similar to those of the pilot station in Pico Island, Azores, Portugal. The inputs are : $D = 2a$, $V_o = \pi a^2 h$, $N = 2000$ rpm ; $K = 0.45$ (for one turbine); $h = 10m$; $\rho_w/\rho_a = 1000$; $g = 9.8m.s^{-2}$ and $c_a = 340m.s^{-1}$.

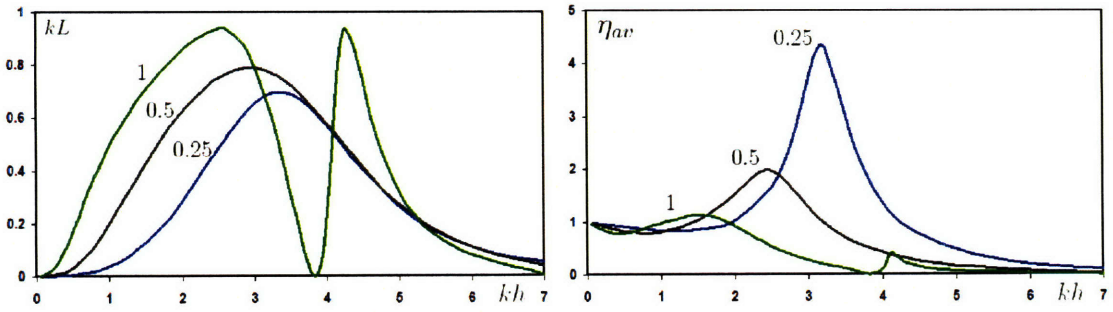

Figure 3-13: Variation against the normalized frequency kh: (i) Capture Length ; (ii) Average free surface elevation inside the OWC. $d/h = 0.2$,$h = 10m$.

The mean water surface displacement and the normalized capture length are plotted in Figure (3-13). By comparing with Figure (3-2), it can be seen that η_{av} and $\widetilde{\mathcal{B}}$ resonance frequencies are close - $kh \approx 1.5,\ 2.5,\ 3.2,\ 4.1$ for η_{av} and $kh \approx 1.9,\ 2.5,\ 3.2,\ 4.1$

for $\widetilde{\mathcal{B}}$. When the cylinder radius is not large, e.g. $a/h \leq 0.5$, there is only one resonance peak in the computed range, dominated by the Helmholtz mode where the free surface in the chamber is essentially horizontal. The peak is higher for a smaller cylinder and occurs at a larger kh. It must be noted here that for the smallest cylinder ($a/h = 0.25$) the average elevation at resonance is more than 4 times the amplitude of the incoming wave. The linearization theory used in this model is challenged for OWC's of smaller radius. Let us limit the discussion to larger structures. A practical value for an OWC is probably close to $a/h = 0.5$. Then linearization is still valid. The normalized capture length kL also features a peak around the same resonance frequency - $kh \approx 2.5,\ 2.9,\ 3.4,\ 4.2$. However, for this set of parameters, kL amplitude and bandwidth increase with the cylinder radius. It is necessary to investigate further to understand how to optimize the efficiency.

3.4.2 Optimization Power Output

For a chosen frequency the theoretical maximum power output can be found by derivating with respect to both the turbine characteristics χ and the size of the cylinder/chamber system β, yielding the well-known criteria:

$$\beta(\omega) = \widetilde{C}(\omega) \quad \text{and} \quad \chi(\omega) = \widetilde{\mathcal{B}}(\omega) \tag{3.4.1}$$

or equivalently,

$$\frac{V_o}{c_a^2 a}\frac{\rho_w}{\rho_a} = \frac{\widetilde{C}(\omega)}{\omega^2} \quad \text{and} \quad \frac{KD}{Na}\frac{\rho_w}{\rho_a} = \frac{\widetilde{\mathcal{B}}(\omega)}{\omega} \tag{3.4.2}$$

The corresponding maximum capture length follows from (3.1.11) under criteria (3.4.1),

$$kL \leq \frac{gka}{C_g \omega}\frac{\left|\widetilde{\Gamma}\right|^2}{4\widetilde{B}} \tag{3.4.3}$$

thus, after using (3.3.26), we get

$$kL_{max} = 1 \tag{3.4.4}$$

i.e. the maximum capture length is equal to the wavelength divided by 2π. In this regard, the OWC is similar to a heaving buoy.

In practise, the system geometry cannot be changed for different frequencies. It is likely easier to control the number, the blade angle and the rotation speed of the turbines, i.e., it is possible to vary the value of χ in real time over a wide interval of kh.

For a fixed pneumatic chamber volume V_o, we take $\partial L/\partial \chi = 0$ and get for optimum capture,

$$\chi(\omega) = \sqrt{\widetilde{\mathcal{B}(\omega)}^2 + \left(\widetilde{\mathcal{C}(\omega)} - \beta(\omega)\right)^2} \tag{3.4.5}$$

where all terms on the right-hand side are known functions of frequencies once the geometry is fixed. The optimum capture length is then

$$kL_{opt}(\omega) = \frac{4\widetilde{\mathcal{B}(\omega)}\sqrt{\widetilde{\mathcal{B}(\omega)}^2 + \left(\widetilde{\mathcal{C}(\omega)} - \beta(\omega)\right)^2}}{\left(\sqrt{\widetilde{\mathcal{B}(\omega)}^2 + \left(\widetilde{\mathcal{C}(\omega)} - \beta(\omega)\right)^2} + \widetilde{\mathcal{B}(\omega)}\right)^2 + \left(\widetilde{\mathcal{C}(\omega)} - \beta(\omega)\right)^2} \tag{3.4.6}$$

The maximum efficiency of 1 is achieved under the condition:

$$kL_{opt}(\omega) = 1 \quad \text{if and only if} \quad \beta(\omega) = \widetilde{\mathcal{C}}(\omega) \tag{3.4.7}$$

A typical result with this control strategy is shown in Figure 3-14. kL, η_{av}, the pressure and the turbine parameter χ are presented as functions of the incident wave frequency kh for different OWC sizes - $a/h = 0.25$; 0.5 ; 1. There is clearly a qualitative difference from figure (3-13). The capture length and the elevation now have two maximum peaks per mode (before each zero of J_0') with a significant amplitude between the two maxima. Recall that zeros of $J_0'(ka)$ correspond to zeros of $kL(ka)$ and happen first at $ka = 3.83$; 7.02. For example, in the case $a/h = 0.5$, $kL = 1$ at $kh \approx 2.6$ and $kh \approx 5.2$. For $a/h = 1$, $kL = 1$ at $kh \approx 1.9$ and $kh \approx 3.1$ for the first mode, $kL = 1$ at $kh \approx 4.1$ and $kh \approx 4.5$ for the second mode.

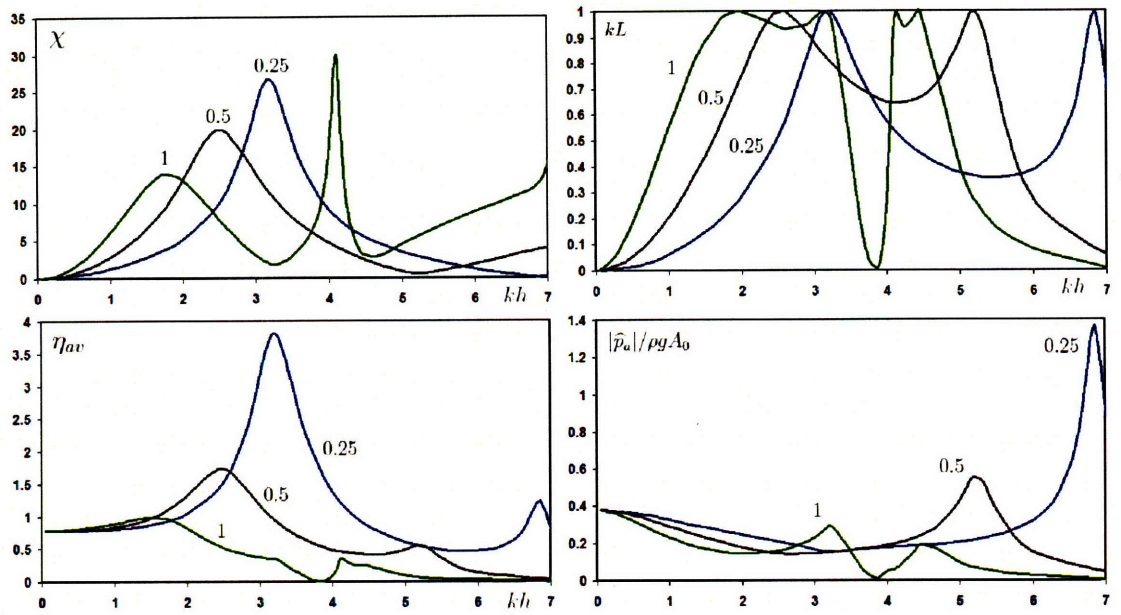

Figure 3-14: Variation against the normalized frequency kh for an optimized efficiency; (i) Non-dimensional turbine parameter. (ii) Capture Length . (iii) Average free surface elevation inside the OWC ; (iv) Average pressure inside OWC; For $a/h =$ 0.25 0.5 ; 1. In all cases $h = 10m$, $d/h = 0.2$, $V_o = \pi a^2 h$.

Note that the pressure and turbine parameter χ show only one peak per mode each, corresponding respectively to the frequency of the second ($kh \approx 5.2$ for $a/h = 0.5$) and first ($kh \approx 2.6$ for $a/h = 0.5$) peak of the capture length. The reason is as follows. At these frequencies, the expression of χ and $\widehat{p}_a$ - respectively (3.4.5) and (3.1.8) - can be simplified by using the fact that $\beta = \widetilde{C}$. It implies that $\chi = \widetilde{\mathcal{B}}$ and $\widehat{p}_a \propto 1/\sqrt{\widetilde{\mathcal{B}}}$. Now, $\mathcal{B}$ is maximum around the first peak ($kh \approx 2.6$) and very small at the second ($kh \approx 5.2$) as shown in figure (3-2). Hence χ is small but $\widehat{p}_a$ is large at $kh \approx 5.2$.

The increase in efficiency brought by the control strategy appears clearly when comparing directly the capture length for the same OWC geometry without control for different fixed turbine characteristics as in Figure (3-15). By construction, the optimized OWC has always a capture length at least equal to any passive case value. The optimized case is the envelope of the curves when χ varies.

Let's now look more closely at this double peak behaviour. This phenomenon has been described by Sarmento and Falcão [14]. It has been shown earlier that

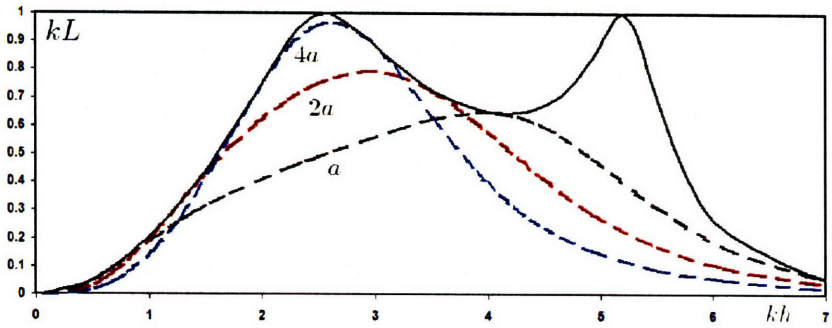

Figure 3-15: Capture length against the normalized frequency kh with fixed parameter turbines (dashed lines) and an optimized turbine (solid line); $d/h = 0.2$; $d/h = 0.5$; $h = 10m$. For the fixed parameter turbines: $N = 2000$ rpm ; $K = 0.45$; $D = a$, $2a$, $4a$.

the capture length is at its maximum reachable value, i.e. 1, when $\beta = \widetilde{C}$ (3.4.7). Indeed, Figure (3-16) shows that the frequencies for which $kL = 1$ (bottom graph) correspond to points where the $\beta(kh)$ and $\widetilde{C}(kh)$ curves intersect. Then, the double peak is explained by the added mass profile. For each mode, the added mass curve has a bell-shaped part which can intersect twice the $\beta(kh)$ curve. We note that $\beta = -\frac{\omega^2 V_o}{c_a^2 a}\frac{\rho_w}{\rho_a} \propto -\omega^2 \propto -kh\tanh(kh)$ so that $\beta \propto -kh$ for kh large. The variation is almost linear for most frequencies.

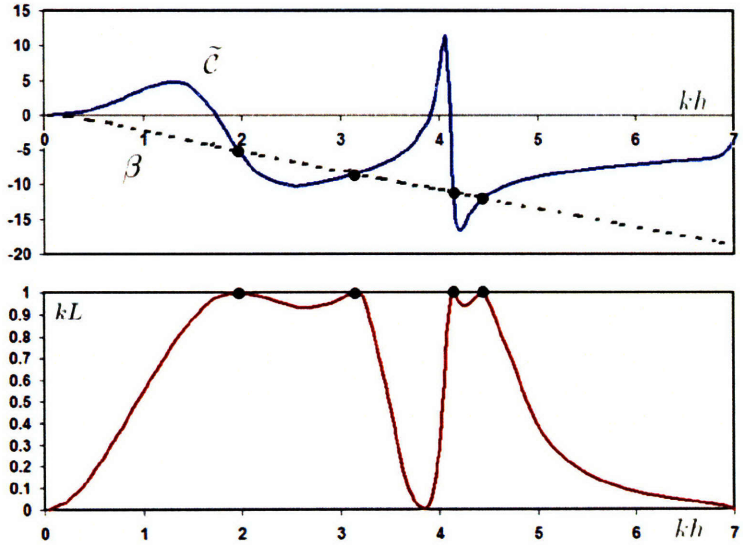

Figure 3-16: Variation with the normalized frequency kh for an optimized efficiency ; $d/h = 0.2$; $a/h = 1$; $h = 10m$. (bottom) The capture length equals 1 when (top) the added mass - solid line - equals the β - dotted line.

A well-known strategy to increase energy extraction efficiency is to introduce control in the power-takeoff system and to make the extraction rate complex where the real part corresponds to *elasticity*. In the OWC system air compressibility provides, through β, such elasticity. The air in the chamber amounts to an elastic spring of negative elasticity whose amplitude increases monotonically with the wave frequency.

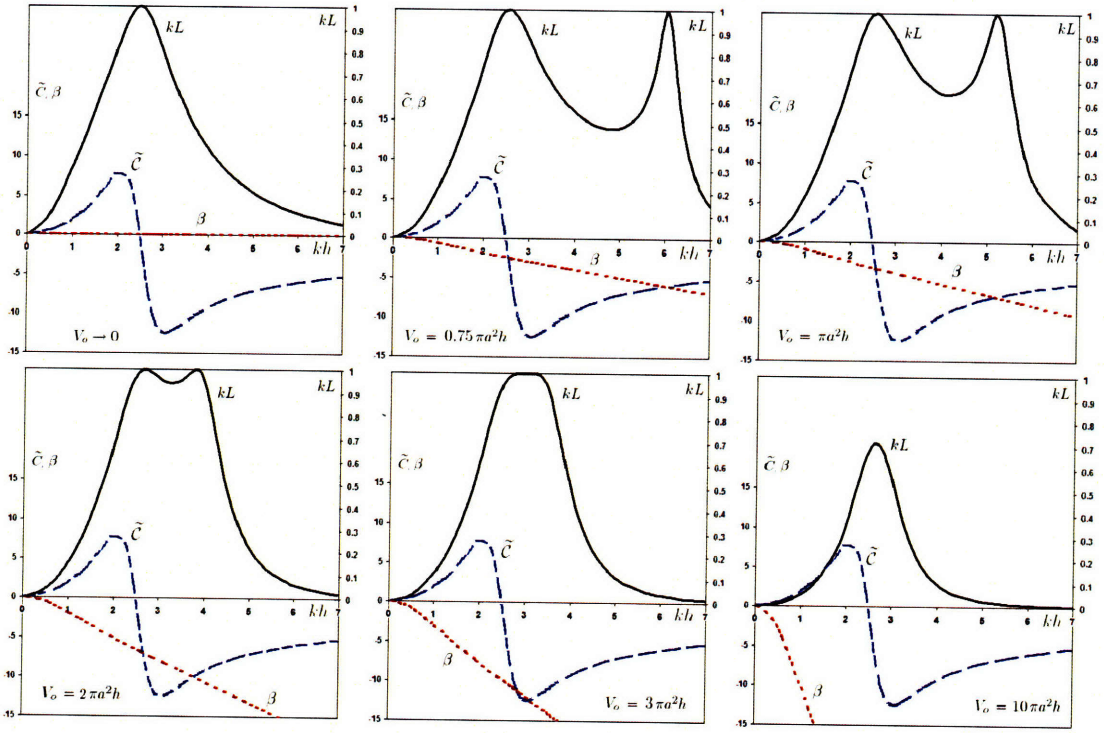

Figure 3-17: Capture length (solid), added mass (dashed) and β coefficient (dotted) against the normalized frequency kh (optimized efficiency) for different pneumatic chamber volumes V_o ; $a/h = 0.5$, $d/h = 0.2$; $h = 10m$: (i) $V_o \to 0$ (uncompressible case) ; (ii) $V_o = 2\pi a^2 h$; (iii) $V_o = 10\pi a^2 h$.

Since the efficiency depends on the relative behaviour of $\widetilde{C}$ and β, we shall study how changes in the latter quantity affect the results. Recall that β is linked to the characteristics of the air chamber through its volume V_o and the speed of sound in air c_a which accounts for compressibility - $\beta = -\frac{\omega^2 V_o}{c_a^2 a}\frac{\rho_w}{\rho_a}$. The following discussion is similar to that by Sarmento & Falcão [14] for a two-dimensional geometry. Let us fix the size and geometry of the immersed part of the OWC but consider different sizes of the air chamber V_0. Beginning from a relatively small volume, as V_o increases, the $\beta(kh)$ curve is shifted downwards causing the two intersection points with $\widetilde{C}(kh)$ to

converge towards the local minimum of this function at $kh \approx 3$. This means that the two peaks of the capture length curve also converge into a single peak - cases (ii), (iii) and (iv). At the same time, as the distance between the two intersection points decrease, it leads to a higher amplitude of the capture length in this frequency range. In the limiting case (v), as V_o is increased further, $\widetilde{C}(kh)$ and $\beta(kh)$ become tangent to each other. Then, the two intersection points coalesce. The OWC now only has a single resonance frequency. If V_o continues to increase, there is no intersection anymore between $\widetilde{C}(kh)$ and $\beta(kh)$. Thus, the capture length profile does not reach the maximum value 1 anymore - see (vi). This corresponds to poor efficiency. The limit is $V_o \rightarrow 0$ (i) is equivalent to an incompressible approximation, i.e. $c_a \rightarrow \infty$. In this case, β is equal to zero. Thus, the capture length has only one maximum at the frequency where $\widetilde{C}$ vanishes. Compared to cases (ii) to (vi), this situation leads to a much smaller bandwidth and a smaller height in the neighbourhood of the resonance frequencies.

Finally we show the effects of the draft d/h on the extraction efficiency in Figure (3-18) on kL_{opt}, η_{av}, $\widetilde{P}$ and the optimum χ for different values of cylinder draft $d/h = 0.1$; 0.2 ; 0.3. It can be seen that a smaller draft leads to a better efficiency (bandwidth and amplitude) for this particular choice of chamber volume. Resonance occurs at higher frequencies if the draft is smaller. Recall that as the draft decreases, the curve of $\widetilde{C}(kh)$ becomes flatter. This means that the two intersection points between $\beta(kh)$ and $\widetilde{C}$ curve are wider apart. This explains why the smaller draft corresponds to a broader efficiency bandwidth.

Practical concerns may limit how small the draft can be. In fact, for an OWC, the wall must be deep enough so that air cannot penetrate inside the cylinder for large amplitude waves.

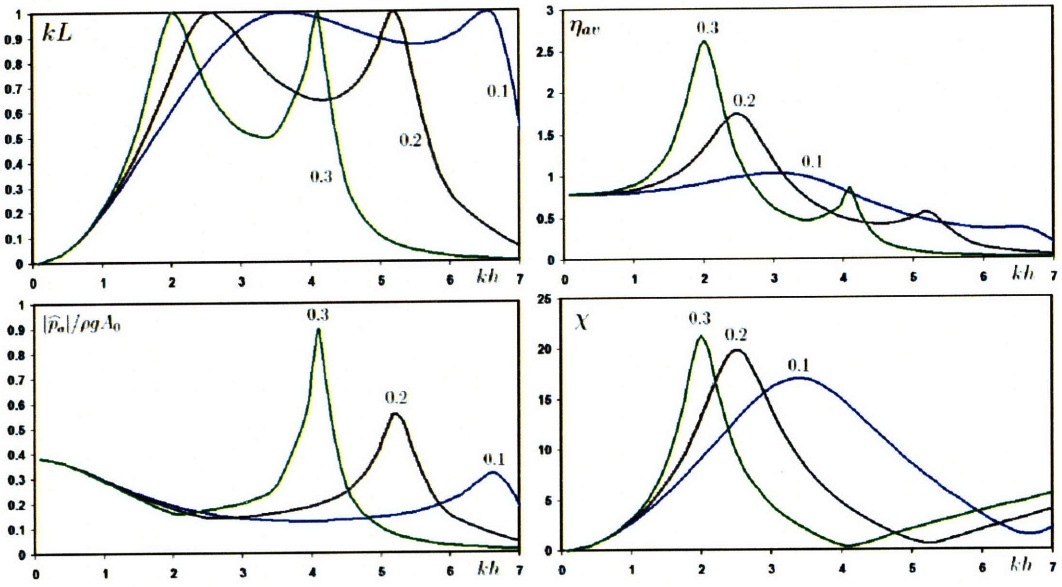

Figure 3-18: Variation against the normalized frequency kh for an optimized efficiency: (i) Capture Length ; (ii) Average free surface elevation inside the OWC ; (iii) Radiation damping ; (iv) Added mass ; (v) Average pressure ; (vi) Non-dimensional turbine parameter. $d/h =$ 0.1 0.2 ; 0.3. In all cases $a/h = 0.5$, $h = 10m$.

Chapter 4

OWC on a Straight Coast

We shall consider here a different configuration consisting of an OWC installed on a straight coastline which is equivalent to a 180° wedge as shown in figure (4-1). In this case, it can be anticipated that the power extraction will no longer be independent of the incidence angle. Let us adopt the model developed in the previous sections to this new geometry.

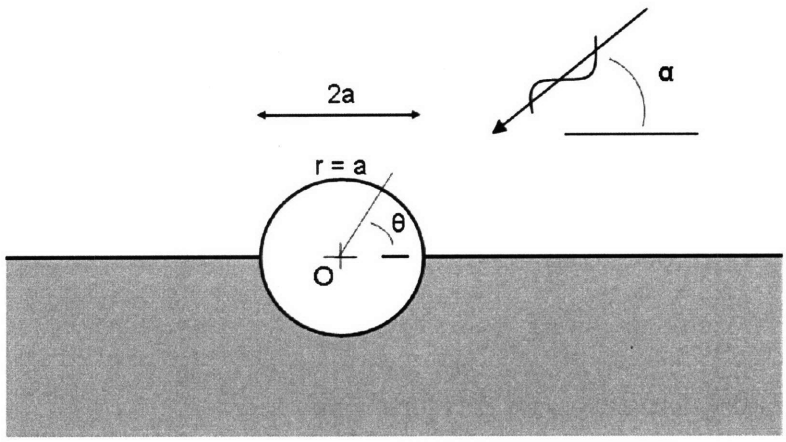

Figure 4-1: Sketch of the considered configuration: OWC installed on a straight coastline.

4.1 Radiation Problem

The velocity potentials both inside (ϕ_C) and outside (ϕ_O) the column is governed by the Laplace equation. On the free surface inside the column, the air pressure is assumed to be uniform in space so that

$$\frac{\partial \phi_C}{\partial z} - \frac{\omega^2}{g}\phi_C = \frac{i\omega}{\rho g}P, \quad z = 0, \quad r < a \tag{4.1.1}$$

Outside the column the water surface is pressure-free. Waves can only be outgoing. In the form of an eigenfunction expansion, using the angular symmetry, the potential inside the chamber is:

$$\phi_C = \frac{-iP}{\rho\omega}\sum_{\ell=0}^{\infty}\sum_{n=0}^{\infty} D_{n\ell}\frac{I_n(\kappa_\ell r)}{\kappa_\ell a\ I_n'(\kappa_\ell a)}Z_\ell(z)\cos\left(n\left[\theta - \frac{\pi}{2}\right]\right) - \frac{iP}{\rho\omega} \tag{4.1.2}$$

The outside potential can be expressed as

$$\phi_O = \frac{-iP}{\rho\omega}\sum_{\ell=0}^{\infty}\sum_{n=0}^{\infty} E_{n\ell}\frac{K_{2n}(\kappa_\ell r)}{\kappa_\ell a\ K_{2n}'(\kappa_\ell a)}Z_\ell(z)\cos(2n\theta) \tag{4.1.3}$$

It satisfies the no-flux boundary condition on the half lines $\theta = 0$ and $\theta = \pi$ and is symmetric with respect to the direction $\theta = \frac{\pi}{2}$.

The unknown coefficients $D_{n\ell}, E_{n\ell}$ must be chosen to ensure the continuity of potential and radial flux on the open part of the column surface,

$$\phi_O = \phi_C \quad \text{and} \quad \frac{\partial \phi_O}{\partial r} = \frac{\partial \phi_C}{\partial r} = U(z,\theta), \quad r = a, \quad -h \le z \le -d, \ 0 \le \theta \le \pi. \tag{4.1.4}$$

Taking the radial derivatives, we get, for $r = a$:

$$\begin{aligned}
\frac{\partial \phi_O}{\partial r} &= \frac{-iP}{\rho\omega}\sum_{\ell=0}^{\infty}\sum_{n=0}^{\infty} E_{n\ell}Z_\ell(z)\cos(2n\theta) \ ; \\
\frac{\partial \phi_C}{\partial r} &= \frac{-iP}{\rho\omega}\sum_{\ell=0}^{\infty}\sum_{n=0}^{\infty} D_{n\ell}Z_\ell(z)\cos(n\left[\theta - \frac{\pi}{2}\right])
\end{aligned} \tag{4.1.5}$$

By invoking the condition of flux continuity, we get

$$\frac{\pi}{\epsilon_n} E_{n\ell} = \frac{i\rho\omega}{Ph} \int_0^{\pi} \int_{-h}^{-d} U(z,\theta) Z_\ell(z) \cos(2n\theta) d\theta dz \tag{4.1.6}$$

$$\frac{2\pi}{\epsilon_n} D_{n\ell} = \frac{i\rho\omega}{Ph} \int_0^{\pi} \int_{-h}^{-d} U(z,\theta) Z_\ell(z) \cos(n\left[\theta - \frac{\pi}{2}\right]) d\theta dz \tag{4.1.7}$$

Continuity of the potential on $r = a, -h \leq z \leq -d, 0 \leq \theta \leq \pi$ requires

$$\sum_{\ell=0}^{\infty} \sum_{n=0}^{\infty} E_{n\ell} \frac{K_{2n}(\kappa_\ell a)}{\kappa_\ell a \; K'_{2n}(\kappa_\ell a)} Z_\ell(z) \cos(2n\theta) \;=\; 1 \;+ \sum_{\ell=0}^{\infty} \sum_{n=0}^{\infty} D_{n\ell} \frac{I_n(\kappa_\ell a)}{\kappa_\ell a \; I'_n(\kappa_\ell a)} Z_\ell(z) \cos(n\left[\theta - \frac{\pi}{2}\right]) \tag{4.1.8}$$

which leads to an integral equation for $U(z)$:

$$\begin{aligned} -\frac{iP}{a\rho\omega} \;=\; & \sum_{\ell=0}^{\infty} \sum_{n=0}^{\infty} \left\{ \frac{\epsilon_n}{\pi h} \int_{-h}^{-d} Z_\ell(z') \left[\int_0^{\pi} U(z',\theta') \cos(2n\theta') d\theta' \frac{K_{2n}(\kappa_\ell a)}{\kappa_\ell K'_{2n}(\kappa_\ell a)} \cos(2n\theta) \right.\right. \\ & \left.\left. - \frac{1}{2} \int_0^{\pi} U(z',\theta') \cos(n\left[\theta' - \frac{\pi}{2}\right]) d\theta' \frac{I_n(\kappa_\ell a)}{\kappa_\ell I'_n(\kappa_\ell a)} \cos(n\left[\theta - \frac{\pi}{2}\right]) \right] dz' Z_\ell(z) \right\} \end{aligned} \tag{4.1.9}$$

Taking into account the symmetry of the problem and adapting from (3.2.13), $U(z,\theta)$ is expressed as:

$$U(z,\theta) = \frac{-iP}{\rho\omega} \sum_{m=0}^{\infty} \sum_{p=0}^{\infty} \alpha_{mp} \cos(2m\left[\theta - \frac{\pi}{2}\right]) u_p(z) \tag{4.1.10}$$

Let us recall that:

$$u_p(z) = \frac{2(-1)^p}{\pi\sqrt{(h-d)^2 - (z+h)^2}} T_{2p}\left(\frac{z+h}{h-d}\right) \tag{4.1.11}$$

where T_n is the n^{th} Chebychev polynomials. Moreover:

$$F_{p\ell} \equiv \int_{-h}^{-d} u_p(z) Z_\ell(z) dz = N_\ell^{-1/2} J_{2p}\{\kappa_\ell(h-d)\} \tag{4.1.12}$$

$$R_{mn} \equiv \int_0^\pi \cos(2m\left[\theta - \frac{\pi}{2}\right]) \cos(n\left[\theta - \frac{\pi}{2}\right]) d\theta = \begin{cases} \frac{\pi}{\epsilon_m} & 2m = n, \\ \frac{(-1)^m 2n \sin\left(\frac{n\pi}{2}\right)}{n^2 - 4m^2} & 2m \neq n, \end{cases} \tag{4.1.13}$$

$$\int_0^\pi \cos(2m\left[\theta - \frac{\pi}{2}\right]) \cos(2n\theta)\, d\theta = (-1)^m \frac{\pi}{\epsilon_m}\, \delta_{mn} \tag{4.1.14}$$

This leads to the relation:

$$\begin{aligned} \frac{h}{a} &= \sum_{\ell=0}^{\infty}\sum_{n=0}^{\infty}\sum_{p=0}^{\infty}\sum_{m=0}^{\infty} \left\{ \frac{\epsilon_n}{\pi} \left[\alpha_{mp} F_{p\ell} \frac{\pi(-1)^m \delta_{mn}}{\epsilon_m} \frac{K_{2n}(\kappa_\ell a)}{\kappa_\ell a\, K'_{2n}(\kappa_\ell a)} \cos(2n\theta) \right.\right. \\ &- \left.\left. \frac{1}{2}\, \alpha_{mp} F_{p\ell} R_{mn} \frac{I_n(\kappa_\ell a)}{\kappa_\ell a\, I'_n(\kappa_\ell a)} \cos(n(\theta - \frac{\pi}{2})) \right] Z_\ell(z) \right\} \end{aligned} \tag{4.1.15}$$

which, after multiplying both sides by $\cos\left(2M\left[\theta - \frac{\pi}{2}\right]\right) . u_P(z)$ and integrating for $\theta \in [0, \pi]$ and $z \in [-h, 0]$, yields, for any pair of integer (M, P):

$$\begin{aligned} \pi \frac{h}{a} \delta_{P0} \delta_{M0} &= \sum_{p=0}^{\infty} \alpha_{Mp} \sum_{\ell=0}^{\infty} \left\{ \frac{\pi}{\epsilon_M} F_{p\ell} \frac{K_{2M}(\kappa_\ell a)}{\kappa_\ell a\, K'_{2M}(\kappa_\ell a)} F_{P\ell} \right\} \\ &- \sum_{m=0}^{\infty}\sum_{p=0}^{\infty} \alpha_{mp} \sum_{n=0}^{\infty}\sum_{\ell=0}^{\infty} \left\{ \frac{\epsilon_n}{2\pi} F_{p\ell} R_{mn} \frac{I_n(\kappa_\ell a)}{\kappa_\ell a\, I'_n(\kappa_\ell a)} R_{Mn} F_{P\ell} \right\} \end{aligned} \tag{4.1.16}$$

This linear system of equations can be solved numerically for the variables $\{\alpha_{mp}\}$. This gives the complete solution for the flow resulting of the radiation problem.

The radiation damping and added mass $\widetilde{\mathcal{B}}$ and $\widetilde{\mathcal{C}}$ are deduced from the $D_{n\ell}$ coefficients:

$$Q^R = -(\mathcal{B} - i\mathcal{C})p_a = \iint_{S_c} \left.\frac{\partial \phi_C}{\partial z}\right|_{z=0} dS \tag{4.1.17}$$

so that

$$\widetilde{\mathcal{B}} = \Re\left\{\iint_{S_c} \sum_{\ell} \frac{iD_{0\ell}}{a} \frac{I_0(\kappa_\ell r)}{\kappa_\ell a\ I_0'(\kappa_\ell a)} Z_\ell'(0) dS\right\} \tag{4.1.18}$$

and

$$\widetilde{\mathcal{C}} = -\Im\left\{\iint_{S_c} \sum_{\ell} \frac{iD_{0\ell}}{a} \frac{I_0(\kappa_\ell r)}{\kappa_\ell a\ I_0'(\kappa_\ell a)} Z_\ell'(0) dS\right\} \tag{4.1.19}$$

4.2 Diffraction Problem

We assume that the incident wave arrives from the direction $\theta = \alpha$ with respect the breakwater (the x axis). The total potential outside the column is composed of two parts: φ_D due to a solid cylinder extending the entire depth, and φ_R due to the opening.

$$\varphi_O(r, \theta, z) \;=\; \varphi_D + \varphi_R \tag{4.2.20}$$

where the first part is known from Appendix B and can be rewritten as

$$\varphi_D = \frac{-igA_o}{\omega} \sum_{n=0}^{\infty} \frac{2\epsilon_n i \cos n\alpha e^{-\frac{in\pi}{2}} Y_n'(ka)}{H_n'(ka)} \left(J_n(kr) - \frac{J_n'(ka)}{Y_n'(ka)} Y_n(kr)\right) \frac{Z_0(z)}{Z_0(0)} \cos n\theta \tag{4.2.21}$$

Let us note that:

$$\begin{aligned}
\varphi_D &= \frac{-igA_o}{\omega}\sum_{n=0}^{\infty} 2\epsilon_n(-i)^n\left(\frac{iY_n'(ka)}{H_n'(ka)}J_n(kr)-\frac{iJ_n'(ka)}{H_n'(ka)}Y_n(kr)\right)\frac{Z_0(z)}{Z_0(0)}\cos n\alpha\cos n\theta \\
&= \frac{-igA_o}{\omega}\sum_{n=0}^{\infty} 2\epsilon_n(-i)^n\left(J_n(kr)-\frac{J_n'(ka)}{H_n'(ka)}J_n(kr)-\frac{iJ_n'(ka)}{H_n'(ka)}Y_n(kr)\right) \\
&\qquad\qquad \cdot\ \frac{Z_0(z)}{Z_0(0)}\cos n\alpha\cos n\theta \\
&= \frac{-igA_o}{\omega}\sum_{n=0}^{\infty} 2\epsilon_n(-i)^n\left(J_n(kr)-\frac{J_n'(ka)}{H_n'(ka)}H_n(kr)\right)\frac{Z_0(z)}{Z_0(0)}\cos n\alpha\cos n\theta \\
&= \frac{-igA_o}{\omega}\sum_{n=0}^{\infty} \epsilon_n(-i)^n\left(J_n(kr)-\frac{J_n'(ka)}{H_n'(ka)}H_n(kr)\right)\frac{Z_0(z)}{Z_0(0)} \\
&\qquad\qquad \cdot\ \{\cos(n[\alpha+\theta])+\cos(n[\alpha-\theta])\}
\end{aligned} \tag{4.2.22}$$

Physically, this is the potential created by the superposition of two symmetrically incident waves scattered by a cylinder extending to the bottom without breakwater. The two incident wave directions are $\pi+\alpha$ and $\pi-\alpha$.

The second part φ_R due the opening is

$$\varphi_R = \frac{-igA_o}{\omega}\sum_{\ell=0}^{\infty} Z_\ell(z)\sum_{n=0}^{\infty} A_{n\ell}\frac{K_n(\kappa_\ell r)}{\kappa_\ell a\ K_n'(\kappa_\ell a)}\cos n\theta \tag{4.2.23}$$

which satisfies:

$$\frac{\partial\varphi_R}{\partial\theta} = 0, \quad \theta = 0,\ \pi \qquad \text{for all } r > a \tag{4.2.24}$$

Inside the column ($r < a$), we have:

$$\varphi_C = \frac{-igA_o}{\omega}\sum_{n=0}^{\infty}\sum_{\ell=0}^{\infty}(B_{n\ell}\cos n\theta + C_{n\ell}\sin n\theta)\frac{I_n(\kappa_\ell r)}{\kappa_\ell a\ I_n'(\kappa_\ell a)}Z_\ell(z) \tag{4.2.25}$$

where $B_{n\ell}$ and $C_{n\ell}$ are unknown. Note that for $\ell = 0$, $\kappa_0 = -ik$ and

$$I_n(-ikr) = (-i)^n J_n(kr) \tag{4.2.26}$$

Since φ_D already satisfies the no flux condition on the wall of the cylinder, continuity of radial velocity requires

$$\frac{\partial \varphi_R}{\partial r} = \frac{\partial \varphi_C}{\partial r} = \begin{cases} 0 & -d < z < 0 \quad \text{or} \quad \pi < \theta < 2\pi \\ U(z,\theta) & -h < z < -d \ ; \ 0 \le \theta \le \pi \end{cases} \tag{4.2.27}$$

which implies :

$$\begin{aligned} \sum_{n=0}^{\infty}\sum_{\ell=0}^{\infty} A_{n\ell}\cos n\theta Z_\ell(z) &= \sum_{n=0}^{\infty}\sum_{\ell=0}^{\infty}\left(B_{n\ell}\cos n\theta + C_{n\ell}\sin n\theta\right) Z_\ell(z) \\ &= \begin{cases} 0 & -d < z < 0 \quad \text{or} \quad \pi < \theta < 2\pi \\ \frac{ia\omega}{gA_o}U(z,\theta) & -h < z < -d \ ; \ 0 \le \theta \le \frac{3\pi}{2} \end{cases} \end{aligned} \tag{4.2.28}$$

Using orthogonality, we get for any ℓ and n:

$$\frac{\pi}{\epsilon_n} A_{n,\ell} = \frac{ia\omega}{ghA_o}\int_0^{\pi}\int_{-h}^{-d} U(\theta,z)Z_\ell(z)\cos(n\theta)d\theta dz \tag{4.2.29}$$

$$\frac{2\pi}{\epsilon_n}\{B_{n,\ell}\ ;\ C_{n,\ell}\} = \frac{ia\omega}{ghA_o}\int_0^{\pi}\int_{-h}^{-d} U(\theta,z)Z_\ell(z)\{\cos(n\theta)\ ;\ \sin(n\theta)\}d\theta dz \tag{4.2.30}$$

Continuity of potentials requires for $-h < z < -d$, $0 \le \theta \le \frac{3\pi}{2}$:

$$\begin{aligned} &\textstyle\sum_{n=0}^{\infty} \frac{2\epsilon_n i\cos n\alpha e^{-\frac{in\pi}{2}}Y_n'(ka)}{H_n'(ka)}\left(J_n(ka) - \frac{J_n'(ka)}{Y_n'(ka)}Y_n(ka)\right)\frac{Z_0(z)}{Z_0(0)}\cos n\theta \\ &\qquad + \textstyle\sum_{\ell=0}^{\infty}\sum_{n=0}^{\infty} A_{n\ell}\frac{K_n(\kappa_\ell a)}{\kappa_\ell a\ K_n'(\kappa_\ell a)}Z_\ell(z)\cos n\theta \\ &\quad = \textstyle\sum_{n=0}^{\infty}\sum_{\ell=0}^{\infty}\left(B_{n\ell}\cos n\theta + C_{n\ell}\sin n\theta\right)\frac{I_n(\kappa_\ell a)}{\kappa_\ell a\ I_n'(\kappa_\ell a)}Z_\ell(z) \end{aligned} \tag{4.2.31}$$

Let us denote for brevity:

$$\mathcal{F}_n = \frac{2\epsilon_n i\cos n\alpha e^{-\frac{in\pi}{2}}Y_n'(ka)}{Z_0(0)H_n'(ka)}\left(J_n(ka) - \frac{J_n'(ka)}{Y_n'(ka)}Y_n(ka)\right) \tag{4.2.32}$$

This yields:

$$\sum_{n=0}^{\infty}\left[\mathcal{F}_n\cos n\theta\ Z_0(z)+\sum_{\ell=0}^{\infty}A_{n\ell}\frac{K_n(\kappa_\ell a)}{\kappa_\ell a\ K_n'(\kappa_\ell a)}Z_\ell(z)\cos n\theta\right]$$
$$=\sum_{n=0}^{\infty}\sum_{\ell=0}^{\infty}\left(B_{n\ell}\cos n\theta+C_{n\ell}\sin n\theta\right)\frac{I_n(\kappa_\ell a)}{\kappa_\ell a\ I_n'(\kappa_\ell a)}Z_\ell(z) \tag{4.2.33}$$

After using (4.2.29, 4.2.30), it can be rewritten as:

$$\begin{aligned}
&\sum_{n=0}^{\infty}\sum_{\ell=0}^{\infty}\frac{\epsilon_n}{2\pi}\frac{1}{h}\int_0^{\pi}\int_{-h}^{-d}U(\theta',z')Z_\ell(z')\sin(n\theta')d\theta'dz'\sin(n\theta)\frac{I_n(\kappa_\ell a)}{\kappa_\ell a\ I_n'(\kappa_\ell a)}Z_\ell(z)\\
+\ &\sum_{n=0}^{\infty}\sum_{\ell=0}^{\infty}\frac{\epsilon_n}{2\pi}\frac{1}{h}\int_0^{\pi}\int_{-h}^{-d}U(\theta',z')Z_\ell(z')\cos(n\theta')d\theta'dz'\cos(n\theta)\frac{I_n(\kappa_\ell a)}{\kappa_\ell a\ I_n'(\kappa_\ell a)}Z_\ell(z)\\
=\ &\sum_{n=0}^{\infty}\sum_{\ell=0}^{\infty}\frac{\epsilon_n}{\pi}\frac{1}{h}\int_0^{\pi}\int_{-h}^{-d}U(\theta',z')Z_\ell(z')\cos(n\theta')d\theta'dz'\frac{K_n(\kappa_\ell a)}{\kappa_\ell a\ K_n'(\kappa_\ell a)}Z_\ell(z)\cos(n\theta)\\
+\ &\frac{igA_o}{a\omega}\sum_{n=0}^{\infty}\mathcal{F}_n\cos n\theta\ Z_0(z)
\end{aligned} \tag{4.2.34}$$

which is an integral equation for $U(\theta,z)\ ;\ 0\le\theta\le\pi\ ,\ -h\le z\le -d$:

$$\iint d\theta'dz'U(z',\theta')\mathcal{K}(z,\theta;z',z',\theta')=\frac{igA_o}{a\omega}\sum_{n=0}^{\infty}\mathcal{F}_n\cos n\theta\ Z_0(z) \tag{4.2.35}$$

with the kernel:

$$\begin{aligned}
\mathcal{K}(z,\theta;z',\theta')\equiv&-\sum_{n=0}^{\infty}\sum_{\ell=0}^{\infty}\frac{\epsilon_n}{\pi h}\frac{K_n(\kappa_\ell a)}{\kappa_\ell a\ K_n'(\kappa_\ell a)}Z_\ell(z)Z_\ell(z')\cos(n\theta)\cos(n\theta')\\
&+\sum_{n=0}^{\infty}\sum_{\ell=0}^{\infty}\frac{\epsilon_n}{2\pi h}\frac{I_n(\kappa_\ell a)}{\kappa_\ell a\ I_n'(\kappa_\ell a)}Z_\ell(z)Z_\ell(z')\left[\sin(n\theta)\sin(n\theta')+\cos(n\theta)\cos(n\theta')\right]
\end{aligned} \tag{4.2.36}$$

Now, we solve for $U(\theta,z)$ by expanding it as a series of base functions. Expecting

singularities of the velocity at $z = -d$, let us write $U(\theta, z)$ as:

$$U(\theta, z) = \frac{-igA_o}{\omega} \sum_{m=0}^{\infty} \sum_{p=0}^{\infty} (\alpha_{mp} \cos m\theta + \beta_{mp} \sin m\theta)\, u_p(z) \tag{4.2.37}$$

The following integrals can be easily evaluated:

$$\int_0^{\pi} \cos(m\theta) \cos(n\theta) d\theta = \frac{\pi}{\epsilon_m} \delta_{nm} \tag{4.2.38}$$

$$\int_0^{\pi} \sin(n\theta) \sin(m\theta) d\theta = \frac{\pi}{2} \delta_{nm} (1 - \delta_{m0}) \tag{4.2.39}$$

$$\int_0^{\pi} \cos(m\theta) \sin(n\theta) d\theta = \frac{n(1 - (-1)^{n+m})}{n^2 - m^2} \tag{4.2.40}$$

Using this notation, the integral equation (4.2.34) or (4.2.35) can be rewritten as:

$$\begin{aligned}
\sum_{n=0}^{\infty} \sum_{\ell=0}^{\infty} \sum_{m=0}^{\infty} \sum_{p=0}^{\infty} \Bigg[& -2\pi \alpha_{mp} F_{p\ell} \delta_{mn} \frac{K_n(\kappa_\ell a)}{\kappa_\ell a\, K_n'(\kappa_\ell a)} \cos n\theta Z_\ell(z) \\
& -2\epsilon_n \beta_{mp} F_{p\ell} \frac{m(1 - (-1)^{n+m})}{m^2 - n^2} \frac{K_n(\kappa_\ell a)}{\kappa_\ell a\, K_n'(\kappa_\ell a)} \cos n\theta Z_\ell(z) \\
& + \epsilon_n \beta_{mp} \left(\frac{\pi}{2} \delta_{nm} (1 - \delta_{m0}) \sin n\theta + \frac{m(1 - (-1)^{n+m})}{m^2 - n^2} \cos n\theta \right) F_{p\ell} \frac{I_n(\kappa_\ell a)}{\kappa_\ell a\, I_n'(\kappa_\ell a)} Z_\ell(z) \\
& + \epsilon_n \alpha_{mp} \left(\frac{\pi}{\epsilon_m} \delta_{nm} \cos n\theta + \frac{n(1 - (-1)^{n+m})}{n^2 - m^2} \sin n\theta \right) F_{p\ell} \frac{I_n(\kappa_\ell a)}{\kappa_\ell a\, I_n'(\kappa_\ell a)} Z_\ell(z) \Bigg] \\
& = \sum_{n=0}^{\infty} 2\pi \frac{h}{a} \mathcal{F}_n \cos n\theta Z_0(z)
\end{aligned} \tag{4.2.41}$$

By multiplying the above with $u_P(z) \cos M\theta$ and $u_P(z) \sin M\theta$ in turn and integrating

over the range $0 < \theta < \pi$, $-h < z - d$, we get for any integer P and M:

$$\frac{2\pi^2 h}{\epsilon_M a}\mathcal{F}_M F_{P0} = \sum_{n=0}^{\infty}\sum_{\ell=0}^{\infty}\sum_{m=0}^{\infty}\sum_{p=0}^{\infty}\Bigg[\quad -\frac{2\pi^2}{\epsilon_M}\delta_{mn}\delta_{Mn}\alpha_{Mp}F_{p\ell}F_{P\ell}\frac{K_M(\kappa_\ell a)}{\kappa_\ell a\ K'_M(\kappa_\ell a)}$$
$$+\epsilon_n\beta_{mp}\left(\frac{\pi}{2}\delta_{nm}\left(1-\delta_{m0}\right)\frac{n(1-(-1)^{n+M})}{n^2-M^2}\right.$$
$$\left. +\ \frac{m(1-(-1)^{n+m})}{m^2-n^2}\frac{\pi}{\epsilon_M}\delta_{Mn}\right)F_{p\ell}F_{P\ell}\frac{I_n(\kappa_\ell a)}{\kappa_\ell a\ I'_n(\kappa_\ell a)}$$
$$+\epsilon_n\alpha_{mp}\left(\frac{\pi^2}{\epsilon_M^2}\delta_{nm}\delta_{Mn}+\frac{n(1-(-1)^{n+m})}{n^2-m^2}\frac{n(1-(-1)^{n+M})}{n^2-M^2}\right)F_{p\ell}F_{P\ell}\frac{I_n(\kappa_\ell a)}{\kappa_\ell a\ I'_n(\kappa_\ell a)}$$
$$-2\pi\beta_{mp}F_{p\ell}F_{P\ell}\frac{m(1-(-1)^{M+m})}{m^2-M^2}\delta_{Mn}\frac{K_M(\kappa_\ell a)}{\kappa_\ell a\ K'_M(\kappa_\ell a)} \quad \Bigg] \tag{4.2.42}$$

and

$$\sum_{n=0}^{\infty}2\pi\frac{h}{a}\mathcal{F}_n\frac{M(1-(-1)^{M+n})}{M^2-n^2}F_{P0} \quad =$$
$$\sum_{n=0}^{\infty}\sum_{\ell=0}^{\infty}\sum_{m=0}^{\infty}\sum_{p=0}^{\infty}\Bigg[-2\epsilon_n\beta_{mp}F_{p\ell}\frac{m(1-(-1)^{n+m})}{m^2-n^2}\frac{K_n(\kappa_\ell a)}{\kappa_\ell a\ K'_n(\kappa_\ell a)}\frac{M(1-(-1)^{M+n})}{M^2-n^2}F_{P\ell}$$
$$+\epsilon_n\beta_{mp}\left(\frac{\pi}{2}\delta_{nm}\left(1-\delta_{m0}\right)\frac{\pi}{2}\delta_{Mn}\left(1-\delta_{M0}\right)+\frac{m(1-(-1)^{n+m})}{m^2-n^2}\frac{M(1-(-1)^{M+n})}{M^2-n^2}\right)$$
$$\cdot\ F_{p\ell}\frac{I_n(\kappa_\ell a)}{\kappa_\ell a\ I'_n(\kappa_\ell a)}F_{P\ell}$$
$$+\epsilon_n\alpha_{mp}\left(\frac{\pi}{\epsilon_m}\delta_{nm}\frac{M(1-(-1)^{M+n})}{M^2-n^2}+\frac{n(1-(-1)^{n+m})}{n^2-m^2}\frac{\pi}{2}\delta_{Mn}\left(1-\delta_{M0}\right)\right)$$
$$\cdot\ F_{p\ell}\frac{I_n(\kappa_\ell a)}{\kappa_\ell a\ I'_n(\kappa_\ell a)}F_{P\ell}$$
$$-2\pi\alpha_{mp}F_{p\ell}\delta_{mn}\frac{K_n(\kappa_\ell a)}{\kappa_\ell a\ K'_n(\kappa_\ell a)}\frac{M(1-(-1)^{M+n})}{M^2-n^2}F_{P\ell} \quad \Bigg] \tag{4.2.43}$$

After simplification, the above equations give:

$$\frac{2\pi^2 h}{\epsilon_M a}\mathcal{F}_M F_{P0} = \frac{\pi^2}{\epsilon_M}\sum_{\ell=0}^{\infty}\sum_{p=0}^{\infty}\alpha_{Mp}F_{p\ell}F_{P\ell}\left[\frac{I_M(\kappa_\ell a)}{\kappa_\ell a\ I'_M(\kappa_\ell a)} - 2\frac{K_M(\kappa_\ell a)}{\kappa_\ell a\ K'_M(\kappa_\ell a)}\right]$$
$$+\sum_{n=0}^{\infty}\sum_{\ell=0}^{\infty}\sum_{m=0}^{\infty}\sum_{p=0}^{\infty}\epsilon_n\alpha_{mp}\frac{n(1-(-1)^{n+m})}{n^2-m^2}\frac{n(1-(-1)^{n+M})}{n^2-M^2}F_{p\ell}F_{P\ell}\frac{I_n(\kappa_\ell a)}{\kappa_\ell a\ I'_n(\kappa_\ell a)}$$
$$+\pi\sum_{\ell=0}^{\infty}\sum_{m=1}^{\infty}\sum_{p=0}^{\infty}\beta_{mp}F_{p\ell}F_{P\ell}\frac{m(1-(-1)^{m+M})}{m^2-M^2}$$
$$\cdot\left[\frac{I_m(\kappa_\ell a)}{\kappa_\ell a\ I'_m(\kappa_\ell a)} + \frac{I_M(\kappa_\ell a)}{\kappa_\ell a\ I'_M(\kappa_\ell a)} - 2\frac{K_M(\kappa_\ell a)}{\kappa_\ell a\ K'_M(\kappa_\ell a)}\right] \tag{4.2.44}$$

and

$$\sum_{n=0}^{\infty}2\pi\frac{h}{a}\mathcal{F}_n\frac{M(1-(-1)^{M+n})}{M^2-n^2}F_{P0} = \sum_{\ell=0}^{\infty}\sum_{p=0}^{\infty}\beta_{Mp}\frac{\pi^2}{2}\left(1-\delta_{M0}\right)F_{p\ell}F_{P\ell}\frac{I_M(\kappa_\ell a)}{\kappa_\ell a\ I'_M(\kappa_\ell a)}$$
$$+\sum_{n=0}^{\infty}\sum_{\ell=0}^{\infty}\sum_{m=0}^{\infty}\sum_{p=0}^{\infty}\epsilon_n\beta_{mp}F_{p\ell}F_{P\ell}\frac{M(1-(-1)^{M+n})}{M^2-n^2}\frac{m(1-(-1)^{n+m})}{m^2-n^2}$$
$$\cdot\left[\frac{I_n(\kappa_\ell a)}{\kappa_\ell a\ I'_n(\kappa_\ell a)} - 2\frac{K_n(\kappa_\ell a)}{\kappa_\ell a\ K'_n(\kappa_\ell a)}\right]$$
$$+\pi\sum_{\ell=0}^{\infty}\sum_{m=0}^{\infty}\sum_{p=0}^{\infty}\alpha_{mp}F_{p\ell}F_{P\ell}\frac{M(1-(-1)^{M+m})}{M^2-m^2}$$
$$\cdot\left[\left(1-\delta_{M0}\right)\frac{I_M(\kappa_\ell a)}{\kappa_\ell a\ I'_M(\kappa_\ell a)} + \frac{I_m(\kappa_\ell a)}{\kappa_\ell a\ I'_m(\kappa_\ell a)} - 2\frac{K_m(\kappa_\ell a)}{\kappa_\ell a\ K'_m(\kappa_\ell a)}\right] \tag{4.2.45}$$

α_{mp} and β_{mp} are solution of this linear system of equations. After solving it, all $A_{n\ell}$, $B_{n\ell}$ and $C_{n\ell}$ coefficients can be deduced from the previous relations. Then the potential in the entire fluid domain is found.

The diffraction coefficient Γ is readily obtained,

$$\begin{aligned}\Gamma &= \frac{1}{A_o}\iint_{S_c}\frac{\partial\varphi_C}{\partial z}dS \\ &= \frac{-2\pi ig}{\omega}\int_0^a\sum_{\ell=0}^{\infty}B_{0\ell}\frac{I_n(\kappa_\ell r)}{\kappa_\ell a\ I_n'(\kappa_\ell a)}Z_\ell'(0)rdr \end{aligned} \tag{4.2.46}$$

which gives,

$$\widetilde{\Gamma} = \frac{-2i\pi}{a}\int_0^a\sum_{\ell=0}^{\infty}B_{0\ell}\frac{I_n(\kappa_\ell r)}{\kappa_\ell a\ I_n'(\kappa_\ell a)}Z_\ell'(0)rdr \tag{4.2.47}$$

4.3 Results on Radiation and Scattering

As in the case of the thin breakwater (3.2.2), the radiation solution can be checked by comparing the energy flux at infinity with the rate of work of the forcing pressure inside the cylinder. Let us recall that the following relation must be satisfied:

$$\overline{P\iint_{S_c}-\frac{\partial\Phi}{\partial z}\bigg|_{z=0}dS} = \overline{\iint_{S_R}-\rho\frac{\partial\Phi}{\partial t}\frac{\partial\Phi}{\partial r}dS} \tag{4.3.48}$$

where S_c is the internal free surface and S_R the surface of a circular half cylinder of any radius larger than a.

By definition, the left-hand side equals $|\widehat{p}_a|^2\,\mathcal{B}/2$. Invoking the eigenfunction expansions and taking the radius of S_R to be infinitely large, the right-hand side can be derived, yielding the relation:

$$|\widehat{p}_a|^2\frac{\mathcal{B}}{2} = \frac{|\widehat{p}_a|^2\,h}{\rho\omega}\sum_{n=0}^{\infty}\frac{|E_{n0}|^2}{\epsilon_n(ka)^2\,|H_{2n}'(ka)|^2} \tag{4.3.49}$$

or

$$\frac{\widetilde{\mathcal{B}}}{2} = \frac{h/a}{(ka)^2}\sum_{n=0}^{\infty}\frac{|E_{n0}|^2}{\epsilon_n\,|H_{2n}'(ka)|^2} \tag{4.3.50}$$

This equality is satisfied by the numerical results as shown in table (4.1) for different frequencies. For this computation as in the rest of this section the infinite series are

truncated using $N_c = 5$, $N_t = 50$ and $N_\ell = 600$ - see section 3.3.3.

kh	1.024	1.719	2.085	3.169	4.075	5.468
$\widetilde{\mathcal{B}}/2$	0.58206	3.93720	2.77660	0.41008	6.43400	0.16643
$\frac{h/a}{(ka)^2}\sum_{n=0}^{\infty}\frac{\lvert E_{n0}\rvert^2}{\epsilon_n\lvert H'_{2n}(ka)\rvert^2}$	0.58206	3.93720	2.77660	0.41008	6.43400	0.16643

Table 4.1: Comparison between the energy flux at infinity and the rate of work of the forcing pressure inside the cylinder - relation (4.3.50) - for different values of ka ; $a/h = 0.5$; $d/h = 0.2$.

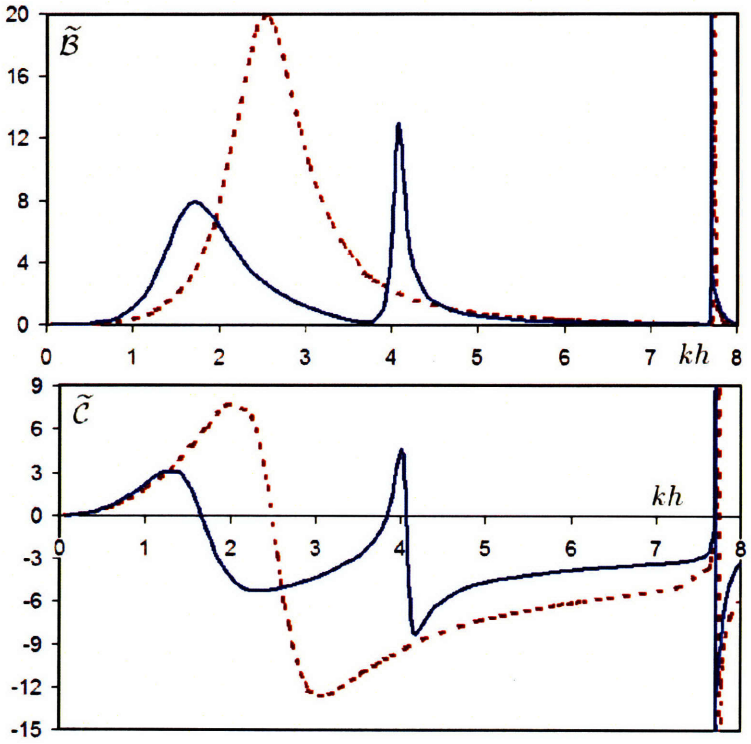

Figure 4-2: Effects of geometry on the variations with the normalized frequency kh : (i) Radiation damping $\widetilde{\mathcal{B}}$; (ii) Added mass $\widetilde{\mathcal{C}}$; $a/h = 0.5$; $d/h = 0.2$. Solid: straight coast. Dotted: Thin breakwater.

Figure (4-2) shows the obtained radiation damping coefficient and added mass for a chosen geometry ($a/h = 0.5$ and $d/h = 0.2$) compared to the breakwater case studied in chapter 3. Clearly, the present case features an additional peak in $\widetilde{\mathcal{B}}$ ($kh \approx 4.1$) between the first maximum ($kh \approx 1.7$) previously identified as Helmholtz mode ($kh \approx 2.6$ for the thin breakwater) and the first zero of J'_0 ($kh \approx 7.7$). A

corresponding singularity in $\widetilde{\mathcal{C}}$ exists at the same frequency $kh \approx 4.1$.

Let us recall that this radiation problem is not axisymmetric given the presence of the infinite wall. Thus, non-axisymmetric modes ($I_n(\kappa_\ell r)\, cos\left(n\left[\theta - \frac{\pi}{2}\right]\right), n \neq 0$) contribute. In fact, the zeroth order modes $I_0(\kappa_\ell r)$ actually can't exist alone. There must be non-axisymmetric modes, at least evanescent local contributions, for the no-flux boundary condition to be satisfied along the cylinder wall between π and 2π.

A more detailed view of the oscillation patterns at the two peaks is given when

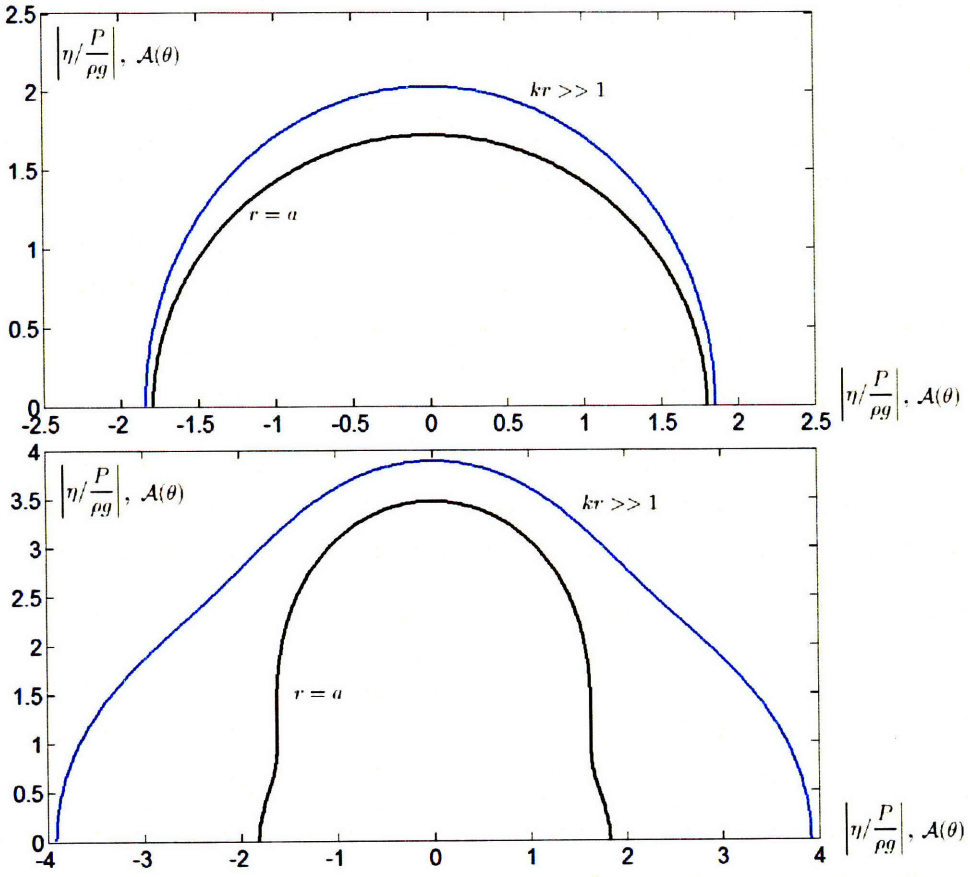

Figure 4-3: Polar plot of the free surface elevation amplitude along the outside wall of the cylinder ($r = a$) and of the coefficient $\mathcal{A}(\theta)$ for $kr >> 1$ - $h/a = 0.5$; $d/h = 0.2$. Top: $ka = 0.85923$. Bottom: $ka = 2.022$.

looking at the angular dependence of the radiated potential. Figure (4-3) presents polar plots of the outside free surface elevation amplitude along the wall and at infinity for frequencies close to each peak in the case $a/h = 0.5$, i.e. $ka = 0.859$ and

$ka = 2.022$. At infinity, the potential is written,

$$\eta(r,\theta) = \frac{P}{\rho g}\mathcal{A}(\theta)\frac{e^{ikr}}{\sqrt{kr}} \quad , \qquad kr >> 1 \tag{4.3.51}$$

where only the propagating terms $J_n(kr)$ of the series contribute. Thus $\mathcal{A}(\theta)$ is presented as the free surface amplitude angular variation far from the OWC.
Both top and bottom plots show, with roughly circular curves, that the main contribution outside the cylinder still comes from the axisymmetric mode $K_0(\kappa_\ell r)$. That is especially true for the propagating part $\mathcal{A}(\theta)$. As can be expected, the non-isotropic modes ($K_2 n(\kappa_\ell r)\, cos\,(2n\theta)$, $n \neq 0$) have a larger amplitude for larger frequencies (second peak shown by the bottom plot with less circular curves) and are mostly present as evanescent contributions along the wall.

Inside the OWC, a combination of the axisymmetric term and the first order ($I_1(\kappa_\ell r)\, cos\,(\theta - \frac{\pi}{2})$) dominates as shown by the fact that the first zero of J_1' - $J_1'(ka)$ = 0 for $ka = 1.84$ - corresponds to a close-to-zero minimum in radiation damping - $kh \approx 3.7$ in figure (4-2). This effect divides the resonance peak of the thin breakwater into two smaller peaks for the present straight coast case. This can be observed in figure (4-4) where another straight coast geometry is also presented ($a/h = 1$). Moreover, the curves are functions of ka and not kh which allows to see more clearly the effect of the zero of J_1' at the frequency $ka = 1.84$.

Note also that the amplitude of the radiation damping is significantly less than for the thin breakwater case. The frequency of the first resonance is also reduced. In the example case of $a/h = 0.5$ and $d/h = 0.2$, the first maximum is $kh \approx 2.6$ for a thin breakwater and $kh \approx 1.7$ for the straight coast case.

All these results show that the modification of the geometry brings significant qualitative changes.

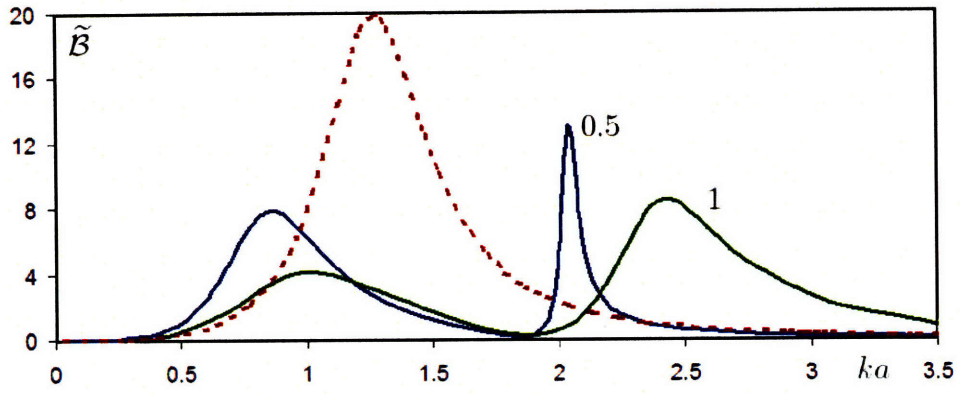

Figure 4-4: Variation of the radiation damping with the normalized frequency ka for $a/h = 0.5$; 1 and $d/h = 0.2$. Solid: straight coast. Dotted: Thin breakwater.

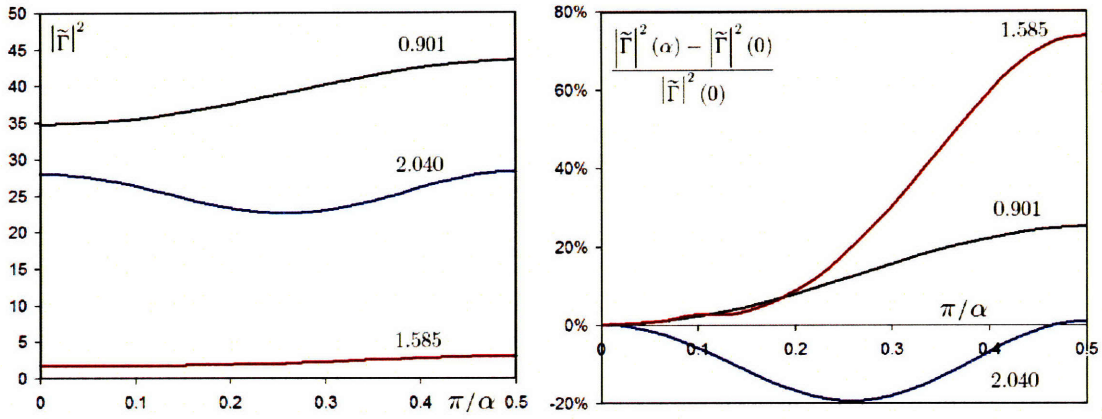

Figure 4-5: Scattering coefficient as a function of the angle of incidence α. Straight coastline, $a/h = 0.5$; $d/h = 0.2$; $ka = 0.901$, 1.585 , 2.040. (i) $\left|\widetilde{\Gamma}\right|^2(\alpha)$; (ii) ratio $\frac{|\widetilde{\Gamma}|^2(\alpha) - |\widetilde{\Gamma}|^2(0)}{|\widetilde{\Gamma}|^2(0)}$

For the scattering problem, the major difference from the previous breakwater geometry is that the scattering coefficient $\widetilde{\Gamma}$ now depends on the angle of incidence α as shown in figure (4-5) for different frequencies for the geometry $a/h = 0.5$, $d/h = 0.2$. The angles are taken from 0 to $\pi/2$ since the problem is symmetric with respect to $\theta = \pi/2$. The normalized curve on the right shows that the variation can be as large as 80% between a glancing and a normal incidence. Another feature is that the variation does not follow a single trend. For $ka = 0.901$ and $ka = 1.585$, the profile is monotonous, the scattering coefficient increasing with the angle of incidence and reaching a maximum at normal incidence. However, for $ka = 2.040$, as the angle

increases, $\left|\widetilde{\Gamma}\right|^2(\alpha)$ first decreases, reaches a minimum around $\pi/4$ and then increases to reach a maximum at $\pi/2$.

These results have been used to check the solution of the scattering problem through the relation:

$$\widetilde{\mathcal{B}} = \frac{kag}{8\pi C_g \omega} \int_0^{\pi} \left|\widetilde{\Gamma}(\alpha)\right|^2 d\alpha \tag{4.3.52}$$

where $\widetilde{\mathcal{B}}$ is known from the radiation solution. This is the equivalent of equation (3.3.26) for the straight coast line geometry with the only change being the range of integration of $\left|\widetilde{\Gamma}(\alpha)\right|^2$ limited to $[0;\pi]$ in the current case [32].

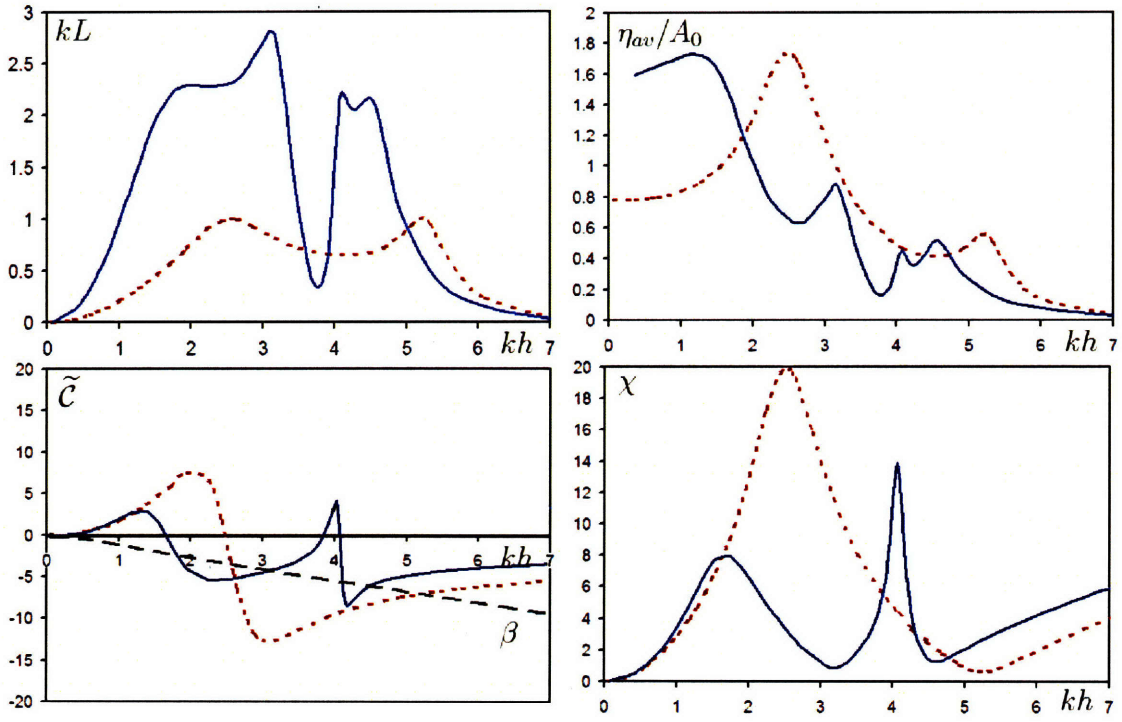

Figure 4-6: Variation with the normalized frequency kh of for: (i) Capture Length ; (ii) Average free surface elevation inside the OWC ; (iii) Added mass ; (iv) Non-dimensional turbine parameter. In all cases $a/h = 0.5$; $d/h = 0.2$; $h = 10m$. Solid: straight coast. Dotted: Thin breakwater.

4.4 Power Extraction

We shall now examine the power extraction by combining the radiation and scattering solutions with the power take-off model discussed in section 3.1. The control strategy described in section 3.4.2 is applied to obtain the following results. Keeping the same size for the OWC: $h = 10m$, $a/h = 0.5$, $d/h = 0.2$; Figure (4-6) shows the capture length, average inside free surface amplitude, added mass and turbine coefficient, all for normal incidence. The results are compared with those for the thin breakwater case. It is interesting to look first at (iii) which shows $\widetilde{C}(kh)$ and $\beta(kh)$. Recall that the single resonance peak of the thin breakwater case is replaced by two peaks in the straight coast line case. Now there are two extra intersection points between $\widetilde{C}$ and β. Consequently, kL (i) and η (ii) both exhibit 4 local maxima at these 4 intersection frequencies ($kh \approx 1.8$; $kh \approx 3.1$; $kh \approx 4.1$; $kh \approx 4.5$) instead of 2 in the thin breakwater case ($kh \approx 2.6$; $kh \approx 5.2$). While the amplitude, η_{av} is of the same order, the capture length is significantly increased. The maxima in the current case is about 2.8 which means that the efficiency at resonance is almost tripled. Moreover, the amplitude is almost always larger in the latter case with a small deficit only around the zero of J_1' and at larger frequencies. For most frequencies in the practical range - $kh < 5$ - the capture length is more than doubled.

The optimized turbine parameter χ covers a smaller range than in the thin breakwater case: this good for design purposes since it means the characteristics of the power take-off system do not need to be as versatile. However, the profile of χ is less smooth with two maxima (compared to only one previously) and quick variations. This potentially introduces more demand on the control system.

Figure (4-7) shows the capture length as a function of kh for three different angles of incidence - $\alpha = 0$, $\pi/4$, $\pi/2$. The result demonstrates that the significant gain in efficiency is not limited to a normal incidence but is also true (to a lesser degree)

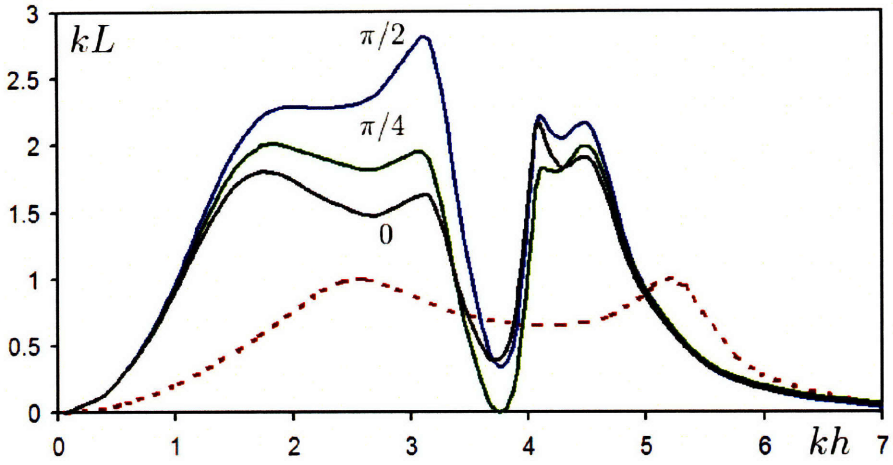

Figure 4-7: Variation of the Captured length with the normalized frequency kh ; $a/h = 0.5$; $d/h = 0.2$. Solid: straight coast. Dotted: Thin breakwater. For the straight coast, $\alpha = 0$; $\pi/4$; $\pi/2$.

for all angles. Analytically, the optimum capture length is now given by:

$$kL_{opt}(\alpha) = \frac{2\pi|\widetilde{\Gamma}(\alpha)|^2}{\int_0^\pi \left|\widetilde{\Gamma}(\alpha')\right|^2 d\alpha'} \tag{4.4.53}$$

which is obtained by combining (3.1.11), (3.4.1) and (4.3.52) when $\beta(kh) = \widetilde{C}(kh)$. This means that when β and $\widetilde{C}$ intersect, the angular average of the capture length is 2. It is consistent with figure (4-7).

Thus, this model shows that the infinite reflecting coast line acts, on average, like a concentrator of wave and doubles the efficiency of the OWC compared to an open sea configuration (equivalent to a thin breakwater).

Chapter 5

Conclusion

Different approaches have been developed to model coastline OWC devices. The hybrid element method used for the Foz do Douro OWC power plant allows one to treat complex structure geometries, specific local bathymetry and neighbouring coastline. The results we obtained for an early design show a large resonance inside the OWC chamber. The breakwater affects significantly the local wave pattern and how the free surface amplitude depends on the angle of incidence of the incoming waves.

An analytical model has been used to treat idealized geometries and predict the power extraction efficiency when considering power take off by Wells turbines. In the case of a circular cylinder at the tip of a thin breakwater, it has been shown that the power extraction is unaffected by the angle of incidence. For a circular cylinder along a straight coast, there are variations with the angle of incidence and the angular average efficiency is twice that of the previous configuration.

In both studies, the results show the effect of the different geometrical parameters such as the cylinder radius, the draft, the pneumatic chamber volume and the frequency. This allows optimizing the resonance frequency and bandwidth for a specific wave climate. Moreover, the significant effect of air compressibility has been confirmed and a control strategy based on turbine control has been presented with a clear impact on efficiency.

The present approach can be extended for different coastline configurations with little efforts. Finally, we believe that in order to obtain a more complete and precise solution, especially near resonance, the next step is to account for nonlinearities such as vortex shedding.

Appendix A

Hybrid element variational principle

This section explores in more details the hybrid element method following Yue, Chen and Mei [24, 25]. Let us show that the boundary value problem studied in chapter 2 is equivalent to the stationarity of the functional:

$$J(\phi,\phi') = \iiint_V \frac{1}{2}(\nabla\phi)^2\,dV - \iint_F \frac{\omega^2}{2g}\phi^2 dF + \iint_S \left[\left(\frac{\phi'-\phi_I}{2} - (\phi-\phi_I)\right)\frac{\partial\phi'}{\partial n} - \frac{\phi'-\phi_I}{2}\frac{\partial\phi_I}{\partial n}\right] dS \qquad \text{(A.0.1)}$$

where F is the free surface of V ($z=0$) and $\vec{n}$ is the unit normal pointing outward from the fluid.

Let's recall that the fluid domain is divided into two regions: the near field V where the spatial factor of the velocity potential ϕ is approximated by finite elements with unknown nodal coefficients and the far field V' where the potential ϕ' is represented by eigenfunction expansions. The regions are separated by the cylindrical surface S as shown in figure 2-1.

We shall first derive δJ:

$$\delta J = \iiint_V (\nabla\phi.\nabla\delta\phi)\, dV - \iint_F \frac{\omega^2}{g}\phi\,\delta\phi\, dF$$
$$+ \iint_S \left[\left(\frac{\delta\phi'}{2} - \delta\phi\right)\frac{\partial\phi'}{\partial n} + \left(\frac{\phi' - \phi_I}{2} - (\phi - \phi_I)\right)\frac{\partial\delta\phi'}{\partial n} - \frac{\delta\phi'}{2}\frac{\partial\phi_I}{\partial n}\right] dS \tag{A.0.2}$$

using the fact that $\delta\phi_I = 0$. By Green's theorem, the first term can be written as:

$$\begin{aligned}\iiint_V (\nabla\phi.\nabla\delta\phi)\, dV &= -\iiint_V \nabla^2\phi\,\nabla\delta\phi dV + \iint_B \frac{\partial\phi}{\partial n}\,\delta\phi\, dB \\ &+ \iint_F \frac{\partial\phi}{\partial z}\,\delta\phi\, dF + \iint_S \frac{\partial\phi}{\partial r}\,\delta\phi\, dS\end{aligned} \tag{A.0.3}$$

B stands for all solid walls, including the sea bed, inside V. In turn, it gives

$$\begin{aligned}\delta J = &-\iiint_V \nabla^2\phi\,\delta\phi\, dV + \iint_F \left(\frac{\partial\phi}{\partial z} - \frac{\omega^2}{g}\phi\right)\delta\phi\, dF + \iint_B \frac{\partial\phi}{\partial n}\,\delta\phi\, dB \\ &+ \iint_S \left[\left(\frac{\partial\phi}{\partial r} - \frac{\partial\phi'}{\partial r}\right)\delta\phi - (\phi - \phi')\frac{\partial\delta\phi'}{\partial r}\right] dS \\ &+ \frac{1}{2}\iint_S \left[\delta\phi'\frac{\partial}{\partial r}(\phi' - \phi_I) + (\phi' - \phi_I)\frac{\partial\delta\phi'}{\partial r}\right] dS\end{aligned} \tag{A.0.4}$$

The last integral can be rewritten,

$$\begin{aligned}&\frac{1}{2}\iint_S \left[\delta\phi'\frac{\partial}{\partial r}(\phi' - \phi_I) + (\phi' - \phi_I)\frac{\partial\delta\phi'}{\partial r}\right] dS \\ &= \frac{1}{2}\iint_S \left[\delta(\phi' - \phi_I)\frac{\partial(\phi' - \phi_I)}{\partial r} + (\phi' - \phi_I)\frac{\partial\,\delta(\phi' - \phi_I)}{\partial r}\right] dS \\ &= \frac{1}{2}\iiint_{V'} \left[(\phi' - \phi_I)\,\nabla^2\delta(\phi' - \phi_I) - \delta(\phi' - \phi_I)\,\nabla^2(\phi' - \phi_I)\right] dV' \\ &\quad -\frac{1}{2}\iint_{S_\infty \cup F' \cup B'} \left[\delta\phi'\frac{\partial}{\partial r}(\phi' - \phi_I) + (\phi' - \phi_I)\frac{\partial\delta\phi'}{\partial r}\right] dS\end{aligned} \tag{A.0.5}$$

where use is made again of Green's theorem. B' and F' are the walls and the free

surface of V'. S_∞ is a circular surface boundary extending to the sea bottom at an infinite distance.

$\phi' - \phi_I$ satisfies by construction (2.1.6) the Laplace equation (2.1.1), the outgoing condition at infinity (2.1.7) as well as the free surface (2.1.2) and walls (2.1.3) boundary conditions which means that all the terms in the previous expression are equal to zero. Thus,

$$\delta J = -\iiint_V \nabla^2\phi\,\delta\phi\,dV + \iint_F \left(\frac{\partial\phi}{\partial z} - \frac{\omega^2}{g}\phi\right)\delta\phi\,dF + \iint_B \frac{\partial\phi}{\partial n}\delta\phi\,dB + \iint_S \left[\left(\frac{\partial\phi}{\partial r} - \frac{\partial\phi'}{\partial r}\right)\delta\phi - (\phi - \phi')\frac{\partial\delta\phi'}{\partial r}\right] dS \tag{A.0.6}$$

Thus, the functional is stationary ($\delta J(\phi, \phi') = 0$) if and only if the potentials ϕ and ϕ' satisfy the Laplace equation and the boundary conditions with continuity of flux and potential at the interface S.

For the numerical implementation, ϕ is expressed as a vector of values at all the nodal points of the mesh in V and ϕ' as a vector of the unknown coefficient in the series expansion (2.1.6). The equation $\delta J(\phi, \phi') = 0$ then takes the form of a linear system of equations.

Appendix B

Appendix: Solid circular cylinder at the tip of a wedge

Among the exact techniques of solving the classical problem of two-dimensional diffraction by a semi infinite screen (or a wedge) , Stoker's method [26] can be easily extended to the diffraction of plane waves by a circular column centered at the tip of a wedge and standing on the seabed. The example of a cylinder centered at the head a thin breakwater is a limiting case. The theory to be derived applies to two dimensional sound waves, and can be modified to similar problems in elastic, electromagnetic and other media.

For simplicity the sea depth h is assumed to be constant everywhere. Let the solid part of the wedge be given by $r > a,\ \nu\pi < \theta < 0$. A solid cylinder of radius a is centered at the the tip of the wedge. An incident plane wave approaches from angle α with respect to the x axis ($\theta = 0$). Since $h =$ constant the three-dimensional velocity potential can be written as $\Phi(r, \theta, z) = \phi(r, \theta) \cosh k(z + h)$. We shall consider the horizontal factor ϕ which satisfies the Helmholtz equation in the (x, y) or (r, θ) plane. Following Stoker we expand ϕ in Fourier series

$$\phi(r, \theta) = \frac{1}{\nu\pi}\bar{\phi}_0(r) + \frac{2}{\nu\pi}\sum_{n=1}\bar{\phi}_n(r)\cos\frac{n\theta}{\nu}, \quad r > a,\ 0 < \theta < \nu\pi. \tag{B.0.1}$$

where $\bar{\phi}_n$ is the Fourier expansion coefficient (finite Fourier transform) of ϕ:

$$\bar{\phi}_n(r.\nu) = \int_0^{\nu\pi} \phi(r,\theta)\cos\frac{n\theta}{\nu}d\theta, \quad n = 0,1,2,3,... \tag{B.0.2}$$

On the wedge surfaces $\theta = 0, \nu\pi$ the normal derivative

$$\frac{1}{r}\frac{\partial\phi}{\partial\theta} = -\frac{2}{\nu\pi r}\sum_{n=1}\frac{n}{\nu}\bar{\phi}_n(r)\sin\frac{n\theta}{\nu} \tag{B.0.3}$$

vanishes for all $r > a$.

From Helmholtz equation governing $\phi(r,\theta)$, the Fourier coefficient $\bar{\phi}_n$ must satisfy

$$r^2\frac{d^2\bar{\phi}_n}{dr^2} + r\frac{d\bar{\phi}_n}{dr} + \left(k^2r^2 - \frac{n^2}{\nu^2}\right)\bar{\phi}_n = 0, \quad r > a. \tag{B.0.4}$$

To satisfy the no-flux boundary condition on the cylinder

$$\frac{d\bar{\phi}_n}{dr} = 0, \quad r = a, \quad n = 0,1,2,3,.... \tag{B.0.5}$$

the solution must be of the form,

$$\bar{\phi}_n = a_n\left(J_{n/\nu}(kr) - \frac{J'_{n/\nu}(ka)}{Y'_{n/\nu}(ka)}Y_{n/\nu}(kr)\right) \tag{B.0.6}$$

where a_n remains unknown. Since the total potential is the sum of incident ϕ^I and scattered ϕ^S potentials, the finite Fourier transform of the scattered wave is

$$\bar{\phi}^S_n = \bar{\phi}_n - \bar{\phi}^I_n = \bar{\phi}_n - \int_0^{\nu\pi}\phi^I\cos\frac{n\theta}{\nu}d\theta \tag{B.0.7}$$

Since ϕ^S must satisfy the radiation condition, we require

$$\sqrt{r}\left(\frac{d\bar{\phi}^S_n}{dr} - ik\bar{\phi}^S_n\right) \to 0, \quad kr \gg 1. \tag{B.0.8}$$

It is easily shown from (B.0.6) that

$$\sqrt{r}\left(\frac{d\bar{\phi}_n}{dr} - ik\bar{\phi}_n\right) \sim a_n\sqrt{\frac{2k}{\pi}}e^{-i(kr-\frac{n\pi}{2\nu})}\left[e^{-i\pi/4} - e^{i\pi/4}\frac{J'_{n/\nu}(ka)}{Y'_{n/\nu}(ka)}\right], \quad kr \gg 1. \text{ (B.0.9)}$$

For a plane incident wave from angle α with respect to the x axis, $\phi^I = Ae^{ikr\cos(\theta-\alpha)}$, the method of stationary phase yields:

$$\sqrt{r}\left(\frac{d}{dr} - ik\right)\bar{\phi}_n^I = \sqrt{r}\left(\frac{d}{dr} - ik\right)\int_0^{\nu\pi}\phi^I(r,\theta)\cos\frac{n\theta}{\nu}d\theta \sim 2\sqrt{2\pi k}\cos\frac{n\alpha}{\nu}e^{-i(kr+\pi/4)} \tag{B.0.10}$$

(see Stoker([26], p. 122)). To satisfy (B.0.8) we equate the two asymptotic approximations above and get

$$a_n\sqrt{\frac{2k}{\pi}}e^{-i(kr-\frac{n\pi}{2\nu})}\left[e^{-i\pi/4} - e^{i\pi/4}\frac{J'_{n/\nu}(ka)}{Y'_{n/\nu}(ka)}\right] = 2\sqrt{2\pi k}\cos\frac{n\alpha}{\nu}e^{-i(kr+\pi/4)} \tag{B.0.11}$$

yielding

$$a_n = \frac{2\pi\cos\frac{n\alpha}{\nu}e^{-\frac{in\pi}{2\nu}}Y'_{n/\nu}(ka)}{Y'_{n/\nu}(ka) - e^{i\pi/2}J'_{n/\nu}(ka)} = \frac{2\pi i\cos\frac{n\alpha}{\nu}e^{-\frac{in\pi}{2\nu}}Y'_{n/\nu}(ka)}{H'_{n/\nu}(ka)} \tag{B.0.12}$$

where $H_{n/\nu} \equiv H^{(1)}_{n/\nu}$. In particular if $n = 0$

$$a_0 = \frac{2\pi i Y'_0(ka)}{H'_0(ka)} \tag{B.0.13}$$

In summary the exact solution is

$$\phi = \sum_{n=0}\frac{\epsilon_n}{\nu\pi}\frac{2\pi i\cos\frac{n\alpha}{\nu}e^{-\frac{in\pi}{2\nu}}Y'_{n/\nu}(ka)}{H'_{n/\nu}(ka)}\left(J_{n/\nu}(kr) - \frac{J'_{n/\nu}(ka)}{Y'_{n/\nu}(ka)}Y_{n/\nu}(kr)\right)\cos\frac{n\theta}{\nu} \tag{B.0.14}$$

where $\epsilon_0 = 1; \epsilon_n = 2, n = 1, 2, 3, \ldots$ are the Jacobi symbols.

The limiting case $\nu = 2$ gives the diffraction potential for a circular cylinder at

the tip of a thin breakwater,

$$\phi = \sum_{n=0} \epsilon_n \frac{\cos\frac{n\alpha}{2} e^{-\frac{in\pi}{4}} i Y'_{n/2}(ka)}{H'_{n/2}(ka)} \left(J_{n/2}(kr) - \frac{J'_{n/2}(ka)}{Y'_{n/2}(ka)} Y_{n/2}(kr) \right) \cos\frac{n\theta}{2} \quad \text{(B.0.15)}$$

which can be rewritten as

$$\begin{aligned} \phi = & \sum_{n=0} \epsilon_n \cos\frac{n\alpha}{2} e^{-\frac{in\pi}{4}} J_{n/2}(kr) \cos\frac{n\theta}{2} \\ + & \sum_{n=0} \epsilon_n \cos\frac{n\alpha}{2} e^{-\frac{in\pi}{4}} \left[\left(\frac{iY'_{n/2}(ka)}{H'_{n/2}(ka)} - 1 \right) J_{n/2}(kr) - i \frac{J'_{n/2}(ka)}{H'_{n/2}(ka)} Y_{n/2}(kr) \right] \cos\frac{n\theta}{2} \end{aligned} \quad \text{(B.0.16)}$$

The first series is the effect of the semi-infinite screen, the second the additional effect of the cylinder. In the limit of $ka \to 0$, the second series disappears. Special cases of a half cylinder on a straight coast $\nu = 1$ and a cylinder at the tip of a right angle corner $\nu = 1/2$ can be easily obtained. These exact results can be applied to derive pressure distributions, wave forces ... etc.

Appendix C

Waves due to oscillating pressure over a circular area on the Water surface

In order to gain a better understanding of why the criteria $J'(ka) = 0$ plays a significant role in many occasions, let us examine the effect of a circular oscillating pressure corresponding to the radiation problem of an OWC with zero draft $d = 0$.

C.0.1 Hydrodynamic coefficients

In this idealized case, there is no immerged cylinder. Thus, there is no scattered wave and the incoming plain wave is simply:

$$\eta_D = a_0 \sum_{n=0} \epsilon_n i^n J_n(kr) \cos n\theta \frac{Z(z)}{Z(0)} \tag{C.0.1}$$

and thus,

$$\begin{aligned}
\widetilde{\Gamma} &= \frac{-i}{a}\int_{r<a}\frac{\partial\widetilde{\eta_D}}{\partial z}dS \\
&= \frac{-i}{a_0 a}\int_{r<a}\frac{\partial\eta_D}{\partial z}dS \\
&= \frac{-i}{a}\iint_{r<a}\sum_{n=0}\epsilon_n i^n J_n(kr)\cos n\theta\frac{Z'(z)}{Z(0)}rdrd\theta \\
&= \frac{-ik2\pi tanh(kh)}{a}\int_0^a J_0(kr)rdr \\
&= 2i\pi tanh(kh)J_0'(ka) \\
&= \frac{2i\pi\omega^2}{kg}J_0'(ka) \qquad \text{(C.0.2)}
\end{aligned}$$

Using eq. (3.3.26), this also gives:

$$\widetilde{\mathcal{B}} = \frac{\pi^2\omega^3 a}{C_g kg}J_0'^2(ka) \qquad \text{(C.0.3)}$$

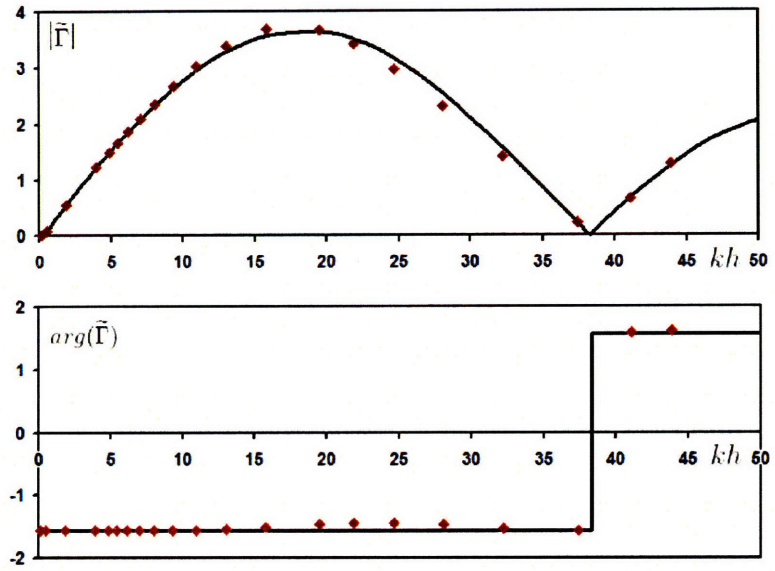

Figure C-1: Amplitude (i) and phase (ii) of the scattering hydrodynamic coefficient $\widetilde{\Gamma}$ against wave frequency for a cylinder of zero draft. Solid line: theory. Diamonds: numerical results for $d/h = 0$. In both cases $a/h = 0.1$.

Figure (C-1) shows how $\widetilde{\Gamma}$ varies with kh in a specific example - $a/h = 0.1$. The plot presents both the derived analytical expression for zero draft and the numerical

computation. Both curves match, with the same exact vanishing frequencies - zeros of $J_0'(ka)$. It can be noted though, that the agreement is not perfect for large frequencies. The error can reach the order of 10% for certain short waves ($kh > 20$). However, we attribute this effect to the finite number of terms in the series of the numerical model. Moreover, these very high frequencies are usually not in the practical range of interest for offshore structures.

C.0.2 Radiated power

Let us look now at the radiation problem considering a forcing pressure P inside the chamber. We have introduced earlier a non dimensional radiated power W - eq. (3.2.24) - that can be related to $\widetilde{\mathcal{B}}$. In fact,

$$\begin{aligned} W &= \frac{\rho\omega}{2aP^2}\overline{\iint_{S_\infty} p\frac{\partial\phi}{\partial r}dS} \\ &= \frac{\rho\omega}{2aP^2}\overline{P\int_{r=0}^{a}\int_{\theta=0}^{2\pi} -\frac{\partial\phi}{\partial z}\Big|_{z=0} dS} \\ &= \frac{\rho\omega}{2aP^2}\overline{-Pq_R} \\ &= \frac{\rho\omega}{4a}\Re\{-\bar{q}_R/P\} \\ &= \frac{\rho\omega}{4a}\Re\left\{\frac{a}{\rho\omega}\left(\widetilde{B}+i\widetilde{C}\right)\right\} \\ &= \frac{\widetilde{\mathcal{B}}}{4} \end{aligned} \tag{C.0.4}$$

Using the expression of $\widetilde{\mathcal{B}}$ (C.0.3), this gives:

$$W = \frac{\pi^2\omega^3 a}{4C_g kg}J_0'^2(ka) \tag{C.0.5}$$

This derivation is consistent with the numerical results presented in this study. Both show that for a frequency such that $J_0'(ka)$ vanishes, there is no propagating wave outside the cylinder and there is no radiated power.

This a generation of the two-dimensional result of Stoker: When $\sin ka = 0$ there is no radiation.

Appendix D

Reciprocal relation - radiation damping and scattering coefficient

For an arbitrary system of N OWC's, Evans has shown [11] that the elements of the damping matrix $\mathcal{B}$ can be expressed as:

$$\mathcal{B}_{nm} = \frac{k}{8\pi\rho g A_o^2 C_g} \int_0^{2\pi} \widehat{Q}_n^D(\alpha) \widehat{Q}_m^{D*}(\alpha) d\alpha \tag{D.0.1}$$

where $\widehat{Q}_n^D(\alpha)$ is the vertical flux in n-th OWC due to the diffraction of an incident wave of angle α.

In the case of a single OWC, the matrix $\mathcal{B}$ is of dimension 1. Moreover, for a circular OWC at the tip of a thin breakwater as studied in chapter 2, it has been shown that $\widehat{Q}^D$ is independent of α which leads to the simplification:

$$\begin{aligned} \mathcal{B} &= \frac{k}{8\pi\rho g A_o^2 C_g} \int_0^{2\pi} |\widehat{Q}^D|^2 d\alpha \\ &= \frac{k \left|\widehat{Q}^D\right|^2}{4\rho g A_o^2 C_g} \end{aligned} \tag{D.0.2}$$

This appendix provides a simplified version of Evans' derivation taking into account the particularities of this geometry including the thin breakwater.
The spatial potential radiated by a pressure of complex amplitude $\widehat{p}_a$ inside the air chamber is governed by:

$$\frac{1}{r}\frac{\partial}{\partial r}\left(r\frac{\partial\phi}{\partial r}\right)+\frac{\partial^2\phi}{\partial z^2}=0, \quad -h<z<0, \tag{D.0.3}$$

$$\frac{\partial\phi}{\partial z}-\frac{\omega^2}{g}\phi=\begin{cases}\frac{i\omega}{\rho g}\widehat{p}_a & z=0\ ;\ 0<r<a \quad (S)\\ 0 & z=0\ ;\ r>a \quad (S_F)\end{cases} \tag{D.0.4}$$

$$\frac{\partial\phi}{\partial n}=0, \quad \text{on the walls } (S_W) \text{ and the bottom } (S_B) \tag{D.0.5}$$

where $\phi\equiv\phi_C$ inside the column and $\phi=\phi_O$ outside. In addition, the wave is outgoing at infinity

$$\phi=\phi_O\sim\mathcal{A}_O\frac{e^{ikr}}{\sqrt{kr}}Z_0(z) \quad \text{when} \quad r\to\infty \tag{D.0.6}$$

with $Z_0(z)=\dfrac{\cosh\left(k(z+h)\right)}{\sqrt{\frac{1}{2}\left[1+\frac{\sinh 2kh}{2kh}\right]}}$.

The usual decomposition is used to write the vertical displacement inside the OWC:

$$\iint_{S_c}\frac{\partial\phi_C}{\partial z}dS=-\left(\mathcal{B}-i\mathcal{C}\right)\widehat{p}_a \tag{D.0.7}$$

We consider an incoming plane wave of amplitude A_0 from the direction α, φ^I. The diffraction potential is $\varphi=\varphi^I+\varphi^S$ where φ^S is outgoing at infinity. Moreover, we write:

$$\widehat{Q}^D=\iint_{S_c}\frac{\partial\varphi}{\partial z}dS \tag{D.0.8}$$

Applying Green's theorem to ϕ over the entire fluid domain within a large vertical circular cylinder S_∞ encircling the OWC, we have

$$\iiint_V \left[\phi\nabla^2\phi^* - \phi^*\nabla^2\phi\right] dV = \iint_{\partial V} \left[\phi\frac{\partial\phi^*}{\partial z} - \phi^*\frac{\partial\phi}{\partial z}\right] dS \tag{D.0.9}$$

where ∂V is the union of S, S_F, S_B, S_W and S_∞. Using the governing conditions (D.0.3), (D.0.4) and (D.0.5), only the surface integrals on S and S_∞ do not vanish. This gives:

$$\iint_S \left[\phi_C\frac{\partial\phi_C^*}{\partial z} - \phi_C^*\frac{\partial\phi_C}{\partial z}\right] dS = -\iint_{S_\infty} \left[\phi_O\frac{\partial\phi_O^*}{\partial z} - \phi_O^*\frac{\partial\phi_O}{\partial z}\right] dS \tag{D.0.10}$$

The left-hand-side can be evaluated using (D.0.4),

$$\begin{aligned}
&\iint_S \left[\phi_C\frac{\partial\phi_C^*}{\partial z} - \phi_C^*\frac{\partial\phi_C}{\partial z}\right] dS \\
&= \int_S \left[\frac{\partial\phi_C^*}{\partial z}\left(\frac{\partial\phi_C}{\partial z}\frac{g}{\omega^2} - \frac{i\widehat{p}_a}{\rho\omega}\right) - \frac{\partial\phi_C}{\partial z}\left(\frac{\partial\phi_C^*}{\partial z}\frac{g}{\omega^2} + \frac{i\widehat{p}_a}{\rho\omega}\right)\right] dS \\
&= -\frac{2i\widehat{p}_a}{\rho\omega}\ \Re\left\{\int_S \frac{\partial\phi_C}{\partial z} dS\right\} = \frac{2i\widehat{p}_a^2}{\rho\omega}\mathcal{B}
\end{aligned} \tag{D.0.11}$$

Using (D.0.6), the right-hand-side is:

$$\begin{aligned}
&-\int_{S_\infty} \left[\phi_O\frac{\partial\phi_O^*}{\partial r} - \phi_O^*\frac{\partial\phi_O}{\partial r}\right] dS \\
&= \lim_{r\to\infty} h\int_0^{2\pi} \left[\mathcal{A}_O\frac{e^{ikr}}{\sqrt{kr}}\mathcal{A}_O^*\frac{e^{-ikr}}{\sqrt{kr}}\left(ik + \frac{1}{2r}\right) + \mathcal{A}_O^*\frac{e^{-ikr}}{\sqrt{kr}}\mathcal{A}_O\frac{e^{ikr}}{\sqrt{kr}}\left(ik - \frac{1}{2r}\right)\right] r d\theta \\
&= 4i\pi h\left|\mathcal{A}_O\right|^2
\end{aligned} \tag{D.0.12}$$

Plugging (D.0.11) and (D.0.12) into (D.0.10), it yields:

$$\mathcal{B} = \frac{2\pi h\rho\omega}{\widehat{p}_a^2}\left|\mathcal{A}_R\right|^2 \tag{D.0.13}$$

Applying Green' theorem to $\varphi = \varphi^I + \varphi^S$ and ϕ and then simplifying using the boundary conditions in the same way as in (D.0.10), we obtain;

$$-\iint_S \left(\varphi \frac{\partial \phi_O}{\partial n} - \phi_O \frac{\partial \varphi}{\partial n}\right) dS = \iint_{S_\infty} \left(\varphi \frac{\partial \phi_O}{\partial n} - \phi_O \frac{\partial \varphi}{\partial n}\right) dS \tag{D.0.14}$$

Again, the left-hand-side can be evaluated using (D.0.4),

$$\begin{aligned} -\int_S \left[\varphi \frac{\partial \phi_O}{\partial z} - \phi_O \frac{\partial \varphi}{\partial z}\right] dS &= -\int_S \left[\left(\frac{i\omega \widehat{p}_a}{\rho g} + \frac{\omega^2}{g}\phi_O\right) \frac{g}{\omega^2} \frac{\partial \varphi}{\partial z} - \phi_O \frac{\partial \varphi}{\partial z}\right] dS \\ &= \frac{-i\widehat{p}_a}{\rho\omega} \int_S \frac{\partial \varphi}{\partial z} dS = \frac{-i\widehat{p}_a}{\rho\omega} \widehat{Q}^D \end{aligned} \tag{D.0.15}$$

Since φ^S and ϕ are both outgoing at infinity, $\iint_{S_\infty} \left(\varphi^S \frac{\partial \phi_O}{\partial n} - \phi_O \frac{\partial \varphi^S}{\partial n}\right) dS = 0$. Consequently, the right-hand-side of (D.0.14) is:

$$\begin{aligned} &\iint_{S_\infty} \left(\varphi \frac{\partial \phi_O}{\partial n} - \phi_O \frac{\partial \varphi}{\partial n}\right) dS = \iint_{S_\infty} \left(\varphi^I \frac{\partial \phi_O}{\partial n} - \phi_O \frac{\partial \varphi^I}{\partial n}\right) dS \\ &= \frac{-iA_0 g}{\omega Z_0(0)} \iint_{S_\infty} \left(\frac{\partial \phi_O}{\partial n} - \phi_O \frac{\partial}{\partial n}\right) e^{ik(x\cos\alpha + y\sin\alpha)} Z_0(z) dS \\ &= \lim_{r\to\infty} \frac{-iA_0 gh}{\omega Z_0(0)} \int_0^{2\pi} \left[\mathcal{A}_O \frac{e^{ikr}}{\sqrt{kr}} \left(ik - \frac{1}{2r}\right) - \mathcal{A}_O \frac{e^{ikr}}{\sqrt{kr}} ik \left(\cos\theta\cos\alpha + \sin\theta\sin\alpha\right)\right] \\ &\qquad \cdot e^{ikr(\cos\theta\cos\alpha + \sin\theta\sin\alpha)} r d\theta \\ &= \frac{A_0 gkh}{\omega Z_0(0)\sqrt{k}} \mathcal{A}_O \lim_{r\to\infty} \int_0^{2\pi} \sqrt{r} \left(1 - \cos\left(\theta - \alpha\right)\right) e^{ikr(1+\cos(\theta-\alpha))} d\theta \\ &= \frac{A_0 gkh}{\omega Z_0(0)\sqrt{k}} \mathcal{A}_O \; 2\sqrt{\frac{2\pi}{k}} e^{\frac{i\pi}{4}} \end{aligned} \tag{D.0.16}$$

where the integration is performed using the method of stationary phase.

Plugging (D.0.15) and (D.0.16) into (D.0.14) gives:

$$\mathcal{A}_O = \frac{-iZ_0(0)\widehat{p}_a e^{\frac{-i\pi}{4}}}{2\sqrt{2\pi}\rho g h A_o} \widehat{Q}^D \tag{D.0.17}$$

Thus, using this expression of $\mathcal{A}_R$ into equation (D.0.13), we get:

$$\mathcal{B} = \frac{2\pi h\rho\omega}{\widehat{p}_a^2}\frac{Z_0^2(0)\widehat{p}_a^2}{8\pi h^2\rho^2 g^2 A_o^2}\left|\widehat{Q}^D\right|^2 = \frac{\omega Z_0^2(0)}{4h\rho g^2 A_o^2}\left|\widehat{Q}^D\right|^2 \tag{D.0.18}$$

Now, let us note that: $Z_0^2(0) = \dfrac{khg}{C_g\omega}$. It yields the final result:

$$\mathcal{B} = \frac{k}{4\rho g A_o^2 C_g}\left|\widehat{Q}^D\right|^2 \tag{D.0.19}$$

Bibliography

[1] M. E. McCormick. *Ocean Wave Energy Conversion.* New York, Wiley-Interscience, 1981.

[2] D.V. Evans. Power from water waves. *Annual Review of Fluid Mechanics*, 13:157–87, 1981.

[3] C.C. Mei. *The Applied Dynamics of Ocean Surface Waves.* Advanced Series on Ocean Engineering - Vol. 1. New York, Wiley, 1983.

[4] A.F. Falcão. Control of an oscillating-water-column wave power plant for maximum energy production. *Applied Ocean Research*, 24:59–71, 2002.

[5] J. Falnes. A review of wave-energy extraction. *Marine Structures*, 20:185–201, 2007.

[6] D.V. Evans. A theory for wave power absorption by oscillating bodies. *Journal of Fluid Mechanics*, 77:1–25, 1976.

[7] C.C. Mei. Power extraction from water waves. *Journal of Ship Research*, 20:63–6, 1976.

[8] K. Budal and J. Falnes. Optimum operation of improved wave-power converter. *Marine Science Communications*, 3:133–50, 1977.

[9] D.V. Evans. The oscillating water column wave energy device. *J. Inst. Maths Applics*, 22:423–33, 1978.

[10] A.J.N.A. Sarmento and A.F. Falcão. Wave generation by a periodic surface pressure and its application in wave-energy extraction. In 15^{th} *Int. Cong. Theor. Appl. Mech.*, Toronto, Canada, 1982.

[11] D.V. Evans. Wave-power absorption by systems of oscillating surface pressure distributions. *Journal of Fluid Mechanics*, pages 481–99, 1982.

[12] C.M. Smith. *Some Problems in Linear Water Waves.* PhD thesis, University of Bristol, 1983.

[13] D.V. Evans and R. Porter. Hydrodynamics characteristics of an oscillating water column device. *Applied Ocean Research*, 17:155–64, 1995.

[14] A.J.N.A. Sarmento and A.F. Falcão. Wave generation by an oscillating surface-pressure and its application in wave-energy extraction. *Journal of Fluid Mechanics*, 150:467–85, 1985.

[15] A.C. Fernandes. *Analysis of an Axisymmetric Pneumatic Buoy by Reciprocity Relations and a Ring-source Method.* PhD thesis, MIT, Department of Ocean Engineering, 1983.

[16] D.V. Evans and R. Porter. Efficient calculation of hydrodynamic properties of owc-type devices. *Journal of Offshore Mechanics and Arctic Engineering*, 119:210–18, 1997.

[17] C.J.R. Garrett. Bottomless harbours. *Journal of Fluid Mechanics*, 43:433–49, 1970.

[18] A.F. Falcão. The shoreline owc power plant at the azores. In 4^{th} *European Wave Energy Conference*, Aalborg, Denmark, 2000.

[19] E. Martins ; F. Siveira Ramos ; L. Carrilho ; P. Justino ; L. Gato ; L. Trigo and F. Neumann. Ceodouro project: overall design of an owc in the new oporto breakwater. In 6^{th} *European Wave and Tidal Energy Conference*, Glasgow, UK, 2005.

[20] P. McIver and D.V. Evans. An approximate theory for the performance of a number of wave-energy devices set into a reflecting wall. *Applied Ocean Research*, 10:58–65, 1988.

[21] L.M.C. Gato ; P.A.P. Justino and A.F. Falcão. Optimization of power take-off equipment for an oscillating-water column wave energy plant. In 6^{th} *European Wave and Tidal Energy Conference*, Glasgow, UK, 2005.

[22] M.D.G. Neves ; F.S. Ramos ; F.M.D. Silva and L.G. Silva. Three-dimensional model tests for a wave energy power plant using the oscillation water column technology. In *Proceedings of the First International Conference on the Application of Physical Modelling to Port and Coastal Protection*, Glasgow, UK, 2006.

[23] A.J.N.A. Sarmento ; A.H. Clement ; A. Brito-Melo ; T. Hofman and G. Dehomeau. Numerical modelling of owc-shoreline devise including the effects of surrounding coastline and non-flat bottom. In *Proceedings of the 10th International Offshore and Polar Engineering Conference, vol.I, p. 743-748*, Seatle, USA, 2000.

[24] H.S. Chen and C.C. Mei. Oscillations and wave forces in an offshore harbor. Technical Report 190, CEE department, MIT, 1974.

[25] D.K.P. Yue ; H.S. Chen and C.C. Mei. A hybrid element method for calculating three-dimensional water wave scattering. Technical Report 215, CEE department, MIT, 1976.

[26] J.J. Stoker. *Water Waves.* Wiley-Interscience, 1958.

[27] C.E. Jarlan. The application of acoustical theory to the reflective properties of coastal engineering structures. Bull 1:23–63, Nat. Res. Council Canada, 1965.

[28] T. Kano ; T. Hayashi and M. Shirai. Hydraulic research on the closely spaced pile breakwater. In *Proceedings 10th Specialty Conf. on Coastal Eng.*, Santa Barbara, USA, 1966.

[29] P.L.F. Liu ; C.C. Mei and A.T. Ippen. Quadratic head loss and scattering of long waves. Report 100:217–239, ASCE J. Waterways, Harbors , Coastal Eng., 1974.

[30] R. Porter and D.V. Evans. Complementary approximations to wave scattering by vertical barriers. *Journal of Fluid Mechanics*, 294:155–80, 1995.

[31] A. Erdélyi ; W. Magnus ; F. Oberhetting and F.G. Tricomi. *Tables of Integral Transforms 1.10.* New York, McGraw-Hill, 1954.

[32] D.V. Evans. The maximum efficiency of wave-energy devices near coast lines. *Applied Ocean Research*, 10:162–4, 1988.